

# UVM ScholarWorks

## Quantifying Cartilage Composition And Arthrokinematics: Application To Short-Term Biomechanical Outcomes After Sports-Related Knee Injury And Surgery

Item Type	dissertation;article
Authors	Ramsdell, John Curtis
Download date	2026-05-13 10:41:13
Link to Item	<a href="https://hdl.handle.net/20.500.14849/3675">https://hdl.handle.net/20.500.14849/3675</a>

QUANTIFYING CARTILAGE COMPOSITION AND ARTHROKINEMATICS:  
APPLICATION TO SHORT-TERM BIOMECHANICAL OUTCOMES AFTER  
SPORTS-RELATED KNEE INJURY AND SURGERY

A Dissertation Presented

by

John Ramsdell

to

The Faculty of the Graduate College

of

The University of Vermont

In Partial Fulfillment of the Requirements  
for the Degree of Doctor of Philosophy  
Specializing in Biomedical Engineering

August, 2023

Defense Date: 05/12/2023

Dissertation Examination Committee:

Niccolo M. Fiorentino, Ph.D., Advisor

Jason H. Bates, Ph.D., Chairperson

Bruce D. Beynnon, Ph.D.

Mathew Failla, PT, Ph.D., SCS

Cynthia J. Forehand, Ph.D., Dean of the Graduate College

## ABSTRACT

The long-term consequence for many individuals who suffer ACL injury, especially when the meniscus suffers injury as well, is the development of early-onset osteoarthritis (OA), commonly referred to as post-traumatic OA (PTOA). Target therapies to reduce PTOA incidence are desperately needed, as upwards of 200,000 ACL injuries occur each year in the United States; however, therapeutic advancements are hindered by the lack of understanding for the mechanisms that drive PTOA onset and progression. A prevailing hypothesis is that post-surgical alterations to the injured knee's arthrokinematics (the way the cartilage surfaces of the femur and tibia articulate) introduce an unusual loading environment which drives cartilage degeneration and thus the onset and development of PTOA. While prior literature has revealed altered arthrokinematics and cartilage degeneration many years following surgery, the existence and timing of these alterations shortly after surgery are unknown mainly due to the limitations of traditional imaging approaches and the difficulty in comparing arthrokinematics with measures of cartilage degeneration.

The first part of this work developed and validated an imaging approach for quantifying arthrokinematic measurements using model-based tracking (MBT) with a high-speed dual fluoroscopic imaging system. MBT is a time-consuming and semiautomatic approach, and thus subject to errors during the tracking process. This work was the first to quantify the effects that intra-user variability and interpolation, which may help speed up the MBT process albeit at the cost of fidelity, have on the arthrokinematic measurement accuracy using MBT. The second part of this work involved the development and assessment of quantitative magnetic resonance imaging (qMRI) parameters,  $T1\rho$  and  $T2^*$ , as biomarkers for the knee PTOA disease progression. With this work we quantified: 1) the repeatability (side-to-side and visit-to-visit) of qMRI measurements in phantoms and healthy knees, 2) the effect of region of interest size on the repeatability of qMRI measurements, and 3) the effects of acute loading via an MR-compatible loading device on qMRI measurements. The remainder of this work utilized the approaches from the first two parts to test the aforementioned hypothesis in a patient population 1-year following ACL reconstruction and meniscus repair or resection (ACLR+M). Side-to-side differences in arthrokinematic measurements were compared to side-to-side differences in qMRI measurements.

Overall, the outcomes of this work define the capacity of our measurement systems to detect abnormalities in arthrokinematic and qMRI measurements. Furthermore, it provides us with evidence of arthrokinematic differences and signs of disease onset 1 year following ACLR+M. Ongoing work will quantify how these measurements change from 1 to 2 years. Ultimately, the results of this work will provide us with a better understanding of the mechanisms that drive PTOA, and will inform future therapeutics, such as new rehabilitation programs, aimed at slowing down or eliminating early changes in patients at high risk for PTOA.

## CITATIONS

Material from this dissertation has been published in the following form:

Ramsdell, J. C., Scott, M. E., Beynnon, B. D., Fiorentino, N. M.. (2022), “Does Interpolation and Intra-User Variability Affect the Accuracy of Arthrokinematic Measurements in the Knee? A Dual Fluoroscopic Imaging and Model-Based Tracking Study.” *Osteoarthritis Imaging*

Ramsdell, J. C., Beynnon, B. D., Borah, A. S., Gardner-Morse, M. G., Zhang, J., Krug, M. I., Tourville, T. W., Geeslin, M., Failla, M. J., Vacek, P. M., Fiorentino, N. M.. (2023), “T1 $\rho$  and T2\* Measurements in Small and Knee-Sized Magnetic Resonance Imaging Phantoms: Effect of Phantom Size and Position Relative to Isocenter” *Osteoarthritis Imaging*

Material from this dissertation has been submitted for publication in the following form:

Ramsdell, J. C., Beynnon, B. D., Borah, A. S., Gardner-Morse, M. G., Zhang, J., Krug, M. I., Tourville, T. W., Geeslin, M., Failla, M. J., DeSarno, M., Fiorentino, N. M.. (2023), “Tibial and femoral articular cartilage exhibit opposite outcomes for T1 $\rho$  and T2\* relaxation times in response to acute compressive loading in healthy knees” *Journal of Biomechanics*

## ACKNOWLEDGEMENTS

I sincerely thank all the members of my dissertation committee: to Dr. Bruce Beynnon for your guidance as a researcher and our many discussions concerning all aspects of orthopaedic research; to Dr. Mathew Failla for your insight and participation in the clinical assessment of study participants; and to Dr. Jason Bates for your advice on the proper presentation of research. I express my deepest gratitude to my advisor Dr. Niccolo Fiorentino. Your extensive knowledge of biomechanics and your dedication to producing excellent honest work has had a profound impact on me as both a young scientist and professional. It has been a pleasure working for the MIOB lab and I cannot wait to see all it accomplishes.

I thank Andy Borah, Mickey Krug, Rebecca Choquette, Mack Gardner-Morse, Melissa Cuke, Susan Platania, and Monika Donlevy for their contributions to this research and for making Stafford an enjoyable place to work.

Lastly, I would like to thank the many undergraduate and graduate students who have aided in the development of the lab and the processing and collection of data: Eduardo Valdez, James Doherty, Emily Kastens, Marit Scott, Amanda Haddad, and Orin Paxton. A special thanks to Sadegh Khodabandeloo for your major contributions and for your continuation of this work.

# TABLE OF CONTENTS

	Page
ACKNOWLEDGEMENTS .....	iii
LIST OF TABLES .....	ix
LIST OF FIGURES .....	xi
CHAPTER 1: INTRODUCTION .....	1
1.1. Post-Traumatic Osteoarthritis .....	1
1.1.1. PTOA by the Numbers.....	2
1.1.2. Proposed Mechanism Driving the Development of PTOA .....	3
1.2. Motivation for Novel Image Based Biomarkers .....	4
1.2.1. Using Model Based Tracking to Quantify Arthrokinematics .....	4
1.2.2. Using Compositional MR to Assess Cartilage Disease Progression .....	5
1.3. Dissertation Outline.....	7
CHAPTER 2: VALIDATION OF AN APPROACH FOR QUANTIFYING ARTHROKINEMATIC MEASUREMENTS USING DUAL FLUOROSCOPIC IMAGING AND MODEL-BASED TRACKING.....	8
2.1. Introduction .....	8
2.2. Methods .....	9
2.2.1. Specimen Preparation .....	9
2.2.2. CT Image Acquisition and Model Generation.....	11

2.2.3.	Dual Fluoroscopy Imaging System and Fluoroscopic Image Acquisition .	11
2.2.4.	Model-Based Tracking.....	12
2.2.5.	RSA.....	14
2.2.6.	Kinematic Metrics.....	15
2.2.7.	Arthrokinematic Metrics.....	16
2.2.8.	Statistical Analysis.....	18
2.3.	Results .....	19
2.3.1.	Activity Velocities .....	19
2.3.2.	Accuracy: Comparison of MBT Versus RSA.....	20
2.3.3.	Interpolation and Intra-User Variability .....	22
2.3.4.	Arthrokinematic Metrics.....	23
2.4.	Discussion .....	24
<b>CHAPTER 3: TEST-RETEST AND SIDE-TO-SIDE RELIABILITY OF T1P AND T2* MEASUREMENTS IN SMALL AND KNEE-SIZED PHANTOMS .....</b>		
3.1.	Introduction .....	30
3.2.	Methods.....	32
3.2.1.	Phantoms.....	32
3.2.2.	MRI Data Acquisitions .....	32
3.2.3.	Post-Processing.....	33

3.2.4. Statistical Methods.....	34
3.3. Results .....	35
3.3.1. T1 $\rho$ Acquisitions.....	35
3.3.2. T2* Acquisitions.....	36
3.4. Discussion .....	38
CHAPTER 4: THE EFFECT OF ACUTE COMPRESSIVE LOADING IN THE HEALTHY KNEE ON T1 $\rho$ AND T2* RELAXATION.....	43
4.1. Introduction .....	43
4.2. Methods.....	45
4.2.1. Study Design.....	45
4.2.2. MR Imaging.....	46
4.2.3. Post-Processing.....	48
4.2.4. Statistical Analysis.....	49
4.3. Results .....	49
4.4. Discussion .....	54
CHAPTER 5: SIDE-TO-SIDE AND VISIT-TO-VISIT REPEATABILITY OF QMRI METRICS IN HEALTHY KNEES.....	59
5.1. Introduction .....	59
5.2. Methods.....	59

5.2.1. Dataset.....	59
5.2.2. Post-Processing.....	60
5.2.3. Statistical Methods.....	60
5.3. Results .....	62
5.4. Discussion .....	64
CHAPTER 6: CHANGES IN QMRI AND ARTHROKINEMATIC MEASUREMENTS ACQUIRED SHORTLY AFTER ACL AND MENISCUS SURGERY.....	66
6.1. Introduction .....	66
6.2. Methods.....	67
6.2.1. Participants.....	67
6.2.2. Computed Tomography (CT) and Magnetic Resonance (MR) Imaging ....	68
6.2.3. Human Motion Data Collection.....	69
6.2.4. Arthrokinematic Analysis.....	70
6.2.5. QMRI Analysis.....	72
6.2.6. Statistical Methods.....	73
6.3. Results .....	74
6.4. Discussion .....	78
CHAPTER 7: DISCUSSIONS AND CONCLUSION.....	82

7.1. Implications for Future Research .....	84
REFERENCES .....	86
APPENDIX.....	95

## LIST OF TABLES

Table	Page
<p>Table 1: The average RMSE, bias, and precision of the 6DOF kinematics between the MBT (without interpolation) and the RSA for each trail across specimens and tracking instances. Flexion, abduction, and external rotation are positive rotations in degrees, and anterior, superior, and lateral translations are positive translations in mm. FlexEx: flexion-extension, IntExt: internal-external rotation, AbAd: abduction-adduction, MedLat: medial-lateral, AntPos: anterior-posterior, and InfSup: inferior-superior. ....</p>	19
<p>Table 2: Mean T1<math>\rho</math> and T2* relaxation times, variance components and measurement precision for small-vial and knee-sized phantoms (ms). Variance component analysis estimated the amount of variance attributed to vial, side (100mm to the left and 100mm to the right of isocenter), day, and slice. Total variance is the sum of all variance components. Precision of individual measurements was estimated as 1.96 times the square root of the total variance. Concentrations (Conc) listed as % agarose or mM of MnCl<sub>2</sub>.....</p>	36
<p>Table 3: The mean, standard deviation (SD) and 95% CI of the difference in T1<math>\rho</math> and T2* relaxation times between the left (L) and right (R) phantom positions for each vial (% agarose or mM of MnCl<sub>2</sub> concentration (Conc)). The L (100mm to the left of isocenter) and R (100mm to the right of isocenter) positions were chosen to replicate where the left and right knees would be located relative to isocenter during a scan of a human subject. T tests with a p-value less than 0.05 are bolded and show significant effects of position of phantom in the scanner at the time of acquisition. ....</p>	37
<p>Table 4: T1<math>\rho</math> and T2* mean responses to load (difference between unloaded and loaded conditions) of each contacting ROI in relaxation times (ms) between visits 1 and 2. Presented are lower/upper 95% confidence limits (LCL/UCL), and p-values. ....</p>	56
<p>Table 5: Participant and meniscal injury (treatment) characteristics.....</p>	68
<p>Table 6: Arthrokinematic Outcome metric differences for each subject in each compartment for the walk at 50% heel-strike to max-loading (HS-ML) and for the jog activity at 20% HS-ML. Metrics are expressed as differences between the injured and uninjured limbs (injured minus uninjured). The Anterior-Posterior (AP) and Medial-Lateral (ML) position (Pos) are the contact points in the tibial coordinate system expressed in percent of Tibial Plateau AP or ML width. A negative AP represents a posterior direction, and a negative ML represents a medial direction. Overlap metric represents the difference in number of cartilage pixels in overlap at that specific timepoint. ....</p>	73

Table 7: QMRI outcomes for the T1 $\rho$ loaded (T1 $\rho$ LD), T1 $\rho$ unloaded (T1 $\rho$ UL), and T2* Loaded (T2*LD). QMRI outcomes for each subject were measured as injured minus uninjured relaxation times (ms) for the medial (Med) and lateral (Lat) compartments of both the tibia (Tib) and femur (Fem). .....	75
Table 8a: MR scanning parameters for the T1 $\rho$ acquisitions in vivo knee scans. ....	95
Table 9a: MR scanning parameters for the unloaded and loaded T2* in vivo knee acquisitions. ....	96

## LIST OF FIGURES

Figure	Page
Figure 1: PTOA timeline, along with the proposed mechanisms that drive PTOA development.....	3
Figure 2: (a) Testing apparatus setup with a mounted cadaver pictured in front of the image intensifiers (I1 and I2); (b) DFIS includes the x-ray emitters (X1 and X2) that are projected onto their corresponding image intensifiers.....	10
Figure 3: Model-based tracking process using DSX software. The processed digitally reconstructed radiographs (cyan for femur and purple for tibia) of a tibia and femur are being matched to the underlying processed radiographs. The green and red lines represent the x-ray projection from each virtual emitter (not pictured) to its corresponding virtual image intensifier. ....	13
Figure 4: Each activity from both specimens were tracked using several different MBT approaches and using a gold standard RSA approach. Each MBT approach was repeated 3 times (instances). For the dynamic activities, the MBT approaches included tracking every 10, 5 or every frame, followed by interpolating any untracked frames with either a GCV spline or a linear interpolation type. ....	15
Figure 5: Example JSW maps during a Lunge activity on a cadaveric specimen at 45, 60, 75, and 90 degrees of flexion. The ROIs are colored according to their JSW distance. The PMDs (black markers in each compartment of both bones) were calculated using the weighted average of the points within each ROI weighted according to their distance from the other bone.....	17
Figure 6: The contact paths estimated from the RSA and the three tracking attempts (instances) of the without-interpolation solutions for both specimens and all dynamic activity types. ....	21
Figure 7: The average RMSE across specimens and tracking instances of the arthrokinematic outcome metrics for the without-interpolation tracking technique compared to the RSA for each dynamic activity type. ....	23
Figure 8: The average RMSE across specimens and tracking instances of the 6 DOF for each of the tracking techniques compared to the RSA for each dynamic activity type.....	25

Figure 9: The tracked 6DOF kinematics vs time of the Lunge activity for specimen 2 shows that the several MBT techniques closely resemble the RSA. Instances 1, 2, and 3 represent the three different pose map solutions generated from three separate tracking instances. 10 and 5 represent the interval of frames solved for, while G and L represent a GCV and Linear interpolation technique, respectively. None represents the solutions generated by solving every frame and not using interpolation. RSA represents the gold standard marker tracking. Flexion, Abduction, and External rotations are positive rotations, and Anterior, Proximal, and Lateral translations are positive translations of the tibia with respect to the fixed femur coordinate system. .... 26

Figure 10: (A) Front view of small-vials phantom for T1ρ manufactured by The Phantom Laboratory, Inc. and (B) small-vials phantom for T2\* manufactured in-house. (C,D) Knee-sized phantoms for T1ρ and T2\* filled with in-house prepared gel and solution, respectively. Labels represent concentrations in percent agarose or mM of MnCl<sub>2</sub>..... 31

Figure 11 (A,B) Example of ROI(s) in a single slice of both the small-vials and knee-sized phantoms for T1ρ. (C,D) Colormaps for the T1ρ relaxation times for each example ROI. (E,F) Colormaps for the T2\* relaxation times for each example ROI..... 34

Figure 12: Study outline for each of the 10 subjects enrolled involved two visits, with each knee being scanned in a loaded, and unloaded condition for a T1ρ and T2\* acquisition..... 45

Figure 13: The MRI loading device is driven pneumatically from the MRI control room. Researchers control the air pressure of two pistons that transmits a force directed superiorly from the foot. Participants are held in place via the combination of a climbing harness at the pelvis and the force of friction from the angled MRI tray. .... 46

Figure 14: Example tibiofemoral cartilage and subchondral bone segmentations with Non-contact and Contact ROIs shown in each compartment. .... 47

Figure 15: Relaxation times in the unloaded and applied compression loaded conditions of the 8 contact ROIs for both T1ρ and T2\*. The “\*” symbol represents a significant difference (p<0.05) in relaxation time between the unloaded and applied compression loaded condition..... 51

Figure 16: Example of sagittal T1ρ (A, B) and T2\* (C, D) images with noncontact and contact ROIs shown for both the unloaded (A, C) and loaded (B, D) conditions. Pixels with the ROIs are color mapped to their respective relaxation times (color bar on righthand side). .... 52

Figure 17 For the 4 femoral ROIs, the mean differences in relaxation times (calculated as the unloaded conditions subtracted from the applied compression load conditions) between the contact region and the noncontact regions. Data are presented for both T1 $\rho$ and T2* assessments (ms). The “*” symbol represents a significant difference (p<0.05) of effect of load between the femoral contact region and femoral noncontact regions. ....	53
Figure 18: T1rho relaxation in each ROI for both the left (light) and right (dark) legs in the unloaded (red) and loaded (blue) conditions. Significant differences are indicated by a * symbol and 95% confidence intervals are represented by error bars. ....	61
Figure 19: T2* relaxation in each ROI for both the left (light) and right (dark) legs in the unloaded (red) and loaded (blue) conditions. Significant differences are indicated by a * symbol and 95% confidence intervals are represented by the error bars. ....	62
Figure 20: T1rho relaxation in each ROI for both Visit 1 (light) and Visit 2 (dark) in the unloaded (yellow) and loaded (pink) conditions. Significant differences are indicated by a * symbol and 95% confidence intervals are represented by error bars. ....	63
Figure 21: T2* relaxation in each ROI for both Visit 1 (light) and Visit 2 (dark) in the unloaded (yellow) and loaded (pink) conditions. Significant differences are indicated by a * symbol and 95% confidence intervals are represented by the error bars. ....	64
Figure 22: Contact points at 50% HS-ML for the walk activities. The uninjured (black) and injured (red) contact locations are shown in each compartment. ....	74
Figure 23: The average difference and standard deviations in T2* relaxation between the injured and uninjured limbs of each ROI. ....	76
Figure 24: The average effect of load (loaded T1 $\rho$ - unloaded T1 $\rho$ ) between the injured (blue) and uninjured (red) limbs. ....	77
Figure 25: AP contact point absolute differences between injured and uninjured limbs vs T2* relaxation differences (injured minus uninjured). ....	79

## **CHAPTER 1: INTRODUCTION**

### **1.1. Post-Traumatic Osteoarthritis**

One of the more severe and common injuries of the young athletic population is the anterior cruciate ligament (ACL) tear. Thanks to advancements in surgical procedures and rehabilitation, young athletes undergo ligament reconstruction that restores stability to the joint and leaves athletes with the relatively short-term consequence of missing a single season [1,2]. However, epidemiologic studies show us that the consequences of suffering sports related knee injuries are not limited to the short-term.

In 2004, Lohmander et al. found that 82% of women soccer players who sustained an ACL injury twelve years prior had radiographic changes associated with post traumatic osteoarthritis (PTOA) to their injured knee, and 75% of these women reported having knee-related symptoms affected their quality of life [3]. The mean age of these women was 32 years old at the time of assessment. Six years later, a study by Oiestad et al. reported similar results suggesting the percentage of individuals that develop OA 10 – 15 years following injury is as high as 62% for isolated ACL injuries and an astonishing 80% for combined ACL injuries (i.e., injuries to the ACL and meniscus) [4]. Neither of these two studies were able to show that ACL reconstructions improved outcomes 10-15 years after the index surgery.

Ultimately, the long-term effects for most individuals who suffer ACL injuries, especially those including the meniscus, are clear: That their injured knee is predisposed to accelerated alterations to the articulating cartilage and the development of early-onset of (PTOA) [5–10]. Target therapies to reduce PTOA incidence are desperately needed [11].

However, advancements are hindered by the lack of understanding of the mechanisms that drive PTOA progression. For young patients, this means increased symptoms associated with PTOA that can require multiple joint replacements to treat, years of pain, and decreased mobility and strength all of which decrease a patient's quality of life [12–15].

### **1.1.1. PTOA by the Numbers**

Osteoarthritis (OA) is the leading cause of mobility impairment in older adults in the United States [16]. From 1995 to 2005 the number of adults with OA increased by 6 million, and is expected to reach a total of 67 million by 2030 [17]. In 2003, the annual costs of OA was reported at \$89.1 billion in the US alone [17]. While most OA cases result mainly from natural aging, close to 12% of cases are a result of previous lower extremity trauma [18]. These patients suffer from post-traumatic osteoarthritis, or PTOA. Of particular concern, persons who sustain a knee injury are 4.2 times more likely to develop OA than those who haven't experienced prior knee injury [6]. Consequently, the financial burden attributed to PTOA on the US health care system is ~\$3 billion annually [19]. From 1994 to 2006, the number of ACL reconstructions (ACLR) in the US has increased from ~86,000 to ~129,000 with about a third of them involving injuries to the meniscus [20]. The reported prevalence of PTOA for patients who undergo ACLR with concomitant meniscal resection ranges between 21%-48% [4,13,21]. With the number of sports-related injuries continuing to rise and the inability to hinder the onset of PTOA, the burden on the health care system will continue to grow substantially.

### 1.1.2. Proposed Mechanism Driving the Development of PTOA

The development of interventions to treat PTOA required an understanding of the mechanisms that drive PTOA development. A prevailing hypothesis is that following injury and surgery there are alterations to the arthrokinematics (the way the cartilage surfaces of the femur and tibia interact with each other) during daily activities such as walking (**Figure 1**). Subsequently, these alterations introduce an abnormal loading environment to the cartilage due to either increases in stress through contact area reduction, or abnormal loading patterns. Ultimately, abnormal loading patterns and increased stress lead to catabolism of cartilage matrix components and eventually result in the thinning and degradation of articular cartilage over time.

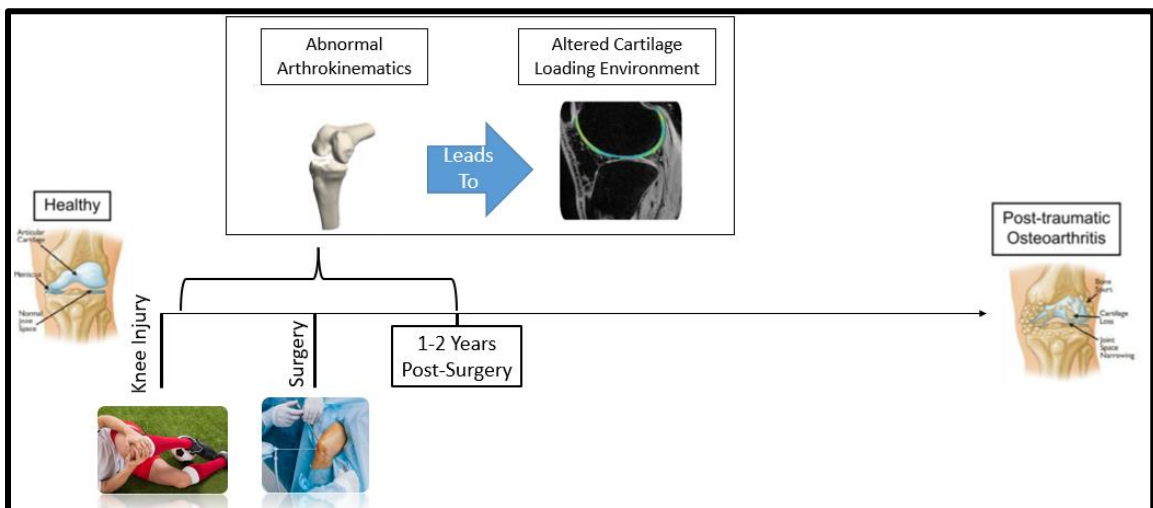


**Figure 1: PTOA timeline, along with the proposed mechanisms that drive PTOA development.**

To test this hypothesis, requires the ability to measure changes to both the loading environments within the knee and the health of the cartilage. While prior literature has provided evidence that knee injury and surgery has led to altered kinematics and cartilage

morphology long term [3,4,22], the existence and timing of these alterations shortly after surgery are unknown mainly due to the limitations of traditional imaging approaches and the difficulty in comparing arthrokinematics with measures of cartilage degeneration. However, novel imaging techniques with better resolutions and accuracy can now detect smaller/earlier changes that are known to occur in the short-term following injury.

## **1.2. Motivation for Novel Image Based Biomarkers**

### **1.2.1. Using Model Based Tracking to Quantify Arthrokinematics**

To accurately quantify abnormal cartilage loading environments that occur early during disease progression requires an approach that: 1) is highly accurate, 2) can quantify interactions inside the joint, and 3) captures dynamic movements that are common during daily activities such as walking. Optical tracking using skin markers has been one of the more common and traditional methods for quantifying joint angles and translations, known as kinematics. This approach involves using the position of markers taped to the skin to estimate the position and orientation of the underlying bones by assuming the markers on the skin move rigidly with the bones. However, there are concerns with this measurement technique because the soft tissue tissues between the skin surface mounted markers and bones are not rigid. Consequently, kinematic errors known as soft tissue artifact are produced [23–25]. Specifically, when measuring tibiofemoral joint kinematics, errors associated with soft tissue artifact have been shown to be as large as  $10^\circ$  in rotation and 10 mm in translation during dynamic activities [26]. These errors are much too high to quantify altered cartilage loading environments as the average thickness of human articular cartilage in the knee is closer to 3 mm [27]. There are other methods of quantifying human

movement such as wearable devices and artificially intelligent (AI) driven optical tracking [28–31]. A major drawback of these approaches as well as optical marker tracking is the lack of information regarding the bony anatomy of a specific subject. In other words, to accurately calculate surface interactions within the joint it would be necessary to have subject-specific bone or cartilage models. There are clinical imaging modalities, for example magnetic resonance (MR) imaging and computed tomography (CT), that can produce subject specific bone models, but they have sampling rates that are too slow to capture dynamic movements such as gait. Ultimately, the most practical approach to quantifying abnormal cartilage loading environments is to compute arthrokinematic metrics using a marker-less tracking techniques known as model-based tracking (MBT), along with a high-speed dual fluoroscopic imaging system (DFIS). This approach utilizes subject specific tissue models that are developed from CT or MRI acquisitions and has rotational and translational errors on the order of one degree and one millimeter, respectively [32–36]. Subject specific tissue models and high accuracy tracking permits the modeling of cartilage-on-cartilage surface interactions within the joint during routine daily activities. However, due to the novelty and technical rigor involved with this approach, systematic validations must be conducted to ensure measurement systems produce accurate measurements.

### **1.2.2. Using Compositional MR to Assess Cartilage Disease Progression**

Measurements that assess the composition of cartilage are necessary to test the aforementioned hypothesis that abnormal loading leads to the disease progression in cartilage. A popular approach involves analyzing the morphology, namely the thickness of

the cartilage. This is logical, as one of characteristics associated with progression of osteoarthritis is the thinning or breaking down of the articular cartilage within a joint. Much research has been done developing morphological cartilage measurements. Briefly, morphological measurements have evolved from inferring cartilage thickness with joint space width (JSW) measurements via radiographic projections to more recently measuring 3D cartilage thickness maps via high resolution MR images [3,37,38]. In addition to morphological assessments, MR imaging permits compositional assessments via relaxometry. The advantage of compositional measurements over morphological measurements is that compositional changes to the articular cartilage occur prior to irreversible morphological changes [39]. Thus, compositional measurements via MR imaging are better suited for detecting the initial onset and early progression of OA in cartilage than traditional morphological measurements. However, studies have reported large variations in their ability to repeat compositional MR measurements. For example, a review reported test-retest intraclass correlations (ICCs) ranging from 0.2 – 0.96 in compositional MR measurements of human knee cartilage [40]. To study the effects of surgery or abnormal loading on the composition of cartilage it is necessary to make side-to-side and timepoint-to-timepoint comparisons. Therefore, the side-to-side and timepoint-to-timepoint variation in healthy uninjured control knees must be quantified to detect if changes in composition are abnormal.

Additionally, since abnormal loading of the cartilage is hypothesized to initiate the progression to OA, abnormal responses to load on cartilage could be a good predictor for the initiation of progression to OA. In other words, diseased cartilage may respond

differently to load than healthy cartilage. The challenge of studying articular cartilage in a loaded state is the need for an MR-compatible loading device, which is difficult to construct due to material and size constraints, and the requirement that the subject's knee remains motionless during scan acquisition. As result of this difficulty, little is known about how cartilage (healthy or diseased) responds to load.

### **1.3. Dissertation Outline**

The overall aim of this work is to test the hypothesis that altered arthrokinematics following knee injury that involves the ACL and surgery to reconstruct it causes accelerated progression of OA. As motivated above, to test this hypothesis requires the proper development, validation, and assessment of systems capable of measuring short-term biomechanical outcomes. Thus, the initial part of this work was the development of these systems. Chapter 2 describes an assessment of a model-based tracking system's ability to quantify arthrokinematic outcome metrics. Chapter 3 describes the repeatability and validation of compositional MR measurements in phantoms, which are standards used in MR imaging. Chapter 4 describes how compositional MR measurements of cartilage respond to acute compressive loading in healthy knees. Chapter 5 describes the repeatability of compositional MR measurements in healthy controls. Chapter 6 describes side-to-side differences in arthrokinematic measurements and side-to-side differences in qMRI measurements in a patient population 1-year following ACL reconstruction and meniscus repair or resection (ACLR+M). Chapter 7 concludes this dissertation with discussions, conclusions, and implications for future work.

## **CHAPTER 2: VALIDATION OF AN APPROACH FOR QUANTIFYING ARTHROKINEMATIC MEASUREMENTS USING DUAL FLUOROSCOPIC IMAGING AND MODEL-BASED TRACKING**

*A modified version of this chapter has been submitted for publication as: Ramsdell, JC., Scott., ME, Beynon, BD., Fiorentino, NM., (2022), "Does Interpolation and Intra-User Variability Affect the Accuracy of Arthrokinematic Measurements in the Knee? A Dual Fluoroscopic Imaging and Model-Based Tracking Study." Osteoarthritis Imaging*

### **2.1. Introduction**

A prevailing hypothesis postulates that abnormal joint arthrokinematics, namely the way joint surfaces interact with each other, following joint trauma play a key role in the cascade of events that lead to post-traumatic osteoarthritis (PTOA) [5,41–43]. Thus, the ability to accurately quantify altered arthrokinematics is pivotal in providing supporting evidence that the proposed pathological framework drives PTOA.

A dual fluoroscopic imaging system (DFIS) with model-based tracking (MBT) has become an increasingly popular measurement technique to quantify knee arthrokinematics [44]. This is a highly accurate, dynamic, and subject-specific approach that in multiple settings has been shown to estimate 6 degree of freedom (DOF) joint kinematics with errors on the order of 1 mm and 1 degree or less [34–36,45,46]. Still, MBT has the significant disadvantage of being a time-consuming and semi-automatic process. As a result, the user input involved in model-based tracking is subject to errors.

One strategy to reduce analysis time is to track fewer frames and interpolate between tracked frames. However, the effect of interpolation on the measurement system's accuracy is relatively unknown. Furthermore, while prior studies have mainly reported the accuracy

of MBT in terms of their ability to quantify 6DOF kinematics, it remains unclear how intra-user variability or interpolation propagate to arthrokinematic outcome metrics. More specifically, it is unclear how errors during the tracking progress propagate to the contact paths, which is the path of the contact points defined by the proximity of the two adjacent subchondral bone surfaces, such as in the medial compartment of the tibiofemoral joint.

Therefore, the present study had two purposes: 1) to establish the accuracy of our DFIS with MBT in measuring tibiofemoral joint kinematic and arthrokinematic outcome metrics in comparison to a gold standard radiostereometric analysis (RSA) marker tracking approach, and 2) to determine how several different interpolation techniques and intra-user variability affect kinematic and arthrokinematic outcome metrics.

## **2.2. Methods**

### **2.2.1. Specimen Preparation**

Two cadaveric mid-thigh to mid-shank specimens were used for the present study (Specimen 1: 67 years old, black male, 183 cm, 97.5 kg, BMI 29; Specimen 2: 70 years old, white male, 178 cm, 101kg, BMI 32). Four 3.175 mm diameter stainless steel spheres were embedded into the proximal tibia and distal femur of the two cadaveric specimens. The spheres were placed to maximize inter-marker distances while avoiding co-linearity and to exploit the accuracy of radio stereometric analysis (RSA) [47]. Both the transected femur and tibia were inserted and fixed in nylon tubing so the specimens could be positioned and manually manipulated inside the field of view (FOV) of the DFIS while minimizing the researcher's exposure to radiation (Figure 2a). The tibia tubing was secured

into a custom testing apparatus that acted as a hinge joint allowing the specimen to be swung with the purpose of replicating an inverse double pendulum. The femoral tubing was free to be actuated by the researcher to simulate knee joint movement. To simulate movement of the patella, a suture was attached on one end to the quadriceps tendon and secured to the femoral tubing while the knee was in full extension using an approach that has been described [48].

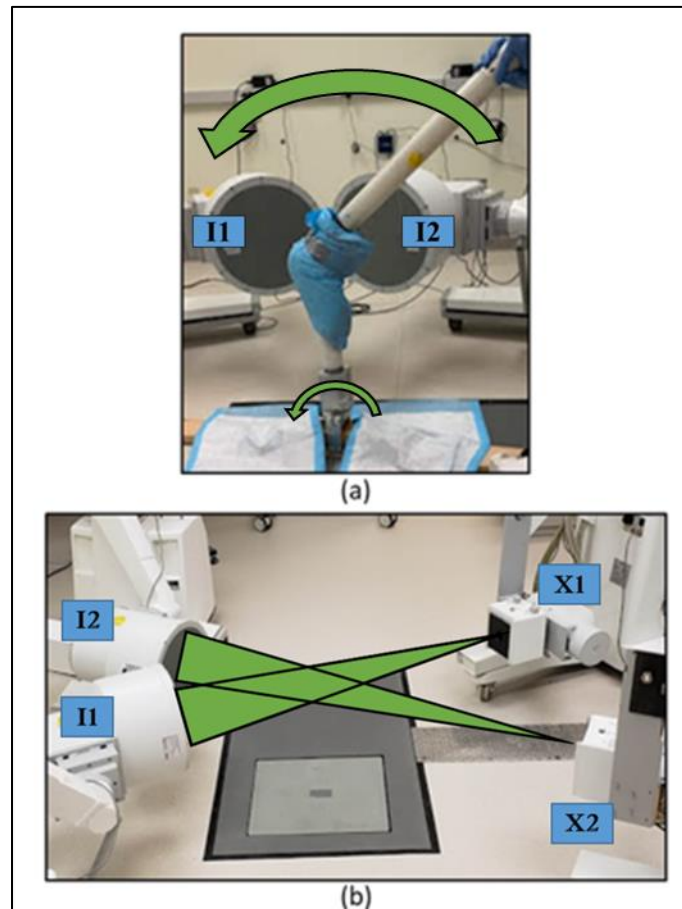


**Figure 2: (a) Testing apparatus setup with a mounted cadaver pictured in front of the image intensifiers (I1 and I2); (b) DFIS includes the x-ray emitters (X1 and X2) that are projected onto their corresponding image intensifiers.**

### **2.2.2. CT Image Acquisition and Model Generation**

Computed tomography (CT) images were collected using an iCT SP imaging system (Philips, Eindhoven, Netherlands). The CT acquisition settings were set to .67 mm slice thickness, 120 KVp, and an in-plane resolution of .195 mm/pixel with metal artifact reduction. The radiation technician was instructed to capture a 300 mm FOV centered along the tibiofemoral joint line. Following acquisition, the femur and tibia were manually segmented (Seg3D v2.4.4, University of Utah) from the CT images. Marker-less reconstructed bone models were created by replacing the pixels that represented markers with random intensities within a range of values similar to that of the surrounding bone [34]. Surface models were imported into MeshLab (v2012.12, Visual Computing Lab) and were smoothed and re-meshed to have 1 mm edge lengths [49]. The bone models were imported into Dynamic Stereo X-ray (DSX) software (C-Motion Inc., Germantown MD) to define local anatomic bone-based coordinate systems [50].

### **2.2.3. Dual Fluoroscopy Imaging System and Fluoroscopic Image Acquisition**

After 24 hours of exposure to room temperature, the cadaveric specimens were secured into the testing apparatus (**Figure 2a**). For each specimen, a static standing activity was captured with the knee in a fully extended position, followed by three dynamic activities. The first two dynamic activities represent the system's ability to track knees at similar velocities to the first 10% of the stance phase of walking and jogging gait cycles, as DFIS are most accurate prior to the contralateral knee entering the FOV. The third activity represents the system's ability to track at high flexion angles similar to a lunging activity. With support from a metronome, the specimens were manually manipulated during the

dynamic activities with instruction to: swing the specimen in full extension at a walking pace (Walk); swing the specimen and slightly flex the knee at a faster than walking pace (Jog); and flex the knee to 90 degrees (Lunge) through the FOV of the DFIS.

All activities were collected at 125 images per second with a resolution of 1024x1024 using synchronized high-speed digital cameras (FASTCAM Mini AX50, Photron, Tokyo, Japan). Static and dynamic activities were shuttered at 1/600 and 1/1000s, respectively. Dual X-rays were generated continuously during the activity (105-125 kVp and 5mA) using a custom-built DFIS (Radiological Imaging Services, Hamburg, PA, USA) (**Figure 2b**). The source to image distance was set to 120 cm. The imaging volume was calibrated after specimen testing. Calibration involved collecting blank images, images of a grid with holes of known dimension, and images of a calibration object described by Brainerd et al. [51]. The calibration object defined the laboratory coordinate system and was used to digitally set the coordinate system of the DFIS.

#### **2.2.4. Model-Based Tracking**

The radiographs were processed by downsampling to 512x512, white balancing, filtering spatially, distortion correcting, and convoluting with a Sobel filter to emphasize edges [52,53]. The MBT was performed in the X4D application of DSX using the marker-less reconstructed bone models with an approach that has been described [36]. The CT-based models were placed within the digitally reconstructed orientation and position of the DFIS to generate digitally reconstructed radiographs (DRR) that were semi-automatically aligned with processed radiographs (**Figure 3**). Manual user input generated initial guesses, followed by an optimization process for the quantitative solution. Ultimately, the judgment

of the user determined the final position and orientation (pose) of the bone models that best fit the DRR with the processed radiographs.

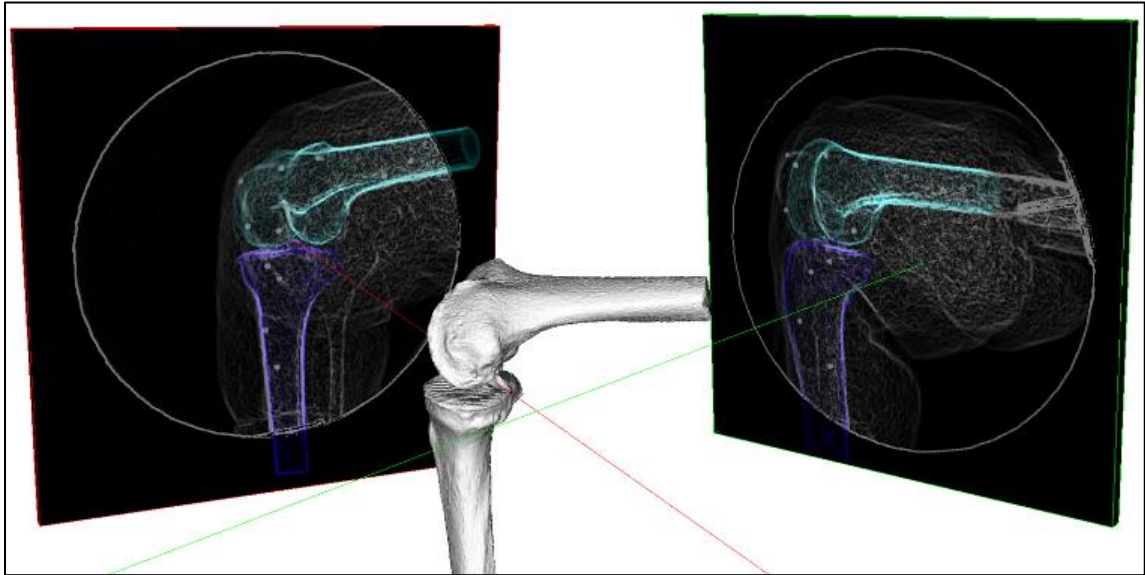


**Figure 3: Model-based tracking process using DSX software. The processed digitally reconstructed radiographs (cyan for femur and purple for tibia) of a tibia and femur are being matched to the underlying processed radiographs. The green and red lines represent the x-ray projection from each virtual emitter (not pictured) to its corresponding virtual image intensifier.**

For each of the activities from both specimens, the bone poses were generated by solving frames in intervals of 10 frames, 5 frames, and finally by solving each frame (without-interpolation). At 125Hz, this is equivalent to generating a solution every 0.08s, 0.04s, and 0.008s(without-interpolation). Any solutions with untracked frames were interpolated using both a 5th order generalized cross validation (GCV) spline method with a 20 Hz cut-off frequency and a linear spline method [54]. This process was repeated in three separate instances (tracking instance) by the same user (JR) to test intra-user variability, generating a total of 48 unique solutions including the Static solutions for each of the two specimens (96 total) (**Figure 4**).

### **2.2.5. RSA**

The two-dimensional locations of the implanted markers in the processed radiographs were tracked semi-automatically in the Locate3D application of DSX. The three-dimensional bone poses for each time frame in reference to the laboratory-based coordinate system were calculated using the CT-defined positions of the markers and the digitally calibrated orientation of the DFIS.

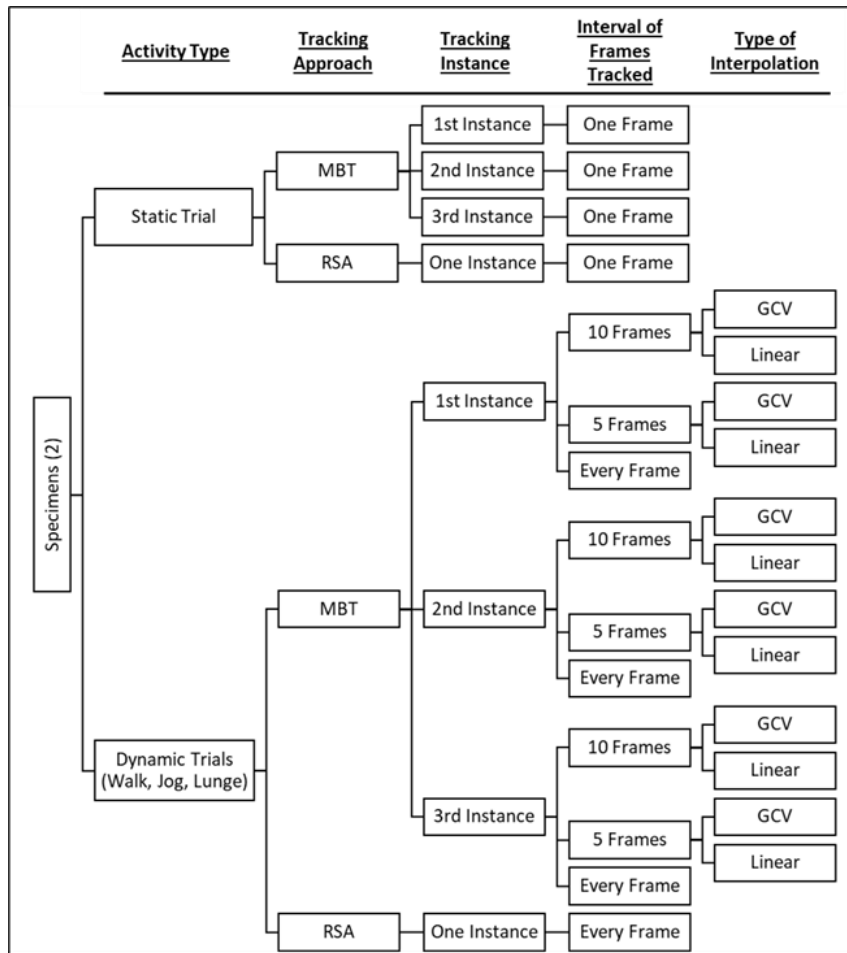


**Figure 4: Each activity from both specimens were tracked using several different MBT approaches and using a gold standard RSA approach. Each MBT approach was repeated 3 times (instances). For the dynamic activities, the MBT approaches included tracking every 10, 5 or every frame, followed by interpolating any untracked frames with either a GCV spline or a linear interpolation type.**

### 2.2.6. Kinematic Metrics

Bone poses were imported into MATLAB (The Mathworks Inc., Natick, MA) where the 6DOF joint kinematics at each frame were calculated following the Grood and Suntay method and were filtered with a fourth-order Butterworth low-pass filter and a cutoff frequency of 6 Hz [55]. To describe the speed of the activities, the specimen velocities (velocity of the specimen through space) for each activity were quantified from the RSA

solutions. The velocities were calculated by differentiating the 3D Euclidean distance between frames of the femoral anatomical system origin with respect to time.

### 2.2.7. Arthrokinematic Metrics

Bone surface models were imported into MATLAB as STL files. There, the centroid of each triangular face on the surface models was converted into a point cloud. Each point in the tibia's anatomical coordinate system  $(Tx_n, Ty_n, Tz_n)$  was then referenced to the anatomical coordinate system of the femur to become  $(Tx'_n, Ty'_n, Tz'_n)$  at each frame as shown:

$$\begin{bmatrix} Tx'_n(t) \\ Ty'_n(t) \\ Tz'_n(t) \\ 1 \end{bmatrix} = LTT(t)^{-1} * LTF(t) \begin{bmatrix} Tx_n \\ Ty_n \\ Tz_n \\ 1 \end{bmatrix}$$

where n represents the number of centroids in the point cloud, t represents the time frame, and LTF(t) and LTT(t) represent the lab-to-femur and lab-to-tibia transformation matrices at specific time frames t derived from the bone poses generated in DSX.

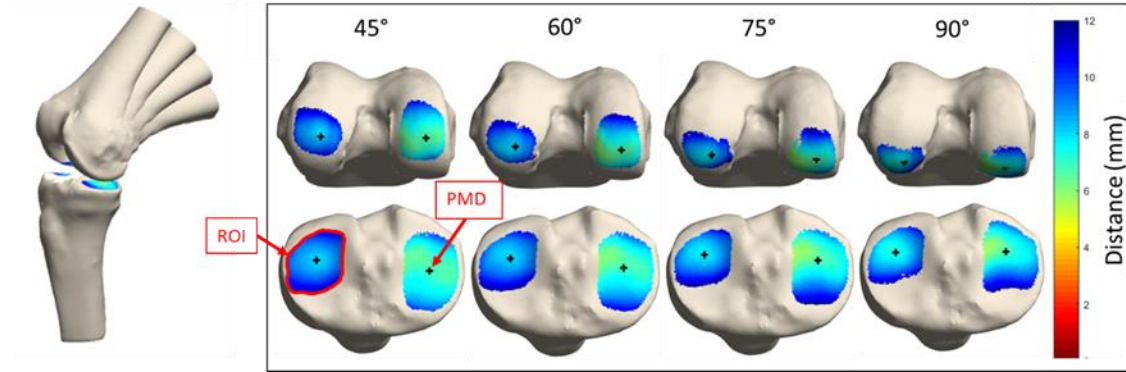


**Figure 5: Example JSW maps during a Lunge activity on a cadaveric specimen at 45, 60, 75, and 90 degrees of flexion. The ROIs are colored according to their JSW distance. The PMDs (black markers in each compartment of both bones) were calculated using the weighted average of the points within each ROI weighted according to their distance from the other bone.**

For each time frame, the dynamic joint space width (JSW) maps and the point of minimum distance (PMD) for each compartment were estimated using a method similar to ones previously described (Figure 5) [56,57]. First, using an algorithm similar to Foumani et al., a region of interest (ROI) was defined as the points on both subchondral bone surfaces estimated to be in contact. A surface was considered within the ROI if its JSW was less than 12mm, and the angle between the vector representing the surface normal and the vector to the closest point on the other bone was less than 30 degrees [58]. In addition, to exclude the intercondylar region, a plane was fit to the tibia plateau and all points that were located within 3mm superior or inferior of this plane were defined as eligible for the ROI. The PMD for a particular compartment was then determined using a weighted centroid algorithm where the positions of the points in the ROI of that compartment were weighted based on their JSW [20]. When calculating the PMDs of the femur, the centroid points were converted to cylindrical coordinates to account for the curved surfaces and then converted back to cartesian coordinates. The collection of the PMDs over all analyzed

timeframes for a particular activity was considered the contact path. The arthrokinematic outcome metrics were generated for each contact path and were path location, anterior-posterior (AP) excursion, and medial-lateral (ML) excursion. The path locations were made up of the locations of each PMD in the anatomical coordinate systems. The AP and ML excursion was quantified as the displacement along their respective directions for the full length of the activity [59].

### **2.2.8. Statistical Analysis**

Each of the MBT 6DOF kinematic solutions was compared to its respective RSA solution in terms of bias (average difference throughout an activity), precision (standard deviation of the differences throughout an activity), and root mean squared errors (RMSE). The arthrokinematic outcome metrics were also compared against the RSA solutions in terms of AP excursion differences, ML excursion differences, path location error, and path location precision. The path location error was calculated by averaging the Euclidean distances between an MBT solution and the RSA solution at each time frame. The path location precision was defined as the standard deviation of these differences.

The overall accuracy of our DFIS with MBT was determined by averaging the 6DOF kinematic errors and the arthrokinematic outcome metric errors from the without-interpolation (tracking every frame) solutions across each tracking instance and of the two specimens (six solutions) for every activity type. Finally, mixed model repeated measures analyses of variance were used to test for significant differences in means by tracking instance, interval of frames interpolated (10, 5, and none), and type of interpolation (GCV and linear) used. For each statistically significant main effect, post-hoc pairwise

comparison tests were conducted, where appropriate, to test for significant differences in means between each pair of levels. Statistical significance level alpha was set a priori at 0.05. Statistical analyses were conducted using SAS statistical analysis software, version 9.4 (SAS Institute, Inc., Cary, NC, USA).

## 2.3. Results

### 2.3.1. Activity Velocities

The absolute maximum knee velocity for specimens 1 and 2 were: 674 and 546 mm/s, 815 and 683 mm/s, and 137 and 81 mm/s for the simulated Walk, Jog, and Lunge activities, respectively.

**Table 1: The average RMSE, bias, and precision of the 6DOF kinematics between the MBT (without interpolation) and the RSA for each trail across specimens and tracking instances. Flexion, abduction, and external rotation are positive rotations in degrees, and anterior, superior, and lateral translations are positive translations in mm. FlexEx: flexion-extension, IntExt: internal-external rotation, AbAd: abduction-adduction, MedLat: medial-lateral, AntPos: anterior-posterior, and InfSup: inferior-superior.**

		<i>FlexEx</i>	<i>IntExt</i>	<i>AbAd</i>	<i>MedLat</i>	<i>AntPos</i>	<i>InfSup</i>
<i>RMSE</i>	Static	0.5±0.1	0.6±0.3	0.4±0.3	0.3±0.2	0.6±0.3	0.4±0.3
	Walk	0.5±0.2	0.7±0.1	0.5±0.2	0.3±0.2	0.6±0.4	0.2±0.1
	Jog	0.6±0.5	0.9±0.6	0.6±0.2	0.6±0.3	0.7±0.6	0.3±0.1
	Lunge	0.3±0.1	0.6±0.1	0.8±0.3	0.6±0.1	0.7±0.1	0.7±0.4
<i>Bias</i>	Static	0.5±0.1	0.3±0.6	0.4±0.3	-0.2±0.3	0.6±0.3	0.4±0.3
	Walk	-0.1±0.4	0.4±0.4	0.2±0.4	0.2±0.3	0.5±0.5	0.0±0.2
	Jog	-0.4±0.6	-0.2±0.4	0.1±0.3	0.3±0.6	0.5±0.7	0.1±0.2
	Lunge	-0.1±0.1	0.1±0.4	-0.1±0.7	0.2±0.2	0.7±0.2	-0.4±0.7
<i>Precision</i>	Walk	0.4±0.1	0.7±0.1	0.3±0.1	0.3±0.1	0.3±0.1	0.2±0.0
	Jog	0.3±0.2	1.0±0.7	0.6±0.3	0.3±0.2	0.5±0.2	0.2±0.1
	Lunge	0.3±0.1	0.6±0.1	0.6±0.2	0.6±0.1	0.3±0.0	0.3±0.1

### **2.3.2. Accuracy: Comparison of MBT Versus RSA**

The RMSEs between the MBT and RSA measurement approaches from all activities in each DOF were less than 1mm in translation and 1° in rotation (**Table 1**). The bones from the Jog activities experienced the largest velocities and showed the highest 6DOF kinematic RMSEs that ranged from  $0.3\pm 0.1$  mm in AP translation to  $0.9\pm 0.6^\circ$  in internal-external (IE) rotation. In three of the four activities, the largest RMSEs occurred in IE rotation (range  $0.6\pm 0.3^\circ$  to  $0.9\pm 0.6^\circ$ ).

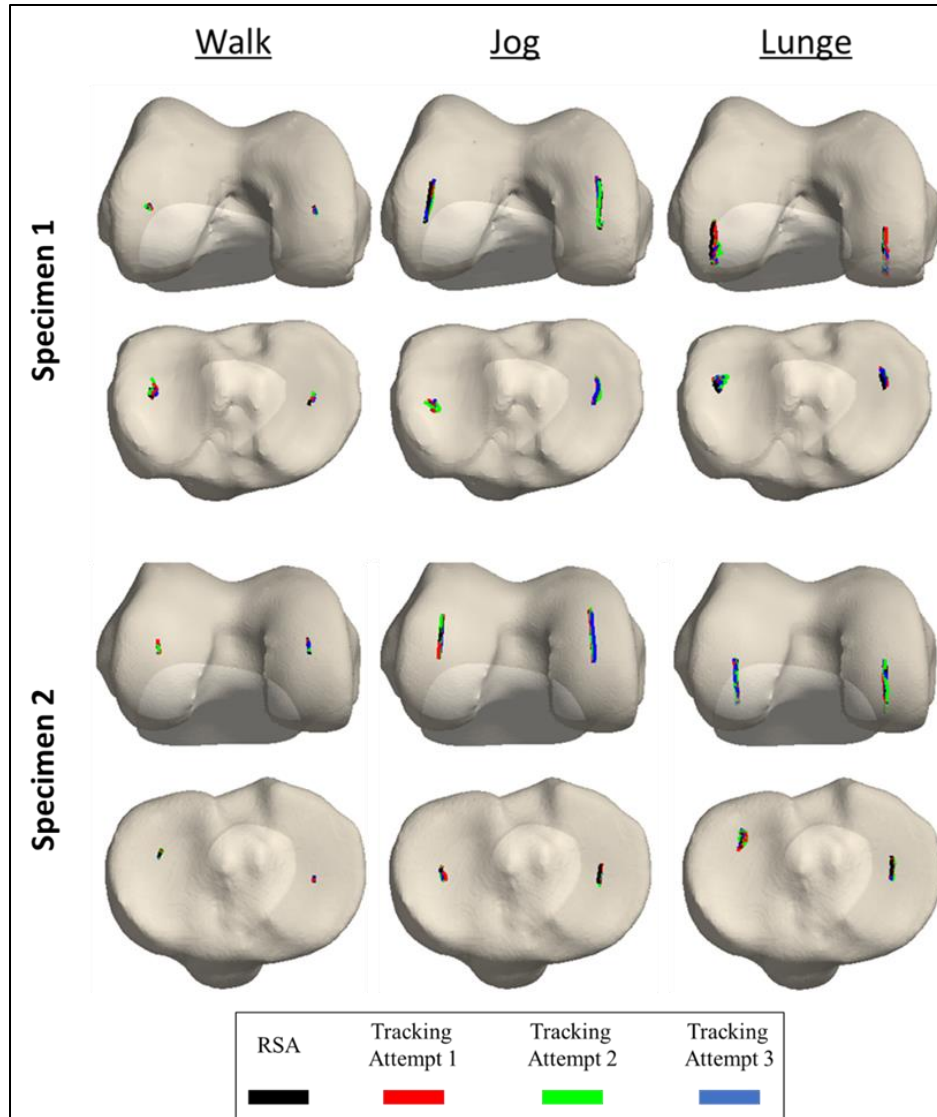


**Figure 6: The contact paths estimated from the RSA and the three tracking attempts (instances) of the without-interpolation solutions for both specimens and all dynamic activity types.**

For the arthrokinematic metrics, contact paths were qualitatively similar between the three tracking instances and RSA (

**Figure 6).** The largest errors occurred in the Lunge activities (**Figure 7**). The largest AP and ML excursion errors were  $0.8\pm 0.3$  mm and  $1.7\pm 0.5$  mm, both of which occurred in the lateral compartment of the tibia of the Lunge activities. The largest path location errors were  $1.3\pm 0.5$  mm in the lateral compartment of the tibia during the Lunge activities and  $1.3\pm 0.7$  mm in the medial compartment of the tibia for the Walk activities. The largest path location precision was  $0.7\pm 0.3$  mm in the lateral compartment of the tibia during the Lunge activities.

### **2.3.3. Interpolation and Intra-User Variability**

The average RMSE in nearly every DOF from all three dynamic activity types was lowest when the tracker did not interpolate (**Figure 8**), with several occurrences where the 6DOF kinematic errors were significantly different. For the Walk activity, there was a significant difference in joint angle measurement with effect of tracking instance in the FE DOF between tracking instances 1 and 2 and 2 and 3 ( $p = 0.03$ ), of which the differences of least squares estimates were  $-0.4^\circ$  and  $0.6^\circ$ , respectively. For the Jog activity, there was a significant difference in joint angle measurement with effect of tracking instance in the IE DOF between instances 1 and 2 and 2 and 3 ( $p = 0.048$ ), of which the differences of least squares estimates were  $-0.9^\circ$  and  $0.7^\circ$ , respectively. Also for the Jog activity, there was the only significant difference with effect of interval of frames interpolated ( $p = 0.046$ ). The difference occurred in the joint angle measurement of the FE DOF between interpolation intervals of 10 and 5 and between 10 and no interpolation. The differences of least squares estimates were  $0.2^\circ$  and  $0.3^\circ$ , respectively. There were no significant differences found in the Lunge activities (**Figure 9**).

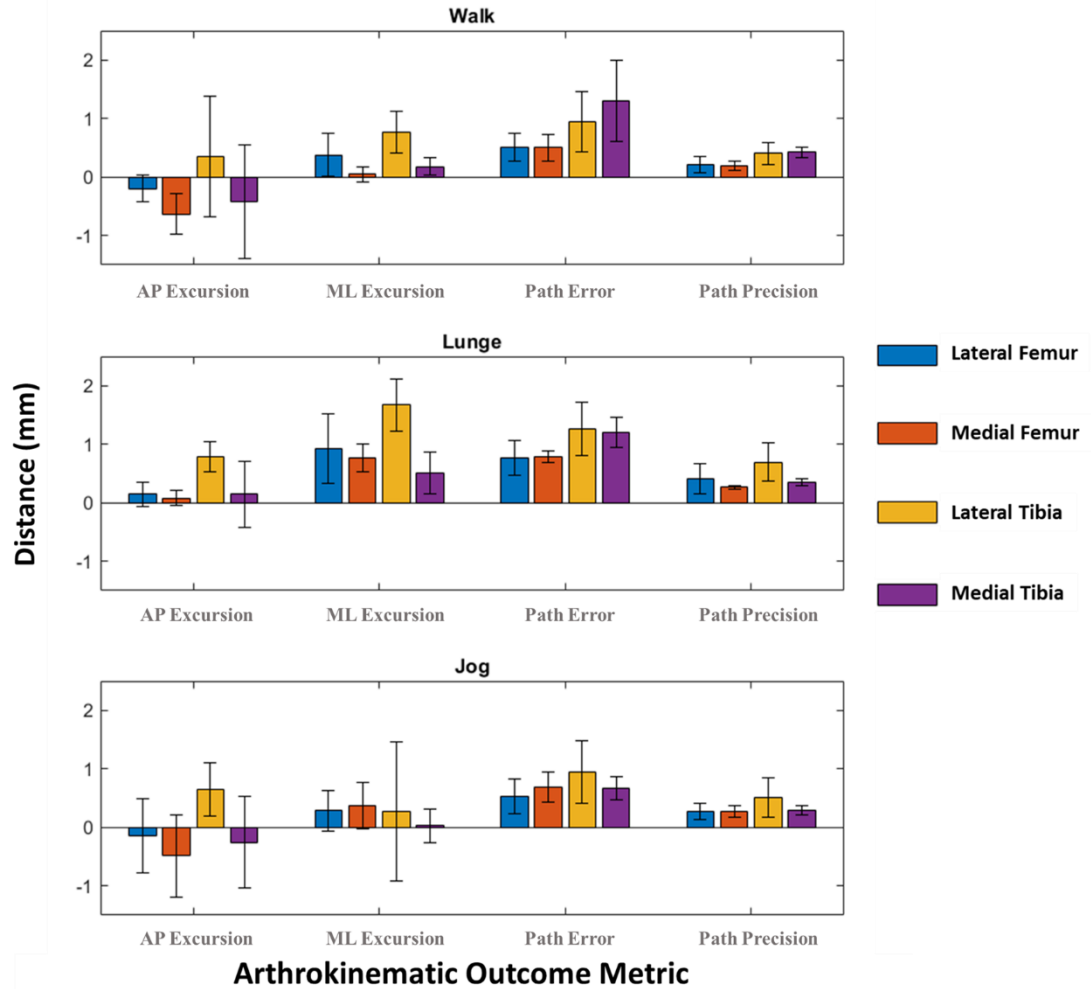


**Figure 7: The average RMSE across specimens and tracking instances of the arthrokinematic outcome metrics for the without-interpolation tracking technique compared to the RSA for each dynamic activity type.**

### 2.3.4. Arthrokinematic Metrics

There were no significant differences in tracking instance, frames, or interpolation on any of the arthrokinematic metrics (AP/ML excursion differences, and path location error/precision).

## 2.4. Discussion

The present study calculated the accuracy of kinematic and arthrokinematic outcome metrics by comparing to a gold standard RSA approach. Further, we determined how accuracy was affected when solutions were generated from three separate tracking instances (i.e. intra-user variability) and when using several interpolation techniques. We found that the interpolation techniques may be used without sacrificing kinematic or arthrokinematic metrics accuracy and that the errors associated with intra-user variability, while still small, were larger than the errors due to interpolation.

Several studies have quantified 6DOF kinematic measurement errors by comparing an MBT approach to an RSA approach [34,35,46]. The errors in the present study compare well to previously validated systems. For example, Anderst et al. presented a maximum RMSE of  $0.85 \pm 0.76^\circ$  in FE during a Static activity and  $1.75 \pm .61^\circ$  in FE during downhill running in human subjects [34]. Further, evaluation of the Mobile Biplane X-Ray Imaging System described by Guan et al. found the largest RMSEs using intact knees during walking to be 0.78 mm in ML translation and  $0.77^\circ$  in Ab-Ad rotation [46]. The maximum RMSE for a without-interpolation solution in the current study was  $0.6 \pm 0.3^\circ$  in IE rotation for a static activity and  $0.9 \pm 0.6^\circ$  in IE rotation during the dynamic Jog activities. The average calculated maximum knee velocity for the Walk and Jog activities (610 and 750 mm/s) compare well to the estimated speed of knee-joint motion during the stance phase of walking gait (700 mm/s) [46].

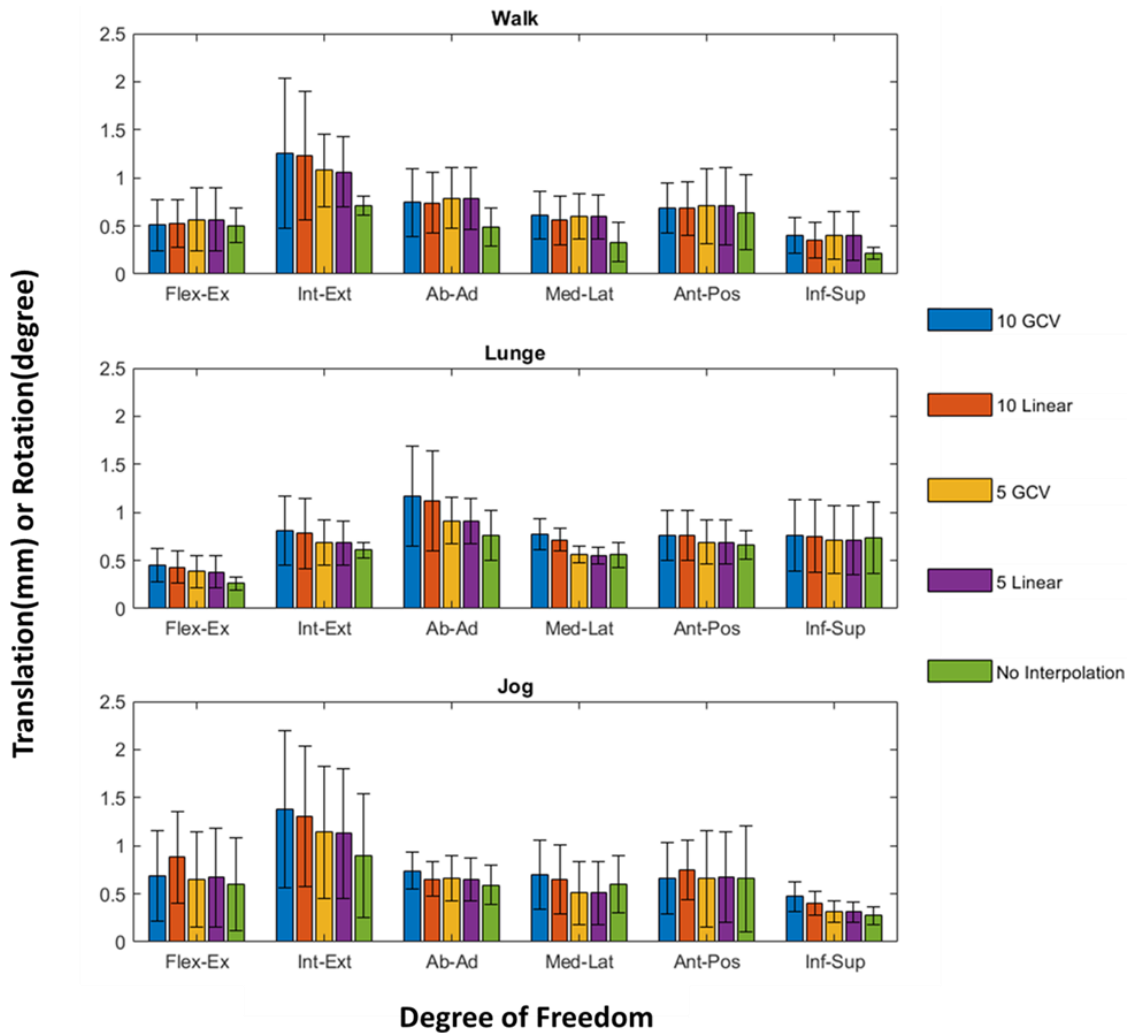


**Figure 8: The average RMSE across specimens and tracking instances of the 6 DOF for each of the tracking techniques compared to the RSA for each dynamic activity type.**

While no significant differences were found in arthrokinematic outcome metrics, the propagation of errors attributable to tracking was largest in the tibia, more specifically the lateral compartment (**Figure 6**). This is likely due to the geometry of tibial plateau subchondral bone being more planar in contrast to the convex geometry of the femoral condyle subchondral bone.

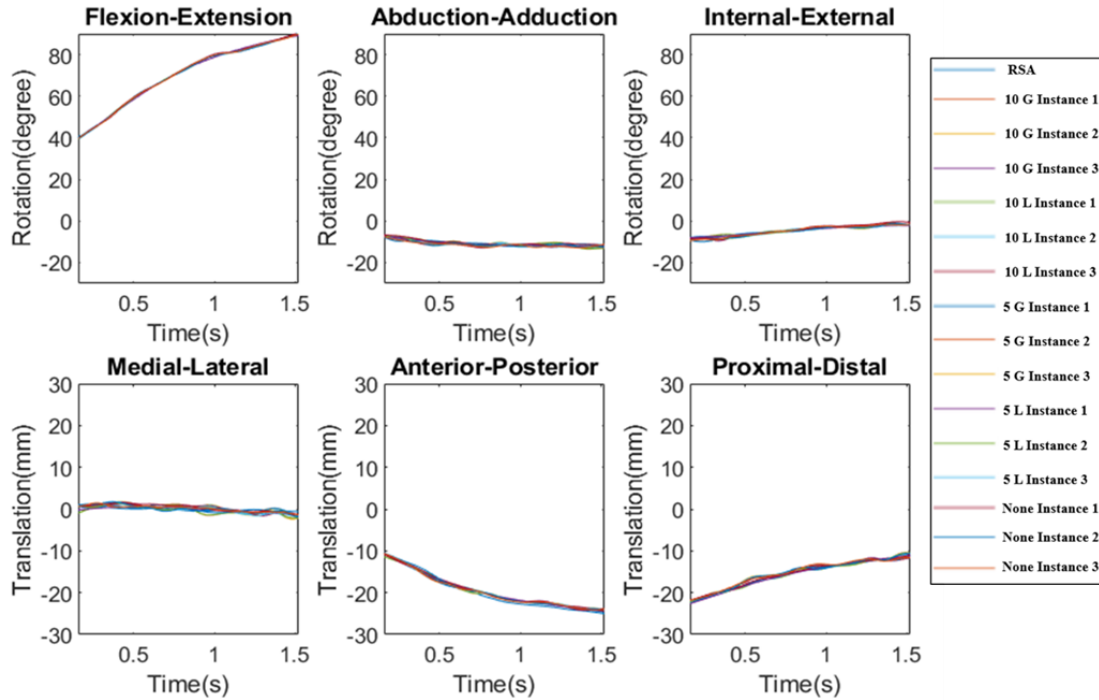


**Figure 9: The tracked 6DOF kinematics vs time of the Lunge activity for specimen 2 shows that the several MBT techniques closely resemble the RSA. Instances 1, 2, and 3 represent the three different pose map solutions generated from three separate tracking instances. 10 and 5 represent the interval of frames solved for, while G and L represent a GCV and Linear interpolation technique, respectively. None represents the solutions generated by solving every frame and not using interpolation. RSA represents the gold standard marker tracking. Flexion, Abduction, and External rotations are positive rotations, and Anterior, Proximal, and Lateral translations are positive translations of the tibia with respect to the fixed femur coordinate system.**

While RSA is considered acceptable as a gold standard for quantifying 6DOF kinematics, it is not entirely appropriate as a gold standard for estimating arthrokinematic metrics. The approach in the present study only accounts for errors due to tracking, not errors from bone model generation, dynamic joint space widths, and center of contact estimations. However, the point of the present study was only to understand how errors during the tracking process affect arthrokinematic metrics. Thorhauer and Tashman validated the accuracy of contact paths as compared to a true gold standard laser scanning method in load-bearing cadaveric

specimens and found maximum coordinate error biases of around 3 mm in either compartment [33]. Notable is that the laser scanning study and many recent studies have used articular cartilage models to estimate contact mechanics [33,59–62]. The decision to use bony geometry in the current study was made, again, to isolate errors resulting from the tracking process along with interpolation and to eliminate errors arising from segmentations. Still, DeFrate et al. compared the two approaches and found that they differ significantly only at low flexion angles [63].

Our descriptive statistics suggest that as the interval of frames interpolated increases, the greater the solution differs from the gold standard RSA approach. However, statistical tests only found one significant difference with effect of interpolation interval on the kinematics, and the largest mean difference was comparable to the largest average RMSE of the system without interpolating (0.3 mm vs. 0.9 mm, resp.). The small difference relative to the system's accuracy suggests that the magnitude to which the errors were affected by the interpolation interval was small. The type of interpolation was found to have no significant effect, though our data did show that the difference between the two interpolation techniques varies more as the interval of frames interpolated increases. The results suggest that intra-user reliability had the largest effect on accuracy, as there were multiple significant differences with effect of tracking instance and relatively large variances found between tracking instances. However, as with the effect of interpolation interval, the magnitude of the differences between tracking instances was similar to the RMSE, bias, and precision of the system.

Along with a low sample size of two specimens, there are several limitations to the present study that are noteworthy. The present study used cadaveric specimens that were manually manipulated to emulate walking, jogging, and lunging motions without bodyweight and muscle forces. Therefore, the kinematics and contact mechanics may differ from that of living human subjects. Moreover, the findings in the study depend on the sampling frequency and the interpolation interval; experiments that sample at faster frequencies than 125 Hz, or interpolate fewer frames may have smaller errors, and vice versa. Furthermore, CT resolution and fluoroscopy settings were optimized to image bead centroids and will likely differ in studies designed to image human subjects. Further investigation should quantify how alterations to the methods of generating bone models (CT slice thickness, CT in-plane resolution, mesh edge length, and mesh smoothing) affect the accuracy of arthrokinematic outcome metrics. Finally, the movements had relatively few sudden changes in direction. Therefore, data collections that involve movements with more changes in direction may suffer higher errors when interpolating untracked frames.

To our knowledge, the present study is the first to quantify the effects that intra-user variability and interpolation have on the accuracy of measuring kinematic and arthrokinematic outcome metrics using MBT. Results from the present investigation showed that the proposed system had submillimeter and sub-degree accuracy compared to RSA, and the described interpolation techniques were shown to have little to no effect on the accuracy of either 6DOF kinematic or arthrokinematic metrics. Ultimately, results from the present study enhance our ability to efficiently and accurately quantify kinematics and

arthrokinematics and will aid in the analysis and interpretation of data in future studies involving orthopaedic patient populations.

## **CHAPTER 3: TEST-RETEST AND SIDE-TO-SIDE RELIABILITY OF T1 $\rho$ AND T2\* MEASUREMENTS IN SMALL AND KNEE-SIZED PHANTOMS**

*A modified version of this chapter has been submitted for publication as: Ramsdell, JC., Beynon, BD., Borah, AS., Gardner-Morse, MG., Zhang, J., Krug, MI., Tourville, TW., Geeslin, M., Failla, MJ., Vacek, PM., Fiorentino, NM., (2023), "T1 $\rho$  and T2\* Measurements in Small and Knee-Sized Magnetic Resonance Imaging Phantoms: Effect of Phantom Size and Position Relative to Isocenter" Osteoarthritis Imaging*

### **3.1. Introduction**

Identifying changes in cartilage matrix composition prior to cartilage loss may inform the development of novel therapeutic interventions to prevent osteoarthritis onset and progression. Recent imaging advancements aim to capture changes in tissue composition using quantitative magnetic resonance imaging (qMRI) techniques [39], with a review of the literature concluding that qMRI parameters T1 $\rho$  and T2 reliably differentiate between healthy knees and those with osteoarthritis [40]. Establishing the reliability of qMRI parameters is an ongoing challenge due to the continued development of research-based image acquisitions and newer applications such as T2\* having received less attention in the literature.

The reliability of qMRI parameters is frequently assessed with an imaging phantom composed of liquid or gel placed at the center of the magnet (i.e. isocenter), where reliability refers to a repeated measure in the same imaging phantom. Imaging phantoms consist of either an array of smaller vials, usually arranged in a circular pattern, or one larger container. While the smaller phantoms permit simultaneous imaging of an array of qMRI relaxation times, the vial size is small compared to diarthrodial joints, and larger phantoms were designed with standard T1 and T2 imaging as the goal. Furthermore,

phantoms imaged at isocenter may generate misrepresentative results, as diarthrodial joints in the extremities are located to the side (left and right) of isocenter during imaging.

Therefore, the purposes of this study were to quantify the sources of variance and the systematic differences between left and right scanner positions in T1 $\rho$  and T2\* in small and knee-sized imaging phantoms.

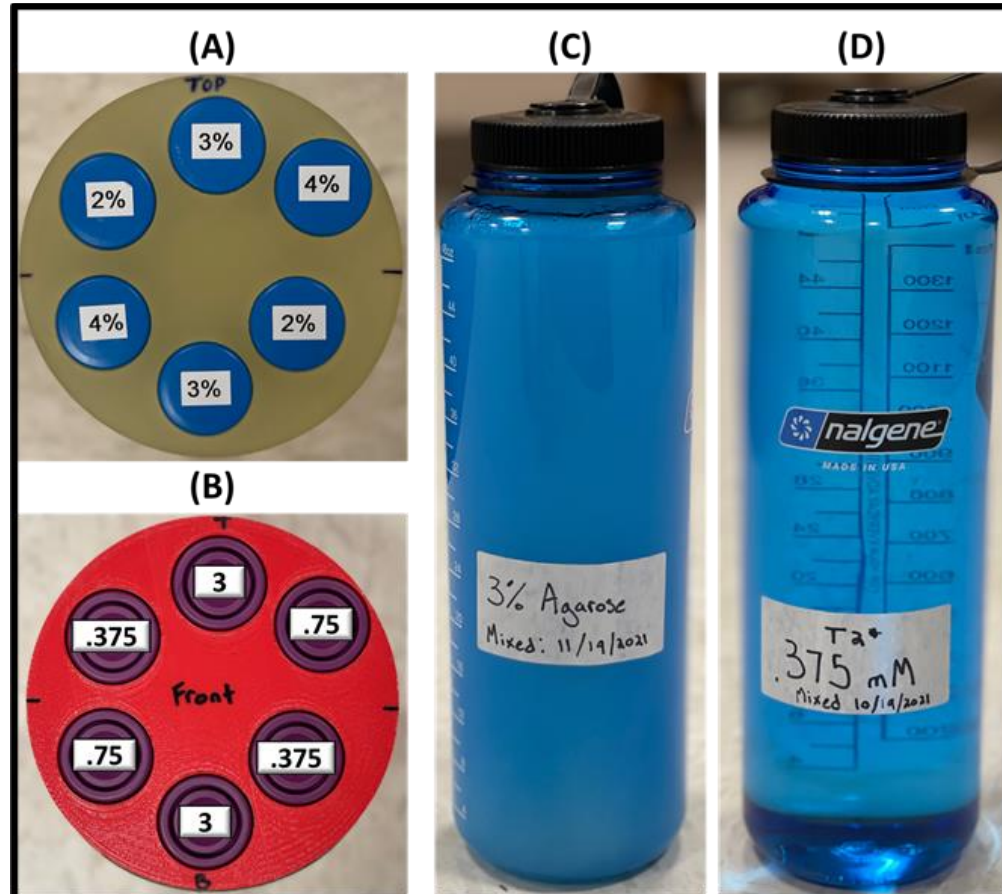


**Figure 10:** (A) Front view of small-vials phantom for T1 $\rho$  manufactured by The Phantom Laboratory, Inc. and (B) small-vials phantom for T2\* manufactured in-house. (C,D) Knee-sized phantoms for T1 $\rho$  and T2\* filled with in-house prepared gel and solution, respectively. Labels represent concentrations in percent agarose or mM of MnCl<sub>2</sub>.

## 3.2. Methods

### 3.2.1. Phantoms

For T1 $\rho$  imaging, a small-vials phantom was acquired that consisted of three pairs of vials (six total) of agarose gel (2, 3, and 4%) (The Phantom Laboratory, Inc.) [64] (Figure 10A). For T2\* imaging of small-vials, a similar phantom was manufactured in-house that consisted of three pairs of tubes of MnCl<sub>2</sub> solution (3, 0.75, and 0.375 mM) (Figure 10B) [65]. While the housing of the T2\* small-vials phantom was 3D-printed to mimic the geometry of the T1 $\rho$  small-vials phantom, the infill of the T2\* small-vials phantom was not solid like the T1 $\rho$  small-vials phantom. To replicate the size of a knee, two knee-sized phantoms of 89 mm in diameter and 285 mm in length (Nalgene™) were filled in-house with 3% agarose gel for T1 $\rho$  imaging and with 0.375 mM MnCl<sub>2</sub> solution for T2\* imaging (Fig. 1C,D).

### 3.2.2. MRI Data Acquisitions

The image series for T1 $\rho$  and T2\* quantification on both small and knee-sized phantoms were acquired with a 3.0T MR scanner (Achieva, Philips Healthcare, Best, The Netherlands) using a 16-channel transmit-receive RF knee coil. At each imaging session T1 $\rho$  and T2\* data for all phantoms were acquired at two locations: 100 mm to the left and 100 mm to the right of the scanner isocenter, which is similar to the locations of an *in vivo* scan setup for left and right knees of a subject. Location indicators on the RF coil and phantoms permitted consistent positioning of the phantom between scanning sessions. The left position was imaged first followed by the right, following our imaging center's standard protocol. A total of five imaging sessions were performed on different days. All

phantoms were kept in the scanner room that maintained a temperature of  $21 \pm 1^\circ \text{C}$  as measured by the thermostat in the scanner room and documented at the timing of scanning.

$T1\rho$  was measured using 3D magnetization prepared angle modulated partitioned k-space spoiled gradient echo snapshots (3D MAPSS) sequence [66]. Four spin lock times (TSL) of 0, 10, 40 and 80 ms at a spin lock frequency of 500 Hz with a variable flip angle (maximum  $70^\circ$ ) were acquired in a single acquisition to calculate the  $T1\rho$  relaxation time values. The small-vials phantom was acquired in the axial plane ( $140 \times 140 \times 96 \text{ mm}^3$  field-of-view (FOV), acquired matrix of  $280 \times 280 \times 32$  reconstructed to  $320 \times 320 \times 64$ ) and the knee-sized phantom was acquired in the sagittal plane ( $250 \times 140 \times 96 \text{ mm}^3$  FOV, acquired matrix of  $500 \times 280 \times 32$  reconstructed to  $512 \times 512 \times 64$ ). (See **Table 8a** in appendix for the  $T1\rho$  scanning parameters.)

$T2^*$  was measured using a 3D gradient echo sequence with spiral-out k-space and stack of spirals trajectory sampling strategies. The multi-acquisitions acquired with different echo times were used to calculate the  $T2^*$  map. For the small-vials phantom six echo times (0.61, 0.72, 1.0, 5.0, 15, and 30.0 ms) were acquired in the axial plane. For the knee-sized phantom five echo times (0.42, 1.0, 5.0, 15.0, and 30.0 ms) were acquired in the sagittal plane. Both phantoms were acquired with an  $8^\circ$  flip angle,  $140 \times 140 \times 96 \text{ mm}^3$  FOV, and a matrix of  $232 \times 232 \times 24$  reconstructed to  $320 \times 320 \times 48$ . (See **Table 9a** in appendix for the  $T2^*$  scanning parameters.)

### 3.2.3. Post-Processing

First, vials were automatically segmented [67] with custom developed [68] MATLAB software (The Mathworks Inc., Natick, MA). To avoid boundary effects near the edges of

the vials, region of interests (ROIs) were defined by fitting ellipses to the center of the vials with the smallest radii reduced by the vial wall thicknesses and an additional 10 pixels (small-vials phantom) or one half of the radius (knee-sized phantom) to form circular ROIs (Figure 11). To account for slice-to-slice variation, ROIs were generated in the central three center slices for every small-vials phantom and generated in the central 16 and 12 slices for the T1 $\rho$  and T2\* knee-sized phantoms, respectively. Each pixel within a ROI was fit with a mono-exponential function to generate relaxation times using the Levenberg-Marquardt [69,70] algorithm.

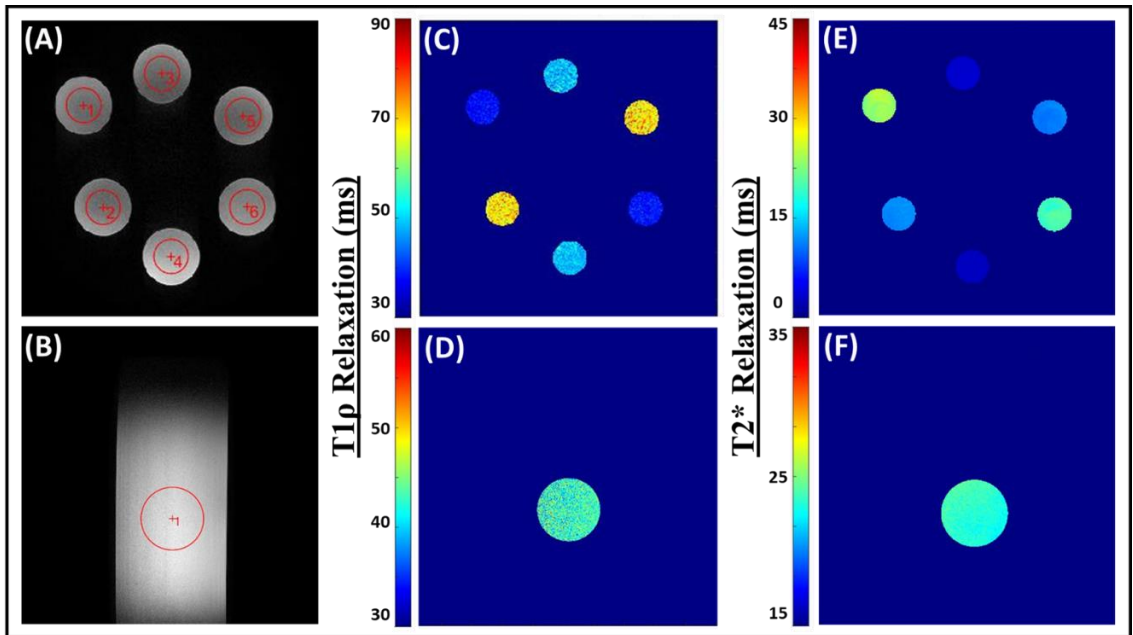


**Figure 11 (A,B) Example of ROI(s) in a single slice of both the small-vials and knee-sized phantoms for T1 $\rho$ . (C,D) Colormaps for the T1 $\rho$  relaxation times for each example ROI. (E,F) Colormaps for the T2\* relaxation times for each example ROI.**

### 3.2.4. Statistical Methods

Variance component analysis was used to obtain maximum likelihood estimates of the measurement variability attributable to the random effects of slice, side (i.e. left and right

position), and day for both phantoms. For the small-vials phantoms, the variability between vials of similar concentrations in the same acquisition was also estimated as a random effect. The precision of an individual measurement was estimated as 1.96 times the square root of the total variance. Paired t-tests were used to determine if systematic differences were present between the left and right imaging locations relative to isocenter from the same slice and day ( $p < .05$ ). Statistical analysis was performed using SAS Version 9.4 (SAS Institute, Inc., Cary, NC, USA).

### 3.3. Results

#### 3.3.1. T1 $\rho$ Acquisitions

The mean T1 $\rho$  relaxation times acquired across all days and both imaging positions were 66.0 ms, 44.8 ms, and 34.2 ms for the three pairs of 2, 3 and 4% agarose small-vials phantoms (**Table 2**). The measurement error tended to increase with increased relaxation time, with corresponding precision of  $\pm 2.7$  ms,  $\pm 1.5$  ms, and  $\pm 1.5$  ms, which expressed relative to the mean was 4%, 3%, and 4%, for the three pairs of 2, 3 and 4% agarose small-vials phantoms, respectively. The variance between sides in the 2% agarose concentration (0.94 of the 1.91 total variance or 49%) was the largest contributor to measurement variability in the small-vials phantom. The mean relaxation time and measurement precision for the 3% agarose knee-sized phantom were 42.6 ms and  $\pm 1.3$  ms with nearly all of the variability attributed to the between-day variance (0.413 of the 0.427 total variance or 97%). All small and large vial phantoms demonstrated significant differences between the left and right imaging locations relative to isocenter (**Table 3**). The average of

the left to right difference in relaxation times across days ranged from -1.5 ms ( $p < .001$ ) to -0.4 ms ( $p = 0.004$ ) for the small phantoms and was 0.1 ( $p < .001$ ) for the knee-sized phantom.

**Table 2: Mean T1 $\rho$  and T2\* relaxation times, variance components and measurement precision for small-vial and knee-sized phantoms (ms). Variance component analysis estimated the amount of variance attributed to vial, side (100mm to the left and 100mm to the right of isocenter), day, and slice. Total variance is the sum of all variance components. Precision of individual measurements was estimated as 1.96 times the square root of the total variance. Concentrations (Conc) listed as % agarose or mM of MnCl<sub>2</sub>.**

	Phantom	Vial # (Conc)	Mean (ms)	Variance Component Estimates				Total	Measurement Precision: $\pm$
				Vial	Side	Day	Slice		
T1 $\rho$	Small-vials	2&5 (2%)	66.0	0.2	0.9	0.4	0.4	1.9	2.7
		3&4 (3%)	44.8	0.0	0.2	0.3	0.1	0.6	1.5
		1&6 (4%)	34.2	0.2	0.2	0.2	0.0	0.6	1.5
	Knee-sized	(3%)	42.6		0.0	0.4	0.0	0.4	1.3
T2*	Small-vials	1&6 (0.375 mM)	23.4	2.8	0.0	0.3	4.0	7.0	5.2
		2&5 (0.75 mM)	11.7	1.1	0.0	0.0	0.1	1.1	2.1
		3&4 (3 mM)	3.1	0.0	0.0	0.0	0.0	0.1	0.5
	Knee-sized	(0.375 mM)	24.3		0.3	0.5	0.0	0.9	1.8

### 3.3.2. T2\* Acquisitions

The mean T2\* relaxation times across all days and both imaging positions were 23.4 ms, 11.7 ms, and 3.1 ms for the three pairs of 0.375, 0.75, and 3.0 mM MnCl<sub>2</sub> in the small-vials phantom (Table 2). Again, measurement error increased with an increase of relaxation times, with corresponding precision estimates of  $\pm 5.2$  ms,  $\pm 2.1$  ms, and  $\pm 0.5$  ms for the three pairs of 0.375, 0.75, and 3 mM MnCl<sub>2</sub> in the small-vials phantom. The total variance of the 0.375 mM MnCl<sub>2</sub> small vials was around seven times that of the other small vials, with the largest variance being between slices (4.0 of the 7.0 total variance or 57%). For the 0.375 mM MnCl<sub>2</sub> knee-sized phantom the mean relaxation time and measurement

precision were 24.3 ms and  $\pm 1.8$  ms, with the largest variance attributed to day (0.54 of the 0.87 total variance or 62%). Five of the six small-vials and the one knee-sized phantoms demonstrated a significant difference between the left and right imaging locations relative to isocenter (**Table 3**). The average magnitude of the left and right difference in relaxation times across days ranged from -3.3 ms ( $p < .001$ ) to 2.3 ms ( $p < .001$ ) for the small vial phantoms and was -0.8 ms ( $p < .001$ ) for the knee-sized phantom.

**Table 3: The mean, standard deviation (SD) and 95% CI of the difference in T1 $\rho$  and T2\* relaxation times between the left (L) and right (R) phantom positions for each vial (% agarose or mM of MnCl<sub>2</sub> concentration (Conc)). The L (100mm to the left of isocenter) and R (100mm to the right of isocenter) positions were chosen to replicate where the left and right knees would be located relative to isocenter during a scan of a human subject. T tests with a p-value less than 0.05 are bolded and show significant effects of position of phantom in the scanner at the time of acquisition.**

		Vial # (Conc)	Mean R-L differences (ms)	SD difference	95% CI	Pr >  t
T1 $\rho$	Small-vials	2 (2%)	-1.3	1.4	-2.2 to -0.4	<b>0.007</b>
		5 (2%)	-1.5	0.3	-1.7 to -1.3	<b>&lt; .001</b>
		3 (3%)	-1.0	0.2	-1.1 to -0.9	<b>&lt; .001</b>
		4 (3%)	-0.4	0.4	-0.6 to -0.2	<b>0.004</b>
		1 (4%)	-0.8	0.3	-1.0 to -0.6	<b>&lt; .001</b>
		6 (4%)	-0.5	0.3	-0.7 to -0.3	<b>&lt; .001</b>
	Knee-sized	(3%)	0.1	0.1	-0.1 to 0.1	<b>&lt; .001</b>
T2*	Small-vials	1 (0.375 mM)	-3.3	2.5	-4.7 to -1.9	<b>&lt; .001</b>
		6 (0.375 mM)	2.3	1.5	1.5 to 3.2	<b>&lt; .001</b>
		2 (0.75 mM)	0.4	0.4	0.2 to 0.6	<b>0.002</b>
		5 (0.75 mM)	<0.1	0.2	-0.1 to 0.2	0.543
		3 (3 mM)	-0.3	0.04	-0.3 to -0.2	<b>&lt; .001</b>
		4 (3 mM)	0.2	0.06	0.2 to 0.3	<b>&lt; .001</b>
	Knee-sized	(0.375 mM)	-0.8	0.3	-0.9 to -0.7	<b>&lt; .001</b>

### 3.4. Discussion

The purposes of this study were to quantify the sources of variance and the systematic differences between left and right scanner positions in T1 $\rho$  and T2\* in small and knee-sized imaging phantoms that closely resemble the *in vivo* condition in which measurements are made. To our knowledge, our study is the first to quantify the sources of variability attributed to slice, side (left and right of isocenter), and day for both T1 $\rho$  and T2\* measurements of small and knee-sized phantoms.

Our analysis showed that the total variances and contributing components of T1 $\rho$  and T2\* measurements differed between the small-vials and knee-sized phantoms. For the T1 $\rho$  small-vials phantom, a large percentage of the total variability was attributed to side (0.2 of 0.6 (38%), 0.9 of 1.9, (49%), and 0.2 of 0.6 (41%) for the three agarose concentrations). However, for the T1 $\rho$  knee-sized phantom, we found virtually no variability between side-to-side imaging locations. In the T2\* acquisitions, the total variance in the knee-sized phantom (0.9) was much less than that of the small-vials pair with the same MnCl<sub>2</sub> concentration (7.0) with virtually no variability between left and right imaging locations in the small-vials. We speculate that the 7x higher total variability in the T2\* small-vials phantoms compared to the knee-sized phantom is a result of the sensitivity of T2\* to field inhomogeneity artifact. To explore this, we acquired B0 field maps of the T2\* small-vials phantom and knee-sized phantom in the left and right positions of isocenter. We compared the knee-sized phantom and the small-vials phantoms of the same MnCl<sub>2</sub> concentration, with the knee-sized phantom as the reference. The difference in mean values ranged from -0.509 ppm to 0.130 ppm. We believe these values provide some credence to the argument

that field inhomogeneity may have played a part in the differences between phantoms; however, the extent to which inhomogeneity affected qMRI results in small-vials and knee-sized phantoms requires additional testing.

The data in Table 3 suggests that both T1 $\rho$  and T2\* values are affected by location of the phantoms within the scanner during data acquisition, as 13 of the 14 phantoms showed significant differences between the left and right imaging locations. While statistically significant, the average differences for eight of the 13 phantoms, including both small-vials and knee-sized phantoms, were less than one millisecond for T1 $\rho$  and T2\* (SD range 0.04 to 0.4 ms for eight phantoms with < 1 ms mean difference). In vivo work has found much larger differences in T1 $\rho$  between patients diagnosed with OA and healthy controls ( $48 \pm 3$  ms vs.  $62 \pm 8$  ms, respectively) [71], whereas differences in T2\* are relatively smaller than T1 $\rho$  but still larger than the side-to-side differences reported herein, such as those observed in patients after anterior cruciate ligament reconstruction and uninjured controls (mean difference range 4.3 – 4.6 ms) [72].

Positional dependence of the phantom relative to isocenter is small and may be due to the systematic acquisition of the left position before the right position. The radiofrequency applications in the left position may raise the temperature [73] of the phantoms' contents prior to acquisition on the right, and relaxation times are known to be sensitive to temperature changes [74]. To test this theory, we collected an additional data set where the small-vials phantoms were imaged twice on the left side of isocenter. For the small-vials T1 $\rho$  phantom, repeated scans on one side of isocenter resulted in changes that ranged from -0.1 ms to -0.3 ms, and corresponded to differences of 12% to 29% when expressed relative

to the mean differences reported in Table 3. For the small-vials T2\* phantom, the differences in T2\* from repeated scans ranged from -0.2 ms to 0.1 ms, and corresponded to differences of 2% to 5% for the vials with a significant difference in Table 3. Therefore, changes due to repeated scans may play a small role in T1 $\rho$  measurements and a minor role in T2\* measurements.

Our T1 $\rho$  means and variances of the small-vials phantom closely replicate that of previously reports that used the same model phantom acquired from the same manufacturer [64]. While the means and variances were similar, the prior study did not find a difference between 70 mm left and right of isocenter acquisitions [64], which was closer to isocenter than the acquisitions in the current study (100 mm). Contrary to the small-vials T1 $\rho$  phantom, it is difficult to compare results from the knee-sized T1 $\rho$  phantom and T2\* phantoms that we manufactured to those from other studies, as outcomes with similar phantoms have not been reported. Because the manufacturers differ, it is inappropriate to compare the means of the commercially manufactured T1 $\rho$  small-vial phantom to our in-house developed T1 $\rho$  knee-sized phantom with similar 3% agarose concentration. Lastly, to our knowledge, this is the first analysis of the reliability and the sources of variability associated with T2\* measurements in phantoms.

There are potential limitations associated with our study. While we have data to support that the temperature within the scan room did not fluctuate more than one degree, temperature of the phantoms at time of each acquisition was not recorded directly. Further, there is limited understanding of the shelf life (temporal stability) of agarose and MnCl<sub>2</sub> phantoms. This limits our ability to associate variability in day-to-day acquisitions with

scanning setup versus phantom change over time, or a combination thereof. In addition, we were only able to perform first order shimming of the magnetic field prior to scanning the small-vials phantoms, as compared to second order shimming for the knee-sized phantoms, and thus the differences between phantom sizes may be exacerbated due to the difference in order of shimming between the phantoms. To quantify the potential impact of differing orders of shimming, we measured  $T1\rho$  and  $T2^*$  in the knee-sized phantoms after first order shimming and after second order shimming. This revealed a difference of 0.2 ms in  $T1\rho$  and 1.1 ms in  $T2^*$ . The relatively higher value for  $T2^*$  indicates that the higher variance in Table 3 for the small-vials phantom compared to the knee-sized phantom may be due, at least in part, to the different orders of shimming applied to the phantoms.

Another potential limitation was that the scanning parameters were different between the small-vials and knee-sized phantoms due to their different geometries. The knee-sized phantoms were acquired sagittally as would be done in vivo and the small-vials phantoms were acquired axially, and this difference may have affected the qMRI parameters we found. Furthermore, the difference in slice orientation may have influenced the ‘slice’ variability in our analysis, as the slice direction for the small-vials was axial whereas the slice direction for the knee-sized phantoms was sagittal. In addition, our results may have been affected by our image processing methods, specifically the lack of a noise floor used in the data fitting model and the number of slices used in the analysis. Last, we chose not to include  $T2$  as a parameter due to its susceptibility to the magic angle effect [75]. Despite these limitations, the advantage of the phantom experimental design provides a low cost

means to measure qMRI parameters in a reference standard, which studies conducted in patients lack [76].

In conclusion, our results showed a position and phantom size dependence on  $T1\rho$  and  $T2^*$  relaxation time values that has not been reported previously. When studying the knee in humans, the results from this study motivate the use of knee-sized phantoms, especially for  $T2^*$  imaging of the knee, and will assist in interpreting future work that studies the effect of trauma, healing, and development of cartilage disease longitudinally.

## **CHAPTER 4: THE EFFECT OF ACUTE COMPRESSIVE LOADING IN THE HEALTHY KNEE ON T1 $\rho$ AND T2\* RELAXATION**

*A modified version of this chapter has been submitted for publication as: Ramsdell, JC., Beynnon, BD., Borah, AS., Gardner-Morse, MG., Zhang, J., Krug, MI., Tourville, TW., Geeslin, M., Failla, MJ., DeSarno, M., Fiorentino, NM., (2023), "Tibial and femoral articular cartilage exhibit opposite outcomes for T1 $\rho$  and T2\* relaxation times in response to acute compressive loading in healthy knees." *Journal of Biomechanics**

### **4.1. Introduction**

Quantitative magnetic resonance imaging (qMRI) parameters have generated much interest as potential biomarkers for detecting pre-arthritic alterations in populations at-risk for developing osteoarthritis (OA) [77–80]. Of particular interest, are the qMRI parameters T1 $\rho$  and T2\* that are associated with the matrix composition of articular cartilage. T1 $\rho$  relaxation has a negative correlation with proteoglycan content and a positive correlation with water content, and changes in T2\* relaxation have been shown to be correlated with changes in collagen matrix architecture [81,82]. Advancements in studying the composition of the cartilage may provide valuable information to aid in the development of novel therapeutic interventions to prevent OA onset and progression before irreversible morphological changes occur [83].

While loading is thought to play a key role in the progression of OA, traditional qMRI of knee articular cartilage is done with the knee in an unloaded state. The challenge of studying qMRI of the articular cartilage in a loaded state, is the need for an MRI-compatible loading device which are difficult to construct due to material and size constraints, and the requirement that the subject's knee remains motionless during scan acquisition [84]. As a result, our understanding of how the matrix composition of human

cartilage changes with the application of load is mostly limited. Currently, the only studies that have investigated the effects of acute loading on  $T1\rho$  relaxation of human knee articular cartilage in vivo, examine weightbearing region of interests (ROIs) that included both the tibial and femoral cartilage in contact with each other [85,86]. To our knowledge, there is no study that has attempted to assess the effects of acute loading on  $T2^*$  relaxation, nor the effects of  $T1\rho$  or  $T2^*$  in the human femoral and tibial articular cartilage separately. Further, it is unclear if a loading effect on qMRI is limited to the regions of cartilage directly transmitting the load as prior acute loading studies mainly focus on the cartilage contact area and not on region where cartilage is not in contact during application of load. A better understanding of how healthy tibial and femoral cartilage matrix content changes in response to load will aid in the identification of an abnormal response produced by injury or disease, and even educate cartilage models to understand structural properties of cartilage in-vivo.

Therefore, the specific aims of this study were to: 1) quantify the effect of acute compressive loading on  $T1\rho$  and  $T2^*$  relaxation in articular cartilage of the femur and tibia separately, 2) determine if the effect of load in the tibiofemoral regions that are in contact is consistent in non-contact regions, and 3) quantify the reliability of these measurements in a healthy population with normal knees. We hypothesize that there will be an effect of load, and that the effect of load on the femoral cartilage that is in contact with the tibia, will be significantly larger than that of femoral cartilage in non-contacting regions.

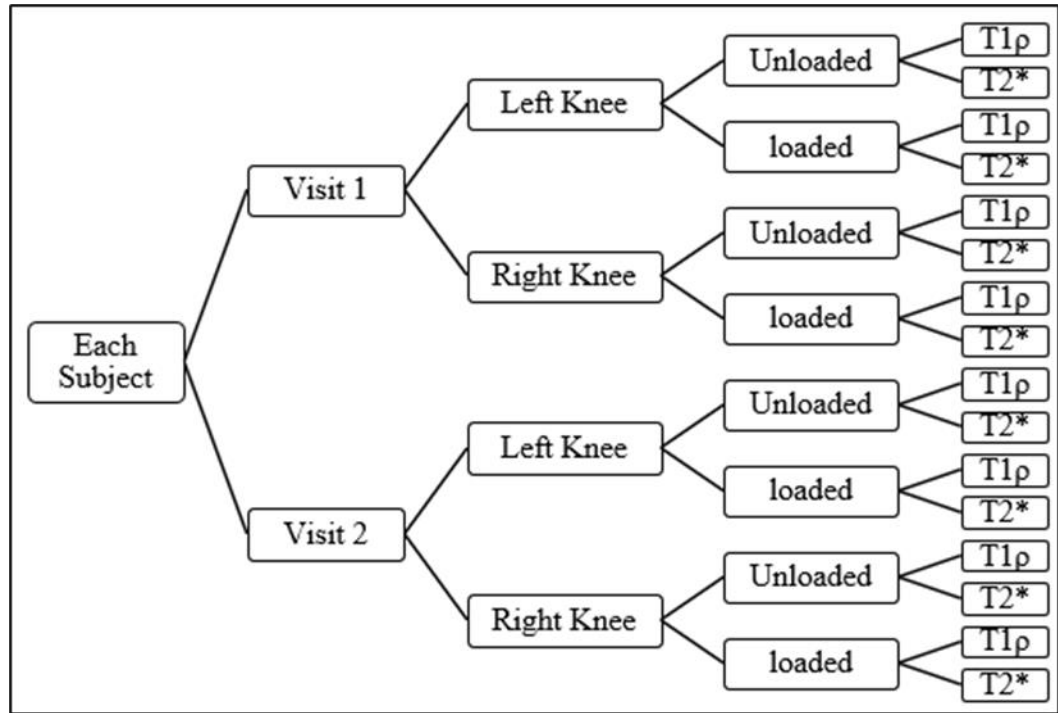


**Figure 12: Study outline for each of the 10 subjects enrolled involved two visits, with each knee being scanned in a loaded, and unloaded condition for a T1ρ and T2\* acquisition.**

## 4.2. Methods

### 4.2.1. Study Design

A total of 10 healthy subjects (6 male, 4 female, average age:  $23 \pm 2.4$  years) with no history of lower limb injuries provided written consent prior to participating in the study. Each subject was scanned at two timepoints  $7 \pm 3$  days apart on a 3T Phillips MR system with a 16 channel transmit-receiver RF coil (Figure 12). A scanning session included off-weighting the subject's left knee 15 minutes prior to MRI acquisitions. Then, T1ρ and T2\* images of the left knee were acquired with the subject supine in a traditional unloaded condition and again while the subject was supine and supporting a load of 40% bodyweight

(BW) as applied by the MRI loading device (Figure 13). This process was repeated for the right knee apart from the off-weighting as the subject's right knee was maintained non-weightbearing while scanning the left.

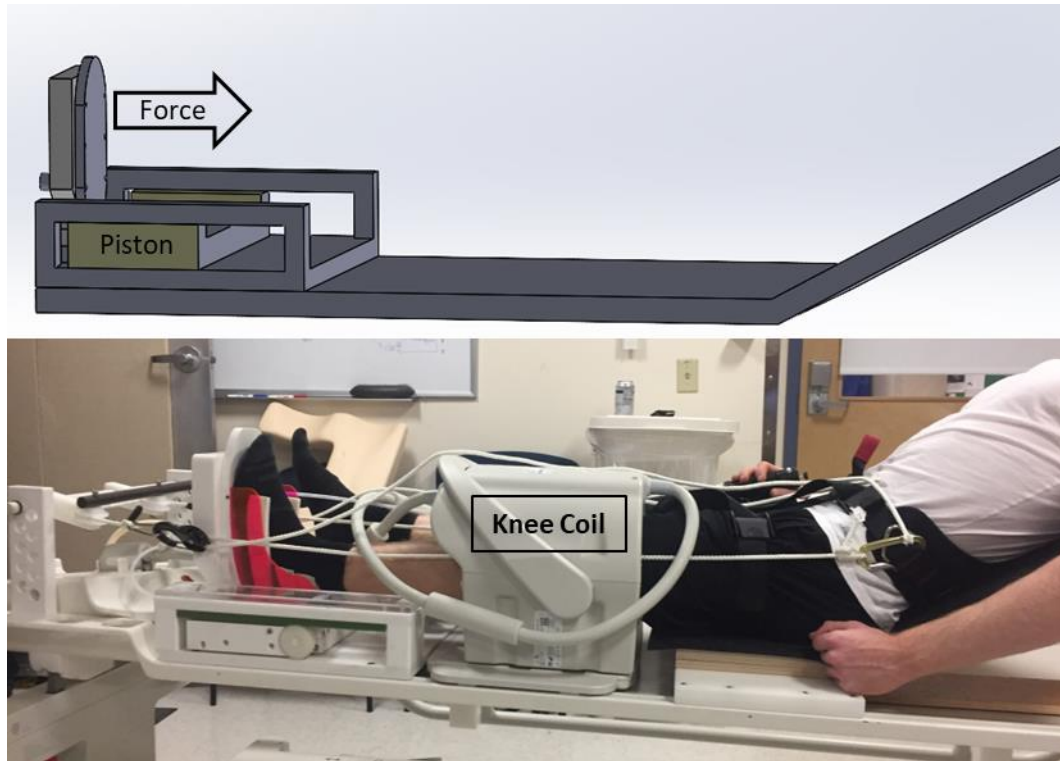


**Figure 13: The MRI loading device is driven pneumatically from the MRI control room. Researchers control the air pressure of two pistons that transmits a force directed superiorly from the foot. Participants are held in place via the combination of a climbing harness at the pelvis and the force of friction from the angled MRI tray.**

#### **4.2.2. MR Imaging**

$T1\rho$  was measured using three-dimensional (3D) magnetization prepared angle modulated partitioned k-space spoiled gradient echo snapshots (3D MAPSS) sequence [66]. Four spin lock times (TSL) of 0, 10, 40 and 80 ms at a spin lock frequency of 500 Hz with a  $70^\circ$  flip angle were acquired in a single acquisition to calculate the  $T1\rho$  relaxation values. Both visit one and visit two  $T1\rho$  acquisitions were acquired in the sagittal plane (250 (FH) x140 (AP)

x 96 (RL) mm<sup>3</sup> field-of-view (FOV), acquired matrix of 500x280x32 reconstructed to 512x512x64). (See Appendix Table 8a for the T1 $\rho$  scanning parameters.)

T2\* was measured using a 3D gradient echo sequence with spiral-out k-space and stack of spirals trajectory sampling strategies. The multi-acquisitions acquired with different echo times were used to calculate the T2\* relaxation times. For both visit 1 and visit 2, five echo times (0.42, 1.0, 5.0, 15.0, and 30.0 ms) were acquired in the sagittal plane. The specific acquisition parameters were: 8° flip angle, 140x140x96 mm<sup>3</sup> FOV, and a matrix of 232x232x24 reconstructed to 320x320x48. (See Appendix Table 9a for the T2\* scanning parameters.)

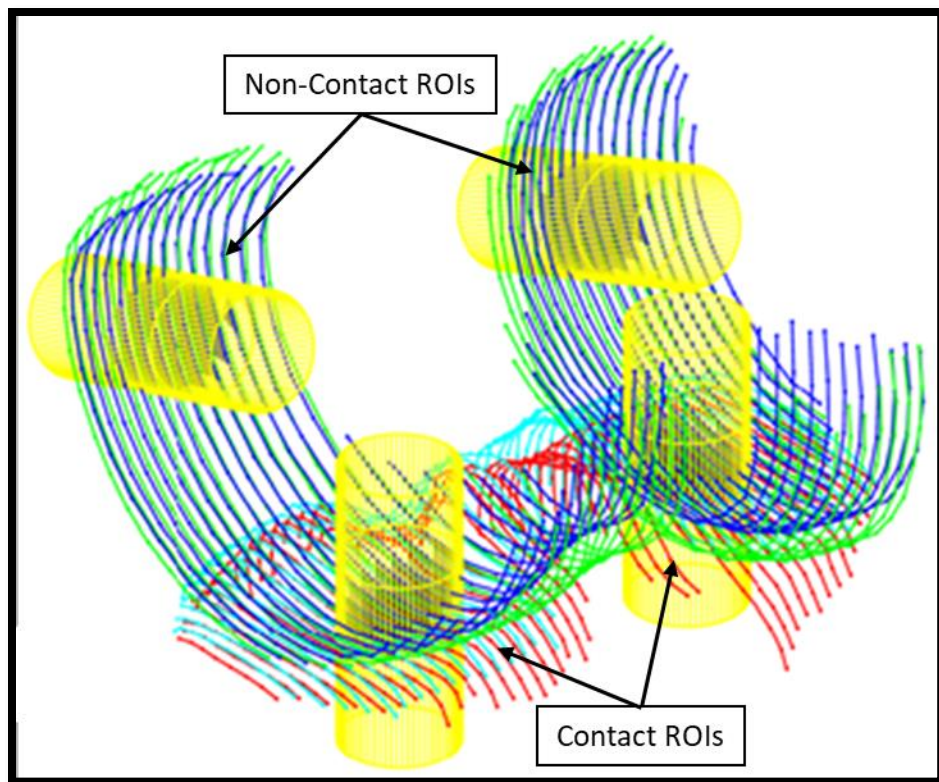


**Figure 14: Example tibiofemoral cartilage and subchondral bone segmentations with Non-contact and Contact ROIs shown in each compartment.**

### 4.2.3. Post-Processing

The articular cartilage and subchondral bone of the tibia and femur were manually segmented in the sagittal plane using OsiriX [87]. These segmentations were imported into a custom MATLAB (The MathWorks Inc., Natick, MA) software [88]. Two types of cylindrical ROIs that were 6mm in radius were defined in each compartment from the articular cartilage segmentations: 1) tibial and femoral contact ROIs that were directly subjected to the axial compressive loading from the loading device, and 2) noncontact ROIs located in the posterior femoral condyles that were not directly affected by the applied compressive load (Figure 14). For the contact ROIs, the centroid of the tibiofemoral cartilage-on-cartilage contact and the inferior-superior axis of the imaging volume defined the geometric center and long axis of the cylindrical contact ROIs in each compartment. For the noncontact ROIs, the centroid of the posterior femoral condyles not in contact with the tibial cartilage along with the surface normal at the centroid directed at a cylindrical axis fitted to the femoral condyles, defined the geometric center and long axis of the cylindrical noncontact ROIs. All cartilage voxels within the cylindrical ROIs were included in the analysis and the ROIs were defined by their bone (tibia and femur) and compartment (medial and lateral). Lastly, the ROIs were split into superficial and deep layers by their position in reference to half of the cartilage thickness.

For each MR acquisition, the spin lock/echo time image volumes were registered together by means of a 3D rigid body translation and rotation using ELASTIX [89]. All spin lock/echo time image volumes were registered to the spin lock/echo time image volume that the tissues were segmented on. For  $T1\rho$ , all spin lock time image volumes

were registered to the first spin lock time (0 ms) image volume, and for T2\* all echo time image volumes were registered to the third echo time (5 ms) image volume. To limit errors associated with the participant's limb shifting during an acquisition, three scans were excluded from the analysis due to poor image volume registrations. The spin lock/echo time signals for each pixel within a ROI were fit with a mono-exponential function to generate relaxation times using the Levenberg-Marquardt [69,70] algorithm. The average of the relaxation times based on all the pixels within an ROI was calculated and used to represent the T1 $\rho$  or T2\* relaxation time for that ROI.

#### **4.2.4. Statistical Analysis**

Mixed model repeated measures analysis of variance tested if T1 $\rho$  and T2\* relaxation times in each of the 8 contact ROIs were significantly different when loaded (Aim 1), and if the effect of load in the femoral cartilage (difference in T1 $\rho$  and T2\* relaxation times between loaded and unloaded conditions) was significantly different between the contact femoral ROIs and the matched noncontact femoral ROIs (Aim 2). To address the third Aim, mean differences, upper/lower 95% confidence limits (LCL/UCL), and p-values were calculated to test if the difference between load and unloaded conditions were repeatable between visits 1 and 2.

### **4.3. Results**

Significant differences ( $p < .05$ ) in T1 $\rho$  relaxation were found between the unloaded and loaded conditions in all contact ROI (Figure 15). However, the femoral and tibial contact ROIs demonstrated opposite responses as the T1 $\rho$  relaxation in the femoral contact ROIs increased with application of the compressive load, while T1 $\rho$  relaxation times in the tibial

contact ROIs decreased with the application of compressive load. The mean effect of load on T1 $\rho$  relaxation ranged from 4.1 to 7.1 ms, and -1.5 to -5.5 ms in the femoral and tibial contact ROIs, respectively. For T2\*, there were significant differences between loaded and unloaded conditions in every femoral contact ROI, but in tibial contact ROIs only the medial-deep ROI was significantly different. The mean effect of applied load on T2\* relaxation ranged from 3.7 to 13.3 ms, and -2.0 to 0.7 ms in the femoral and tibial contact ROIs, respectively. The effect of load on the femoral contact ROIs in the deep cartilage (13.4ms [lateral] and 13.3 ms [medial]) were much larger than that of the superficial cartilage (3.7ms [lateral] and 5.3 ms [medial]).

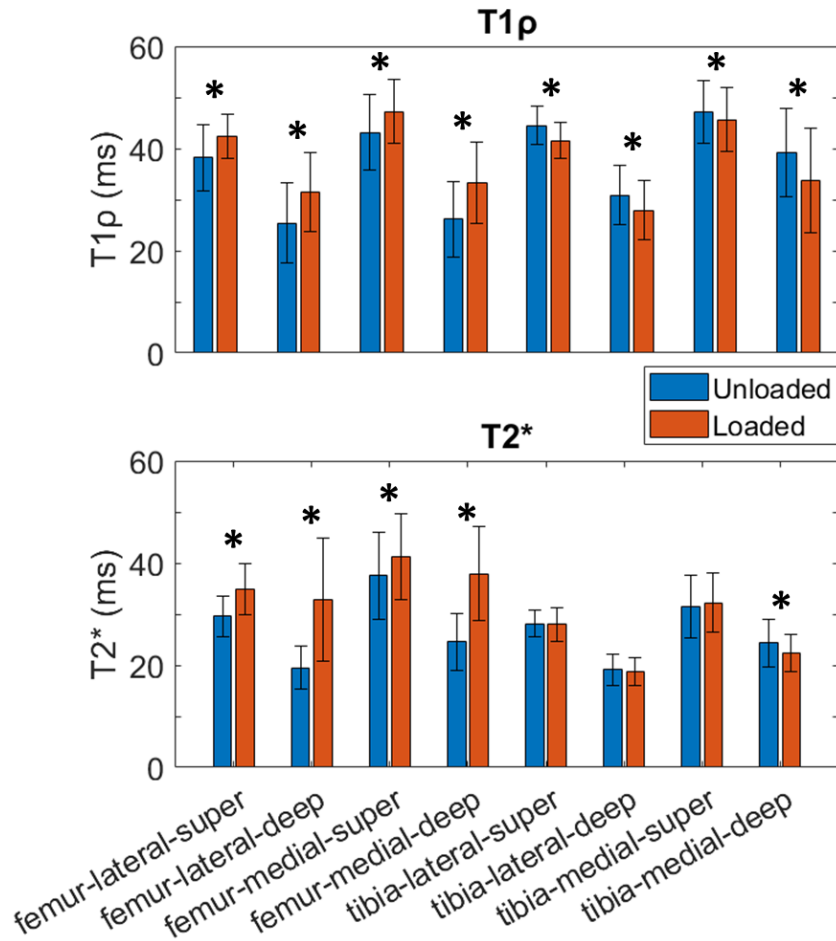


**Figure 15: Relaxation times in the unloaded and applied compression loaded conditions of the 8 contact ROIs for both T1ρ and T2\*. The “\*” symbol represents a significant difference (p<0.05) in relaxation time between the unloaded and applied compression loaded condition.**

The mean effect of load in the femoral cartilage on both T1ρ and T2\* was larger in all four of the femoral contact ROIs than in the femoral noncontact ROIs (Figure 16). Only T1rho in the lateral-deep femoral cartilage did not show a significant difference (p = 0.1) in the effect of load between the contact and non-contact regions (Figure 17). The mean difference in effect of load between the femoral noncontact and contact ROIs ranged from 2.2 to 8.9 ms and 2.8 to 9.9 ms for T1ρ and T2\*, respectively.

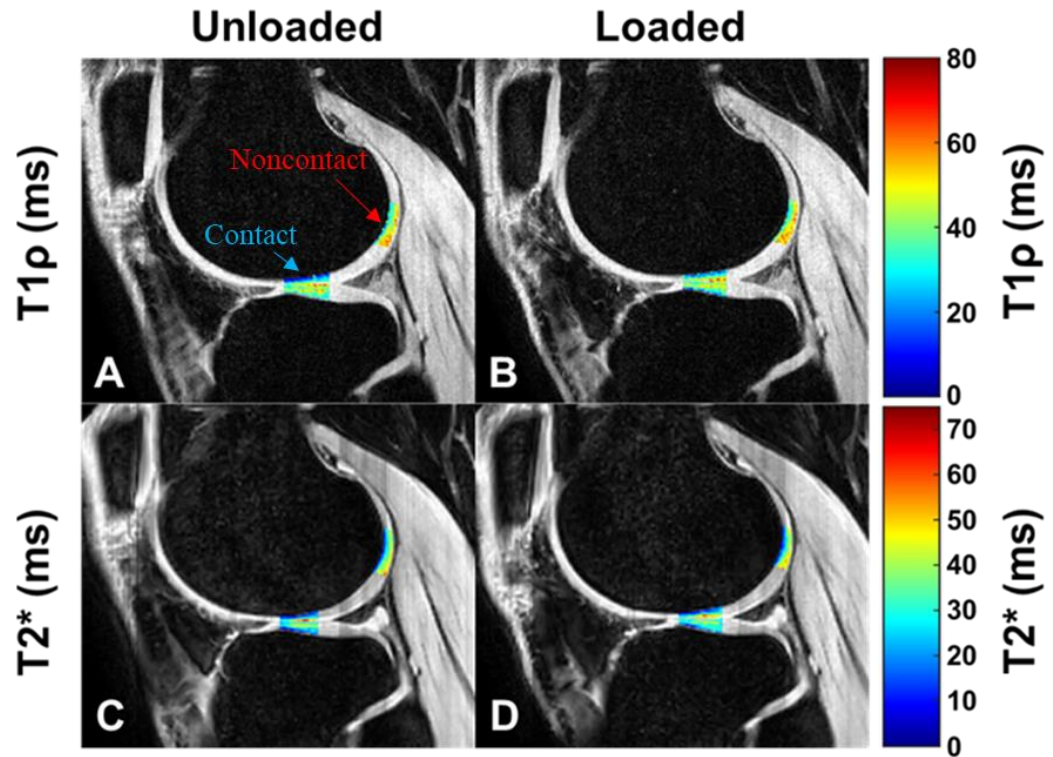


**Figure 16: Example of sagittal T1 $\rho$  (A, B) and T2\* (C, D) images with noncontact and contact ROIs shown for both the unloaded (A, C) and loaded (B, D) conditions. Pixels with the ROIs are color mapped to their respective relaxation times (color bar on righthand side).**

There were no significant differences in effect of applied compressive load on T1 $\rho$  or T2\* relaxation values of all contact ROIs between visit 1 and visit 2 (Table 4). The mean differences in effect of load between visit 1 and visit 2 in all contact ROIs ranged from -1.6 to 2.9 ms and -1.5 to 0.5 ms for T1 $\rho$  and T2\*, respectively.

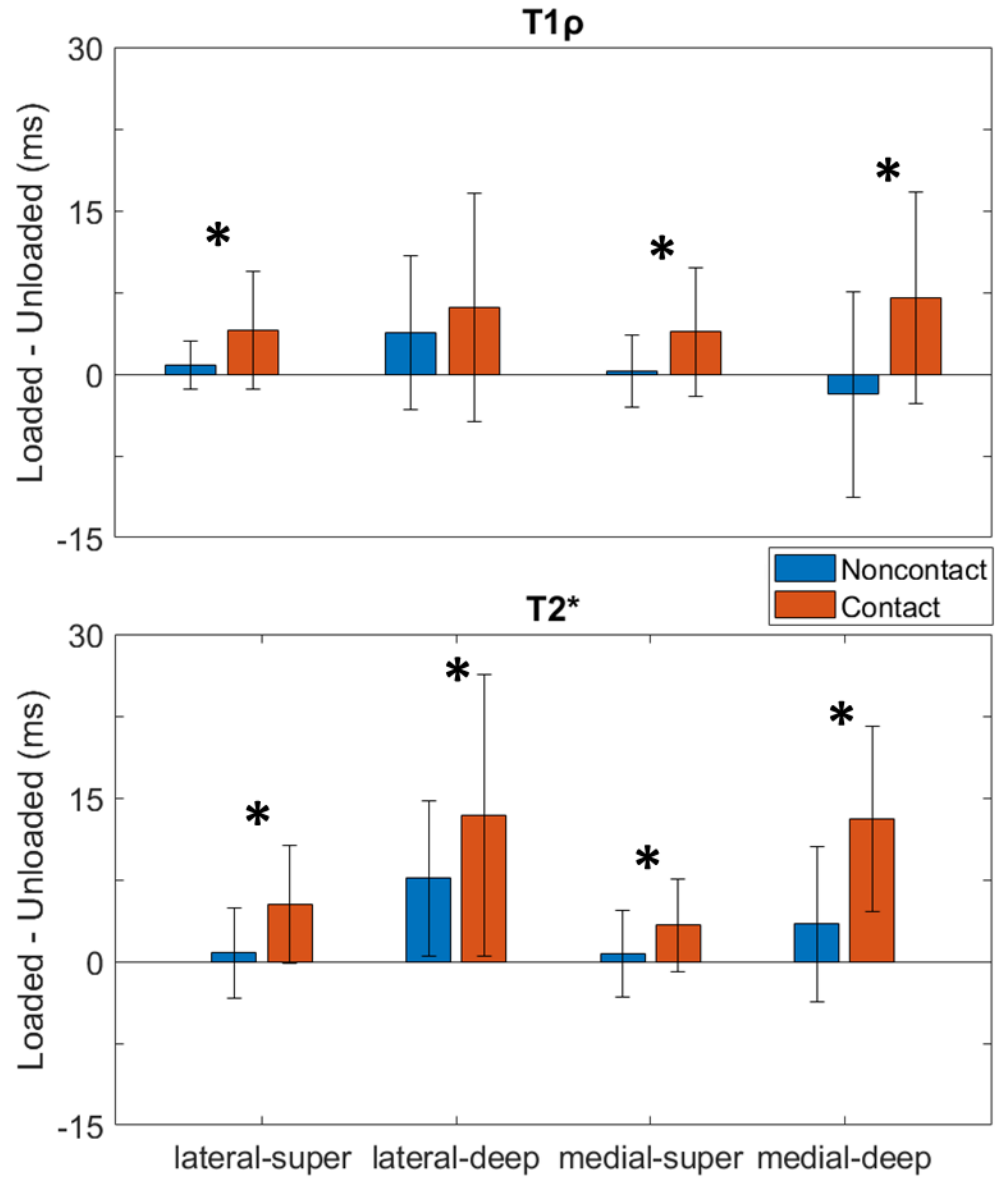


**Figure 17** For the 4 femoral ROIs, the mean differences in relaxation times (calculated as the unloaded conditions subtracted from the applied compression load conditions) between the contact region and the noncontact regions. Data are presented for both T1ρ and T2\* assessments (ms). The “\*” symbol represents a significant difference (p<0.05) of effect of load between the femoral contact region and femoral noncontact regions.

#### 4.4. Discussion

Our hypothesis that the application of a compressive load to the knee will have a significant effect on qMRI measurements of articular cartilage was consistent with the present investigation's results for T1 $\rho$  relaxation times, and only partially consistent with the results for T2\* relaxation times. This hypothesis is supported on the grounds that every contacting ROI for T1 $\rho$  showed a significant effect of applied compressive load, whereas for T2\*, every femoral and only the medial-deep-tibia contact ROI showed a significant effect of applied compression load. We found that the changes in T1 $\rho$  and T2\* relaxation times for the femoral non-contacting ROIs in response to the compressive loading was significantly smaller than the changes in the femoral contacting ROIs. Further, we determined the response to load to be a repeatable measurement one week apart, as we found no significant differences in effect of load on T1 $\rho$  or T2\* of any contact ROI between visit 1 and visit 2 (Table 4).

However, the most notable finding was that the femoral and tibial contacting cartilage demonstrated opposing effects on qMRI parameters between the unloaded and the 40% BW loaded conditions. To our knowledge, this is the first study that analyzed the effects of T1 $\rho$  and T2\* on acute loading in the human femoral and tibial cartilage as unique and separate structures. Nevertheless, A similar study by Hamanda et al. examined the effect of acute loading on the T1 $\rho$  relaxation of femoral weightbearing cartilage in porcine knee models [90]. Contrary to the present investigation, this study found a decrease in T1 $\rho$  in the femoral cartilage and did not analyze the tibial cartilage as the authors reported it was too thin. In porcine knees, the thickness of the tibial cartilage is reportedly half that of

the femoral cartilage[91]. This is not the case for healthy adult human cartilage where tibial and femoral cartilage are more similar in thickness in the regions that we analyzed, which may explain the different results found between the two investigations [27,92]. Unlike the present study, Subburaj et al. showed opposing responses to load between the deep and superficial contacting cartilage on T1 $\rho$  [86]. However, this study combined the femoral and tibial cartilage within the same deep or superficial ROI and may explain the differences in results. Similar to the present study, Heckelman et al. performed T1 $\rho$  scans on healthy knees immediately after running 3 and 10 miles that showed an increase in T1 $\rho$  values in the femoral cartilage and a decrease in the tibial cartilage with increased running duration[93]. While the application of load between this prior study and the present study are different, it should be noted that opposing responses to loading on qMRI between tibial and femoral cartilage have been observed.

A significant change in these qMRI parameters with the addition of load suggests the composition of the cartilage matrix within the ROI was altered. T1 $\rho$  and T2\* have been shown to be negatively correlated with proteoglycan content and positively correlated with water content [81,82]. Thus, a reduction in the qMRI parameters of the tibial cartilage with the addition of load suggests water loss and an increase in proteoglycan concentration, though an actual increase in proteoglycan concentration is more likely due to water loss and deformation [94]. Concurrently, the results from the femoral contact cartilage, which showed an opposing response to load, suggests a water gain and swelling. This introduces the hypothesis that the net flux of fluid between the femoral and tibial cartilage is different following the addition of a 40% BW load. The work of Li et al. has shown that the

mechanical properties and the concentration of cartilage components in a canine knee differ depending on the region sampled [95]. Therefore, A possible explanation is that the regions of tibial and femoral cartilage we compared have different mechanical properties and thus different water permeabilities.

**Table 4: T1 $\rho$  and T2\* mean responses to load (difference between unloaded and loaded conditions) of each contacting ROI in relaxation times (ms) between visits 1 and 2. Presented are lower/upper 95% confidence limits (LCL/UCL), and p-values.**

	ROI	Visit 1		Visit 2		Mean Diff.	LCL	UCL	p-value	
		Mean	Std. Dev.	Mean	Std. Dev.					
T1 $\rho$	Tibia	lateral-super	-2.60	2.64	-3.50	2.54	-1.01	-2.21	0.18	0.16
		lateral-deep	-3.10	4.51	-3.08	6.50	-0.12	-3.51	3.27	0.99
		medial-super	-0.99	2.75	-2.47	2.68	-1.58	-2.97	-0.19	0.05
		medial-deep	-5.92	9.00	-5.09	9.88	0.72	-5.92	7.36	0.79
	Femur	lateral-super	3.70	4.62	4.32	6.14	0.60	-2.64	3.83	0.71
		lateral-deep	4.55	8.36	7.64	12.22	2.86	-2.17	7.89	0.30
		medial-super	3.40	5.78	4.36	6.12	1.52	-2.11	5.16	0.57
		medial-deep	6.85	9.43	7.15	10.16	0.76	-4.18	5.70	0.82
T2*	Tibia	lateral-super	0.40	2.60	-0.97	3.31	-1.48	-3.31	0.34	0.12
		lateral-deep	-0.39	3.09	-0.65	2.60	-0.16	-2.10	1.79	0.69
		medial-super	0.74	4.25	0.51	2.95	0.29	-1.44	2.02	0.96
		medial-deep	-2.35	4.44	-2.01	3.27	0.53	-1.82	2.88	0.80
	Femur	lateral-super	6.37	5.69	3.95	4.95	-1.26	-4.68	2.16	0.19
		lateral-deep	13.59	10.97	13.16	15.02	0.23	-6.56	7.02	0.93
		medial-super	4.02	5.13	2.52	3.08	-0.51	-3.14	2.13	0.34
		medial-deep	13.30	8.06	12.88	9.18	-0.94	-5.64	3.76	0.89

Various approaches of selecting ROIs have been employed to studying cartilage with qMRI. The present study analyzed contacting cartilage with a fixed radius ROI to 1) analyze a region that is exposed to the largest effect of load, 2) limit the differences in cartilage sampled between the unloaded and loaded conditions, and 3) choose an approach where the analyzed region is reproducible in both a normal and diseased knee (such as a meniscectomy) that may be used to make side-to-side comparisons [96,97]. While there is evidence that the cartilage over the meniscus bears load, prior research has shown larger differences in qMRI with the addition of load occurring in the cartilage-cartilage contacting zones [98,99]. Additionally, a fixed radius was used as opposed to analyzing the full area of contacting cartilage because the cartilage contacting area increases with load and can differ between a healthy and diseased conditions [100]. Additionally, the present study analyzed the non-contacting region of the femur to act as a within scan acquisition noncontact control. The result showed the effect of load was larger in the contact regions than in the noncontracting regions of the femoral cartilage which support the hypothesis that the change in qMRI measurements between an unloaded and loaded scan was attributable to the application of compressive load by the loading device.

There are several limitations to the present study that are noteworthy. Firstly, acquisition parameters were chosen to maximize image quality while simultaneously reducing the amount of time subjects were loaded in the loading device. Thus, we chose to use a fewer number of spin locks and echoes than that of typical qMRI acquisitions to reduce the amount of time the subjects were loaded while recognizing that the accuracy of our measurements may be affected. Quantifying the effect of load on a particular ROI

presented a unique problem as the tissues within the knee were free to move and deform in response to the application of load. As detailed in the text above, much thought went into the ROI selection to limit the differences in regions of cartilage sampled between unloaded and loaded conditions. However, differences may still exist. Still, we feel any differences are small, since the position of the tibia relative to the femur has been shown to translate less than 1mm in healthy knees as per direct radiographic measurements of bone position in response to a similar application of 40% BW compressive load relative to the unloading condition [101].

To our knowledge, this is the first study that analyzed the effects of acute loading on T1 $\rho$  and T2\* measurements in the human femoral and tibial cartilage separately. The data from this study suggest that the effect of acute loading at 40% BW on the qMRI measurements was: 1) opposing in the femoral and tibial cartilage; 2) larger in the cartilage contacting regions than in the non-contacting regions of the femur cartilage; and 3) was repeatable between two visits separated by one week. The results from this study introduce a new hypothesis that the direction of the flux of fluid between the femoral and tibial contacting cartilage may be opposing in response to a 40% BW load. Ultimately, the results will aid in the analysis and interpretation of data in future studies involving orthopaedic patient populations.

## **CHAPTER 5: SIDE-TO-SIDE AND VISIT-TO-VISIT REPEATABILITY OF QMRI METRICS IN HEALTHY KNEES**

### **5.1. Introduction**

Investigations have reported wide ranges in their ability to repeatably measure qMRI in human articular cartilage and there is relatively no understanding of the repeatability of qMRI measurements with the use of MRI loading devices [40]. A lack of agreement between investigations on the repeatably of qMRI is likely due to different approaches of quantifying qMRI metrics including differences in postprocessing techniques such as region of interest (ROI) selection.

Therefore, one purpose of this study was to quantify the side-to-side (i.e. left versus right knee) and visit-to-visit repeatability of qMRI metrics in healthy subjects in an unloaded and loaded condition. Another purpose of this study was to determine how ROI selection effects the repeatability of the qMRI measurement. We hypothesized there will be no effect of side and visit on qMRI metrics unloaded or loaded, and that the repeatability of these measurements will improve with larger ROI size.

### **5.2. Methods**

#### **5.2.1. Dataset**

This study used the same dataset from the previous chapter in section **4.2**.

### **5.2.2. Post-Processing**

Five levels of ROIs were defined in each acquisition. The first level (laminar plug) included 8 ROIs that were defined as the tibial and femoral contacting cartilage plugs (described fully in the previous section [4.2.3]). These included a deep and superficial ROI for each compartment and each bone. The second level (combined plug) included 4 ROIs and was similar to the first level but combined the deep and superficial layers. The third level (full volume by compartment) also had 4 ROIs but included all segmented cartilage in the medial and lateral compartments of both the femoral and tibial cartilage. The fourth level (full volume by bones) included all segmented cartilage of each bone. The fifth and final level (full volume) included all segmented cartilage from both bones.

### **5.2.3. Statistical Methods**

Mixed model repeated measures analysis of variance tested if T1 $\rho$  and T2\* relaxation times in each ROI were significantly different between the left and right limbs, and between visits. Statistical significance level alpha was set a priori at 0.05. Statistical analyses were conducted using SAS statistical analysis software, version 9.4 (SAS Institute, Inc., Cary, NC, USA).

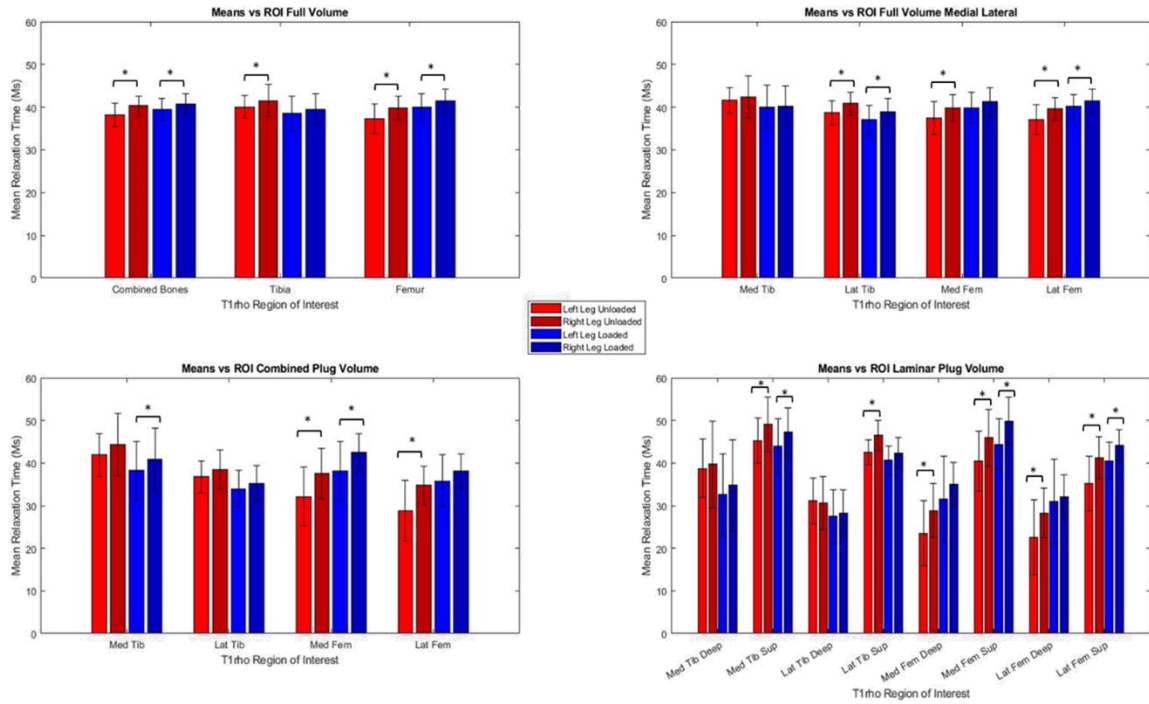


**Figure 18: T1rho relaxation in each ROI for both the left (light) and right (dark) legs in the unloaded (red) and loaded (blue) conditions. Significant differences are indicated by a \* symbol and 95% confidence intervals are represented by error bars.**

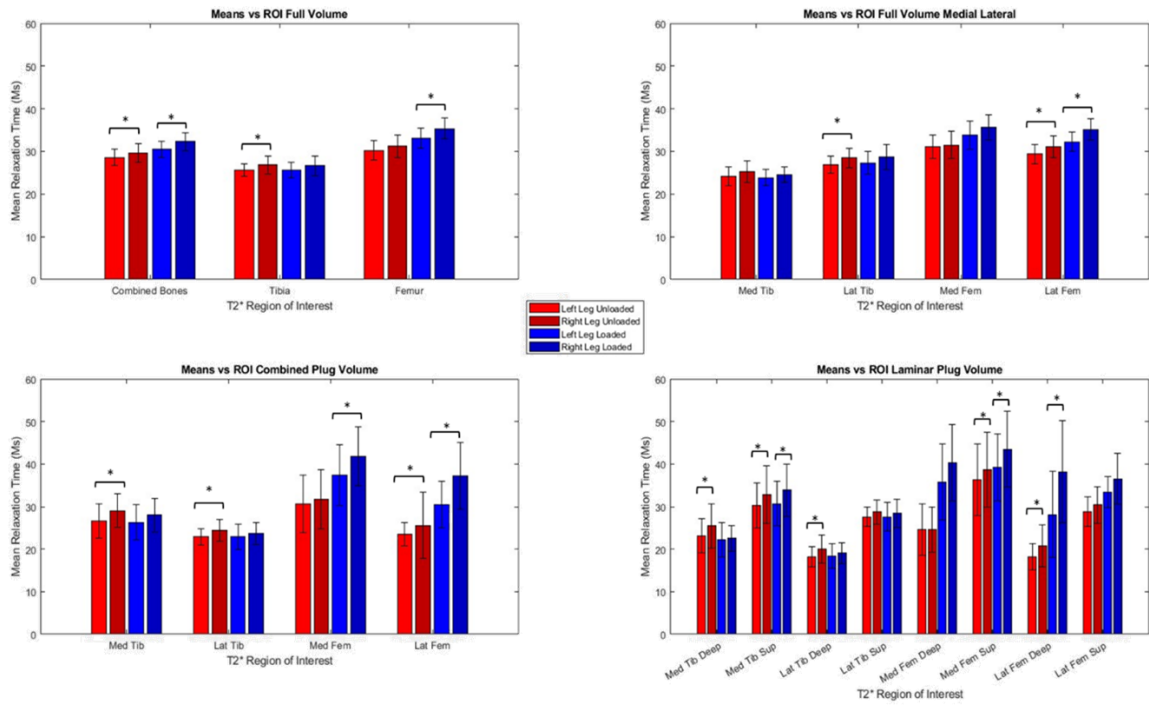


**Figure 19: T2\* relaxation in each ROI for both the left (light) and right (dark) legs in the unloaded (red) and loaded (blue) conditions. Significant differences are indicated by a \* symbol and 95% confidence intervals are represented by the error bars.**

### 5.3. Results

There were significant differences found between left and right limbs in all levels of ROIs for both T1 $\rho$  and T2\*. The full volume (every segmented cartilage pixel) for loaded and unloaded ROIs for both T1 $\rho$  (mean differences were 1.5 ms [loaded] and 2.2 ms[unloaded]) and T2\* (mean differences were 1.5 ms [loaded] and 1.1 ms [unloaded]) were significantly different between sides. For T1 $\rho$ , the maximum margin of error from level one to level five ROIs was 4.5, 3.6, 1.7, 1.5, and 0.7 ms (**Figure 18**). For T2\*, the maximum margin of error from level one to level five ROIs was 7.0, 4.2, 1.4, 1.0, and 0.7 ms (**Figure 19**).

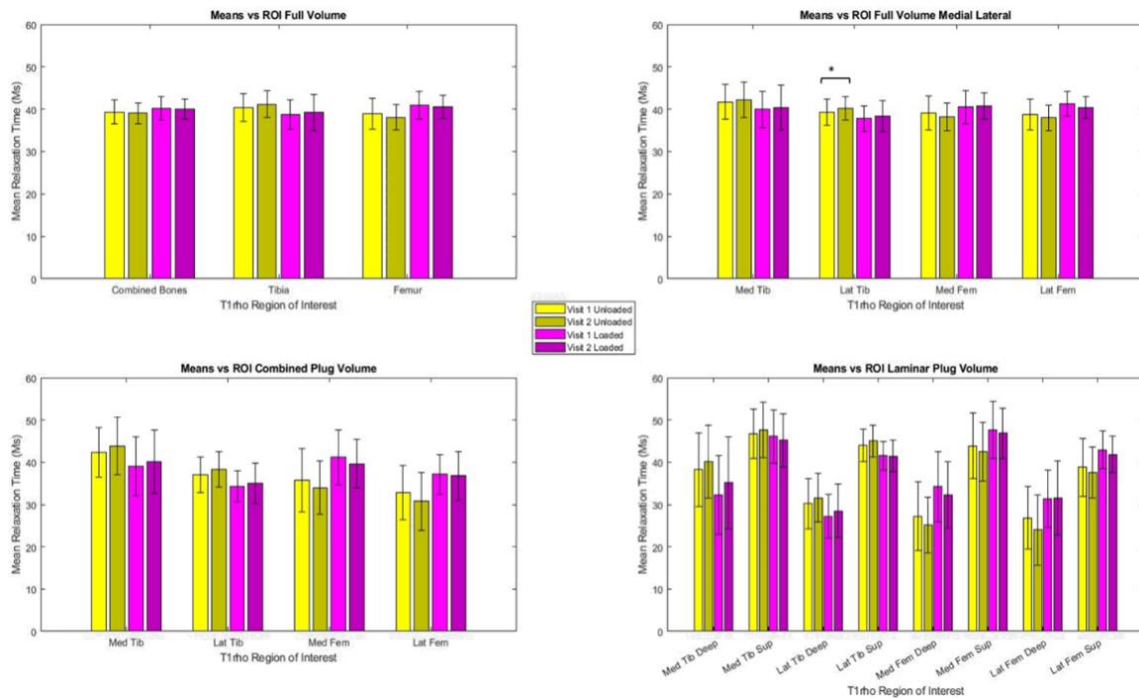


**Figure 20: T1rho relaxation in each ROI for both Visit 1 (light) and Visit 2 (dark) in the unloaded (yellow) and loaded (pink) conditions. Significant differences are indicated by a \* symbol and 95% confidence intervals are represented by error bars.**

There was only one of 38 ROIs with significant differences found between visit 1 and visit 2 for T1 $\rho$  and T2\*. For T1 $\rho$ , there was a significant difference in the full volume by compartment lateral tibia unloaded ROI (mean difference: 0.92 ms,  $p = 0.02$ ) and for the T2\* there was a significant difference for the combined layers plug medial tibia unloaded ROI (mean difference: -1.2 ms,  $p = 0.02$ ). For T1 $\rho$ , the maximum margin of error from level one to level five ROIs was 5.1, 3.8, 1.8, 1.5, and 0.9 ms (**Figure 20**). For T2\*, the maximum margin of error from level one to level five ROIs was 5.3, 3.3, 1.6, 1.2, and 0.8 ms (**Figure 21**).

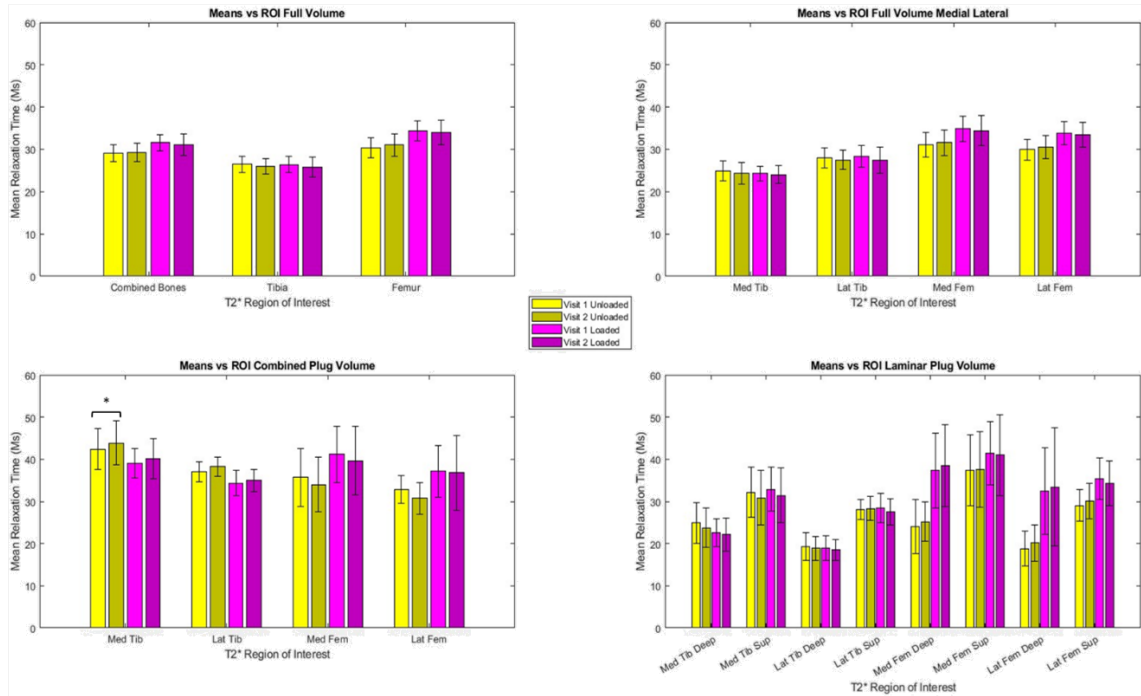


**Figure 21: T2\* relaxation in each ROI for both Visit 1 (light) and Visit 2 (dark) in the unloaded (yellow) and loaded (pink) conditions. Significant differences are indicated by a \* symbol and 95% confidence intervals are represented by the error bars.**

#### 5.4. Discussion

Significant differences between left and right limbs in both T1rho and T2\* qMRI measurements was found in more than half of the 38 ROIs. The results also showed that the full combined ROIs were significantly different between left to right knees in both qMRI metrics. Further analysis shows that right limbs had consistently longer relaxation times than the left limbs. Therefore, the results from this study suggest that there is a systematic bias between left and right limbs. One potential source of the left to right bias may be the difference in off-weighting time. In other words, the participants spent a longer time (close to an extra hour) off-weighted on there right limb because the left limb was

always scanned first. Yet, the bias seemed consistent with the knee in unloaded and loaded conditions. Therefore, it is unlikely that off-weighting would be the primary cause of this bias. Other potential sources of this bias could be magnetic field inhomogeneity or temperature changes as discussed in Chapter 3.4. Further experiments such as measuring field inhomogeneity or measuring temperature changes during scanning may be necessary to determine if these mechanisms are driving the left to right bias.

We also found that there is little to no difference in qMRI measurements between two visits one week apart as there was only 1 of 38 ROIs that was found to be significantly different between visits. There is a clear increase in the 95% confidence limits as the ROIs become smaller. This makes sense as averages are less sensitive to local variability in the larger ROIs. The results also suggest that qMRI measurements with the knee in loaded conditions are just as repeatable as measurements acquired with the knee unloaded.

In conclusion, qMRI measurements T1 $\rho$  and T2\* in the present study presented a systematic left-to-right bias and were repeatable between two visits separated one week apart. As expected, the variation in the measurements grew as the ROIs size got smaller. Future studies should assess the source of the bias and account for the bias when analyzing injured and diseased populations. Ultimately, the results will aid in the analysis and interpretation of data in future studies involving orthopaedic patient populations.

**CHAPTER 6: CHANGES IN QMRI AND ARTHROKINEMATIC  
MEASUREMENTS ACQUIRED SHORTLY AFTER ACL AND MENISCUS  
SURGERY.**

**6.1. Introduction**

The prevalence of OA in those who suffer sports-related knee injuries such as anterior cruciate ligament (ACL) disruption is high [102–105] and even higher in those who suffer ACL disruption with concomitant meniscal lesions [4,106]. Surgical interventions, namely ligament reconstruction and meniscal repair or resection (ACLR+M), are performed to restore stability to the joint and permit return to sport but fail to slow the progression of OA following surgery. In an attempt to understand the mechanisms driving OA disease progression following sports-related injuries, investigators have attempted to link mechanical outcomes in the gait lab to cartilage degeneration. Most research has been limited to studying long term changes because to measure small changes that may be occurring to the mechanics or cartilage shortly after surgery requires highly accurate and technically rigorous approaches.

Much attention is being given to the use of model-based tracking (MBT) with high-speed dual fluoroscopic imaging to capture biomechanical outcomes. For MBT, the combination of highly accurate tracking (bias and precision of less than 1 degree and 1 mm) and the utilization of subject-specific tissue models, permits the measurement of cartilage contact mechanics, which are vastly improved compared to traditional kinematic and kinetic analysis using optical marker tracking. Additionally, quantitative magnetic

resonance imaging (qMRI) has drawn much attention for the assessment of early OA disease progression. Of particular interest are the qMRI parameters  $T1\rho$  and  $T2^*$  that are associated with the matrix composition of articular cartilage. The advantage of a qMRI approach is that changes to the composition of the cartilage must happen prior to morphological changes which have been traditionally used to measure changes associated with PTOA. Both qMRI and MBT require significant personnel, time, technical expertise, and financial resources. Thus, there is limited understanding of how arthrokinematic outcome metrics from MBT are related to compositional metrics from qMRI measurements.

Therefore, the primary purpose of this study was to quantify the effects of ACLR+M on the arthrokinematic (aim 1) and qMRI measurements (aim 2) 1-2 years post-surgery. The secondary purpose of this study was to assess if larger side-to-side differences in arthrokinematic measurements are correlated with larger differences in qMRI measurements (aim 3). Quantifying both alterations to the cartilage loading patterns and how the composition of the cartilage responds to load shortly after surgery in a high-risk population such as ACLR+M will help us better understand the disease progression and ultimately develop therapeutic interventions.

## **6.2. Methods**

### **6.2.1. Participants**

A total of 7 participants – sex: 4 male and 3 female; age:  $26 \pm 5$  (18 - 35) years old [average  $\pm$  standard deviation (range)]; BMI:  $24.5 \pm 3.6$  (18.6 – 29.5); time since surgery:  $1.4 \pm 0.3$  years (1.0 – 1.96), were studied following written and informed consent. All participants

underwent ACLR using an ipsilateral bone-patella tendon-bone autograft along with either the repair or resection of a meniscus injury (Error! Not a valid bookmark self-reference.) and reported an uninjured contralateral limb (confirmed following MR scanning and by a board-certified musculoskeletal fellowship trained radiologist). Two additional participants were withdrawn due to either a scheduling conflict or incidental MR findings (Error! Not a valid bookmark self-reference.).

**Table 5: Participant and meniscal injury (treatment) characteristics**

<i>Subject</i>	<i>Sex</i>	<i>Injured Knee</i>	<i>Meniscus injury Compartment</i>
S01	Male	Left	Medial complex tear (repaired)
S02	Male	Right	Medial longitudinal tear (repaired)
S03	Female	Left	Medial longitudinal tear (repaired); Lateral complex tear (repaired)
S04	Male	Left	Medial complex tear (repaired + resected)
S05*	Female	Left	Medial complex tear (repaired); Lateral complex tear (repaired)
S07	Male	Right	Medial RAMP lesion; Lateral root tear (resected); Lateral complex tear (repaired)
S08**	Female	Right	Medial tear (resected)
S09	Female	Right	Medial longitudinal tear (repaired + resected); Medial ramp lesion (repaired); Lateral complex tear (repaired + resection)
S10***	Female	Right	Lateral complex tear (repaired + resected)
S11	Female	Left	Medial oblique undersurface tear (repaired)

\* Subject withdrawn due to scheduling conflicts

\*\*Subject withdrawn due to Incidental MR findings

\*\*\* Subject withdrawn due to motion during MR acquisition

### 6.2.2. Computed Tomography (CT) and Magnetic Resonance (MR) Imaging

Bilateral computed tomography (CT) images were collected using an iCT SP imaging system (Philips, Eindhoven, Netherlands). The CT acquisition settings were set to 0.67 mm

slice thickness, 120 KVp, and an in-plane resolution of 0.195 mm/pixel with a 300 mm FOV.

An MR scanning session included off-weighting the subject's left knee 15 minutes prior to any acquisitions. Bilateral scans were acquired on all participants. Subsequently, T1 $\rho$  images of the left knee were acquired with the subject supine in a traditional unloaded condition, followed by acquiring T1 $\rho$  and T2\* images of the left knee while a compressive load of 50% bodyweight (BW) was applied by the MRI loading device (**Figure 13**). This process was repeated for the right knee apart from the off-weighting, as the participants' right knee was maintained non-weightbearing while scanning the left knee. T1 $\rho$  was measured using a three-dimensional (3D) magnetization prepared angle modulated partitioned k-space spoiled gradient echo snapshots (3D MAPSS) sequence (see **MR Imaging 4.2.2** or **Table 8a** in the appendix for details on T1 $\rho$  parameters). T2\* was measured using a 3D gradient echo sequence with spiral-out k-space and stack of spirals trajectory sampling strategies (see **MR Imaging 4.2.2** or **Table 9a** in the appendix for details on T2\* parameters).

### **6.2.3. Human Motion Data Collection**

Each participant performed three activities: standing, walking, and jogging. Full-body marker locations, high-speed dual fluoroscopic images, and ground reaction forces (GRFs) were recorded simultaneously for each activity. Full-body marker locations were recorded using a ten-camera motion capture system (VICON) operating at 125 Hz. Dual fluoroscopic images (1024  $\times$  1024 pixels, 250 frames/s, 125 kV, 5 mA) were captured using a previously described system (see **Chapter 2.2.3**). GRFs were measured using a

force plate (AMTI) embedded under the field of view (FOV) of the DFIS sampling at 1000 Hz. Because the FOV of the DFIS is limited and not easily moved, each dynamic activity was performed in both directions along the walkway of the lab to collect images of each knee centered in the FOV (left knee followed by right knee). The dynamic activities (all but the standing) were performed 3 times starting with the left side first to ensure the capture of at least one good trial. A good trial was defined by the ability to visualize the knee in the FOV of the DFIS at the time of heel strike. For each activity and each limb, the trial imaged the largest percent of gait cycle with the DFIS was used for post-processing.

#### **6.2.4. Arthrokinematic Analysis**

Anatomical coordinate systems, bone poses (position and orientation of the bones during an activity), and knee joint 6DOF kinematics were computed using a previously validated MBT system (see **Chapter 2.2.4**). Force plate data was used to define when initial contact and maximal loading (for the walk this was the peak load during the loading phase of gait) occurred in each trial. The bone poses were then resampled using linear interpolation to include 100 poses between heel strike and maximum loading (loading interval).

Bone models were manually segmented (Seg3D v2.4.4, University of Utah) from the CT images. Bone and cartilage models were segmented from T1 $\rho$  MR images. Surface models of bone were imported into MeshLab (v2012.12, Visual Computing Lab), smoothed, and re-meshed to have .75 mm edge lengths. Additionally, each MR bone model was rigidly registered to its corresponding CT bone model as to estimate the pose of the cartilage models during each activity in reference to the tracked CT models used during MBT.

The center of contact in each compartment between the tibia and femur was estimated using custom MATLAB (The MathWorks Inc., Natick, MA) software. Firstly, cartilage models were represented as point clouds by representing each segmented cartilage pixel from each bone as a point. Secondly, at each instance during an activity the tibial cartilage models were transformed into the femoral cartilage reference frame. Third, a weighted centroid algorithm estimated the center of contact in each compartment. All points within a 3mm threshold of the other cartilage model were sampled and given weights. All points that were overlapping were given a weight of 27 (the equivalent of 3mm cubed) and a point that was not, was given a weight corresponding to its distance as:

$$Wiegth(n) = [dist(n) - 3]^2$$

Where  $n$  represents a specific pixel,  $dist(n)$  represents the distance in the sagittal plane from the  $n^{th}$  point from one cartilage model to the closest point on the other.

The location of the center of contact and the overlap volume (points of the tibial cartilage that are either in contact or overlapping with the femoral points at a given instance) in each compartment were quantified at 50 and 20 percent of the loading interval for the walk and jog activities, respectively. The contact locations and contact area of the injured limb were compared to the uninjured limb. To compare contact locations between limbs, the contact locations of the left limb were transformed to the right limb. The transformation was computed by reflecting the left tibia and registering it to the right tibia to compute a left-to-right transformation for each subject. Once transformed, the medial-lateral (ML) and anterior-posterior (AP) position of the contact points in the tibia's anatomical coordinate system were compared between the uninjured and injured limb.

Finally, the ML and AP contact location differences (Injured – uninjured) were normalized by the ML width and AP length of the tibia plateau, respectively. Overlap volume differences were solved by comparing the overlap of injured limbs to that of the uninjured limbs (injured – uninjured).

#### **6.2.5. QMRI Analysis**

Three sagittal slices of the femoral and tibial cartilage from each compartment were segmented from the unloaded T1 $\rho$ , loaded T1 $\rho$ , and the loaded T2\* images. The three slices were selected and segmented by the same individual similarly to previously described methods [78]. The three slices represented the weightbearing regions of each compartment and were chosen by estimating the center of the three slices that were located at 20% and 80% of the width of the tibia plateau. The cartilage-on-cartilage contact regions of both the tibial and femoral cartilage segmentations in each of the three slices within a compartment defined the final region of interests (ROIs). All spin lock/echo time image volumes were registered to the spin lock/echo time image volume that the tissues were segmented on (see **Chapter 4.2.3**). The spin lock/echo time signals for each pixel within a ROI were fit with a mono-exponential function to generate relaxation times. The average of the relaxation times based on all the pixels within an ROI was calculated and used to represent the T1 $\rho$  or T2\* relaxation time for that ROI. Given the results from our prior repeatability analysis in healthy knees, we added a systematic bias to the left ROIs of 3.4 ms and 2.5 ms for the T1 $\rho$  and T2\* measurements, respectively.

**Table 6: Arthrokinematic Outcome metric differences for each subject in each compartment for the walk at 50% heel-strike to max-loading (HS-ML) and for the jog activity at 20% HS-ML. Metrics are expressed as differences between the injured and uninjured limbs (injured minus uninjured). The Anterior-Posterior (AP) and Medial-Lateral (ML) position (Pos) are the contact points in the tibial coordinate system expressed in percent of Tibial Plateau AP or ML width. A negative AP represents a posterior direction, and a negative ML represents a medial direction. Overlap metric represents the difference in number of cartilage pixels in overlap at that specific timepoint.**

		<i>Medial</i>			<i>Lateral</i>		
	Subject	Pos ML	Pos AP	Overlap	Pos ML	Pos AP	Overlap
<i>Walk at 50% HS-ML</i>	01	-7%	-14%	1323	-4%	-4%	-1158
	02	1%	-4%	2684	-7%	-9%	887
	03	0%	0%	-158	1%	-2%	-130
	04	-1%	-7%	2751	-1%	-2%	1061
	07	3%	-6%	535	2%	2%	639
	09	-3%	-10%	352	-5%	-6%	197
	11	0%	-19%	-305	-3%	-12%	-661
<i>Jog at 20% HS-ML</i>	01	-2%	0%	401	6%	-1%	-779
	02	1%	-3%	2256	-7%	11%	4539
	03	2%	1%	447	3%	-3%	919
	04	8%	4%	2668	3%	-4%	-2340
	07	7%	0%	-110	11%	-8%	795
	09	-3%	-5%	1146	-5%	2%	605
	11	1%	-6%	1509	0%	-4%	567

### 6.2.6. Statistical Methods

To quantify the effects of ACLR+M on the arthrokinematics (aim 1) and qMRI measurements (aim 2), descriptive analyses were done to look at the average difference between injured and uninjured limbs. To assess if larger side-to-side differences in arthrokinematic measurements are correlated with larger differences in qMRI measurements (aim 3), pairwise linear correlation coefficients (corr) were quantified between the absolute value of each of the arthrokinematic outcome metric differences and

each of the qMRI outcome metric differences of the same compartment. For example, the T2\* loaded (T2\*LD) relaxation time differences of the lateral tibia were tested against the absolute value of the AP lateral contact point differences. The arthrokinematic and qMRI metrics were deemed correlated if the p-value was less than 0.05.

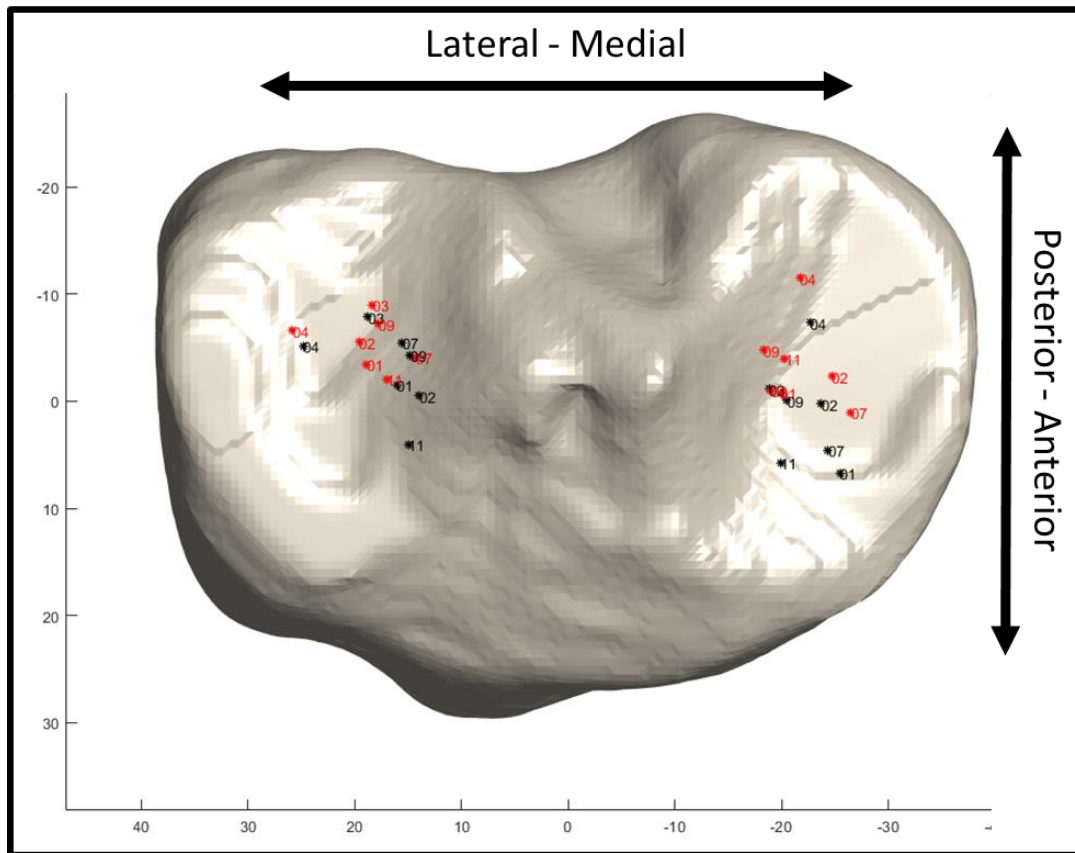


**Figure 22: Contact points at 50% HS-ML for the walk activities. The uninjured (black) and injured (red) contact locations are shown in each compartment.**

### 6.3. Results

The arthrokinematic outcome metric differences are shown in **Table 6**. The AP contact point difference for the walk at 50% HS-ML ranged from 0% to -19% and 2% to -12% for

the medial and lateral compartments, respectively. The AP differences were larger in the medial compartment in 5 of the 7 subjects (**Figure 22**). Injured limbs generally had larger overlaps during the jog at 20% HS-ML as 6 of the 7 for the medial compartment and 5 of the 7 for the lateral compartment had larger overlaps.

**Table 7: qMRI outcomes for the T1 $\rho$  loaded (T1 $\rho$ LD), T1 $\rho$  unloaded (T1 $\rho$ UL), and T2\* Loaded (T2\*LD). qMRI outcomes for each subject were measured as injured minus uninjured relaxation times (ms) for the medial (Med) and lateral (Lat) compartments of both the tibia (Tib) and femur (Fem).**

	<i>Subject</i>	<i>Med-Tib</i>	<i>Lat-Tib</i>	<i>Med-Fem</i>	<i>Lat-Fem</i>
<i>T1<math>\rho</math>LD</i>	01	7.34	4.11	5.09	3.75
	02	-9.57	-2.05	4.04	8.45
	03	-13.27	-7.75	16.34	21.24
	04	5.18	-4.25	14.37	9.10
	07	-1.95	-0.51	4.28	-0.20
	09	-11.86	-4.33	0.38	1.70
	11	9.60	7.02	-4.08	-2.09
<i>T1<math>\rho</math>UL</i>	01	7.11	1.69	-3.22	0.73
	02	-0.85	-3.75	-0.62	5.88
	03	1.60	4.88	10.53	8.13
	04	17.79	3.48	-3.53	-6.82
	07	-5.07	-1.25	3.77	3.31
	09	-7.28	-6.58	13.45	6.66
	11	3.77	1.51	7.26	1.80
<i>T2*LD</i>	01	-11.15	-8.30	-18.01	-5.28
	02	-10.38	-5.62	-5.54	-11.84
	03	5.03	5.61	-1.84	7.94
	04	4.47	-5.61	6.61	4.05
	07	-1.20	-2.23	6.07	-0.18
	09	-12.34	-5.49	-14.92	-6.19
	11	1.90	-0.51	-18.14	-14.16

For the qMRI outcome metrics, there was no metric that showed a consistent change between injured and uninjured limbs (**Table 7**). However, there was an average decrease in the T2\* of injured limbs compared to the normal limb when loaded (**Figure**

23). The absolute average effect of load for  $T1\rho$  was larger for the injured limbs in each of the four ROIs (**Figure 24**). The tibial ROIs showed a decrease in effect of load and the femur ROIs showed an increase. The medial ROIs experience a larger response to load than the lateral ROIs.

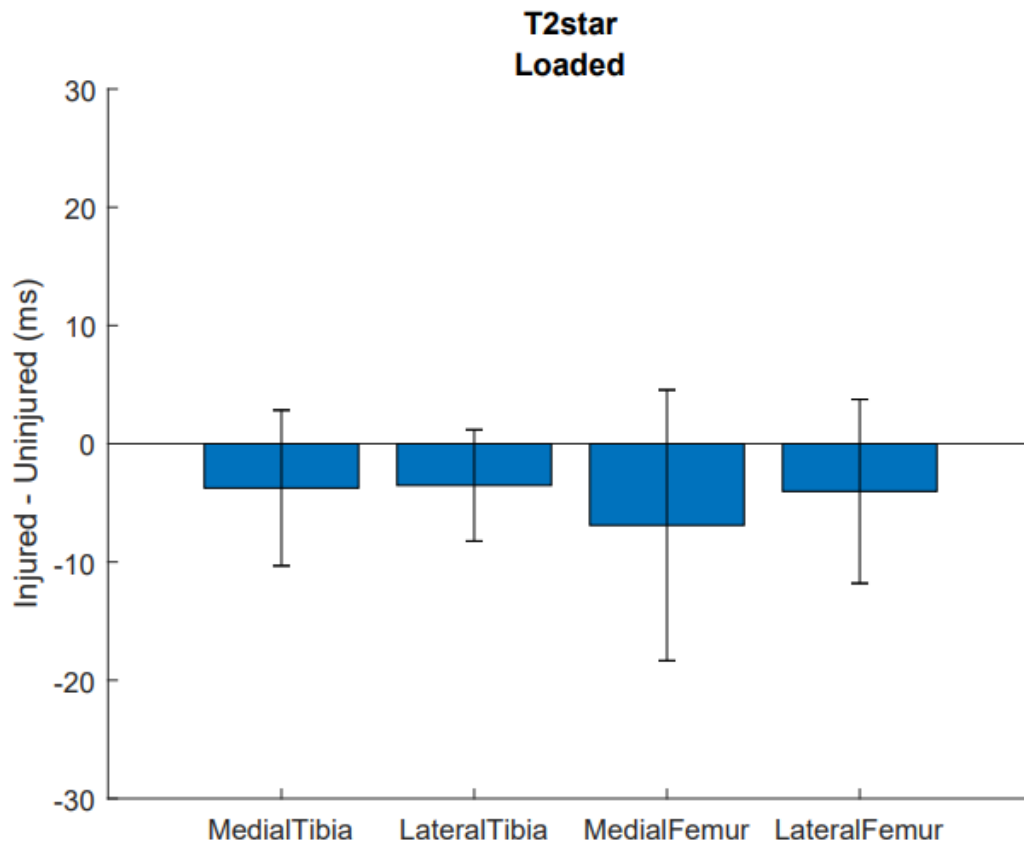


**Figure 23: The average difference and standard deviations in  $T2^*$  relaxation between the injured and uninjured limbs of each ROI.**

The correlation analysis found two of 48 comparisons to be significantly correlated with each other. The most significant finding was that larger AP contact point differences between injured and uninjured limbs were significantly correlated ( $p = 0.01, \text{corr} = -0.89$ ) with a decrease in the loaded T2\* relaxation in the lateral compartment of the femur (**Figure 25**). The second finding was that larger ML contact point differences between injured and uninjured limbs were also significantly correlated ( $p\text{val} = 0.05, \text{corr} = -0.76$ ) with a decrease in the loaded T2\* relaxation in the lateral compartment of the femur.

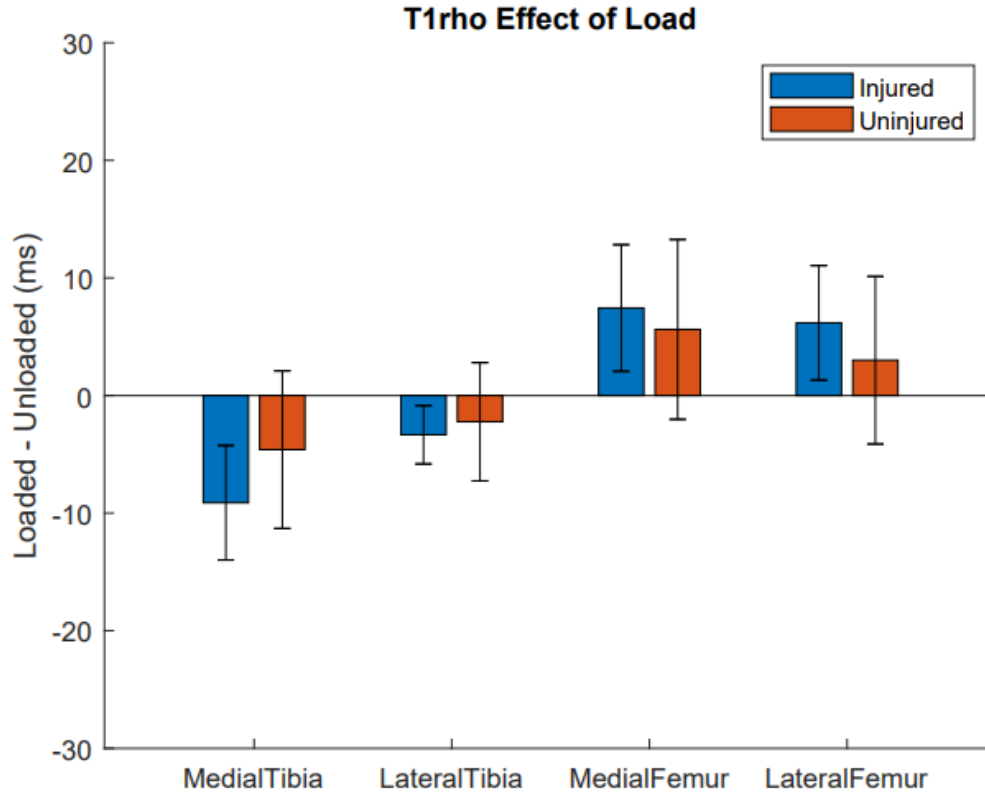


**Figure 24: The average effect of load (loaded T1 $\rho$  - unloaded T1 $\rho$ ) between the injured (blue) and uninjured (red) limbs.**

#### 6.4. Discussion

The present study aimed to quantify arthrokinematics and cartilage composition differences between injured and uninjured limbs one year post ACLR+M. Our results suggest that there was effect of ACLR+M surgery on a subset of the arthrokinematic metrics. During the walk, at 50% of BW-HS there seemed to be a trend towards a more posterior contact location of both compartments in the injured limbs. In other words, the tibia tended to be more anterior shifted in the injured limbs. Amano et al. has shown anterior translation of the tibia in non-weightbearing MR with respect to the femur as early as 1 year post ACLR which is consistent with the findings of a more posterior contact location in the present study [77]. Additionally, Anderst et al. found significantly larger anterior translation of the tibia in ACLR+M at 24 years post-op which is consistent with the present study [107]. Ultimately, the results on the contact points being more posterior from the present study are consistent with prior findings. The present study also found that there was a trend towards an increase in overlap in the ACLR+M knees as compared to the uninjured limbs. A similar study using MBT found similar results that ACLR knees had significantly larger congruency indexes (the amount of contact between cartilage in the joint including meniscus) in the lateral compartment at 24 months following surgery during downhill running [108].

The results also suggest that there was effect of ACLR+M surgery on some of the qMRI metrics that were measured. ACLR+M knees tended toward a shorter loaded T2\* relaxation compared to uninjured limbs. Because T2\* is positively correlated with water content, a shorter T2\* relaxation might suggest a larger decrease in water content in the

injured limbs' cartilage with the addition of a 50% BW compressive load. To the author's knowledge, there has yet to be an investigation studying T2\* in injured knees with the addition of compressive loads. However, there has been a study looking at T2\* in ACLR knees without load and have reported both significant decrease in T2\* in injured limbs [72]. The results from the present study also showed that injured limbs tended to have larger absolute effects of the 50% BW compressive load on T1ρ relaxation. Larger changes in T1ρ suggest larger changes in fluid flow between the femoral and tibial cartilage. There is no study to our knowledge that has examined the effect of load on T1ρ in ACLR+M knees.

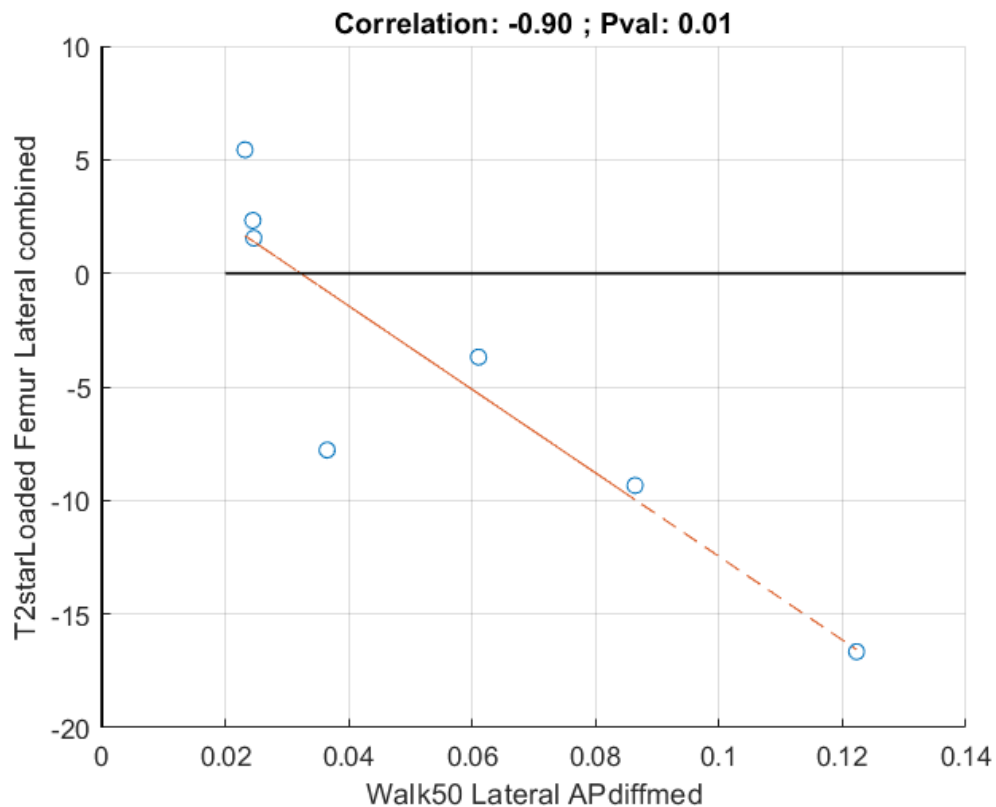


**Figure 25: AP contact point absolute differences between injured and uninjured limbs vs T2\* relaxation differences (injured minus uninjured).**

The present study collected arthrokinematic and cartilage composition measurements at one timepoint. Given these data, to test the hypothesis that changes to the cartilage loading environment following injury is resulting in the degeneration of the articular cartilage, correlations were conducted between the arthrokinematic and cartilage composition measurements to test if patients who had larger changes in arthrokinematics also experienced larger changes in compositional metrics. Of the 48 correlation tests, only two correlations were found to be significant. The significant findings were that larger AP and ML contact point differences between injured and uninjured limbs were significantly correlated with a decrease in the loaded T2\* relaxation in the lateral compartment of the femur. While these correlated results support the hypothesis, the vast majority of uncorrelated results do not.

There are several limitations to the present study. The most apparent is that the number of subjects is small. Additionally, the data for the arthrokinematics was derived from one trial as opposed to multiple trials which increases the likelihood of characterizing an abnormal walking event. The arthrokinematic data were also limited to one timepoint as the FOV for tracking with MBT during non-treadmill gait is limited to the first 10% of the gait cycle. Another potential limitation was that qMRI outcome metrics were limited to 3 slices in each compartment and only analyzed contact regions. This method was chosen because segmenting MRIs of injured limbs is very difficult towards the tibial spines and over the meniscus because of the artifact from screws and anchors used during surgery. Lastly, the qMRI acquisitions acquired a smaller number of echos and spin lock times than

typically acquired to limit the amount of time the participants were in the scanner and under the compressive load, which may have affected the accuracy of our estimation of relaxation constants.

In conclusion, the limited number of subjects in the present study show trends that suggest patients who are 1-2 years post ACLR+M surgery have both arthrokinematic and cartilage compositional side-to-side differences. There is evidence that suggests larger lateral contact location difference are correlated with decreases in the T2\* measurement of the femoral cartilage under load. The combination of data from the present study and future data from that of the same population one year later will ultimately provide us with a better understanding of the disease progression and ultimately help develop therapeutic interventions for individuals who suffer sports-related injuries.

## CHAPTER 7: DISCUSSIONS AND CONCLUSION

The aim of this work was to develop and apply the tools necessary to test the hypothesis that altered arthrokinematics following ACLR+M causes the accelerated progression of OA. Chapter 2 describes the validation of a method for quantifying arthrokinematic measurements via MBT using DFIS. While other investigations have shown that MBT has sub-millimeter and sub-degree accuracy of kinematic measurements, the validation of each system is still very important as there are many steps and variables involved (i.e. cameras, lenses, fluoroscopy units, calibration methods, equipment, segmentations, smoothening, tracking methods, contact algorithms, and many more). Additionally, there is not one gold-standard system in place that is consistent among research groups which further supports the need for individual validation of each system. The major contribution to the literature in this section, is that we quantified how much arthrokinematic measurements changed when the same activity was tracked multiple times. This is important when trying to determine if differences are an effect of surgery or simply an effect of tracker error. This work also showed that tracking errors are larger than errors due to interpolating using the proposed interpolation methods, which supports the use of interpolation in future studies.

Chapter 3 describes the first study to quantify the sources of variability attributed to slice, side (left and right of isocenter), and day for both  $T1\rho$  and  $T2^*$  measurements of small and knee-sized phantoms. The major contribution was that this work showed a position and phantom size dependence on  $T1\rho$  and  $T2^*$  relaxation time values that has not been reported previously. While the  $T1\rho$  and  $T2^*$  relaxation time values from the left scans were significantly different from the right scans, the difference were of very small

magnitudes (less than 1 ms). When studying the knee in humans, the results from this study motivate the use of knee-sized phantoms, especially for T2\* imaging of the knee.

Chapter 4 is the first study that analyzed the effects of acute loading on T1 $\rho$  and T2\* measurements in the human femoral and tibial cartilage separately using an MR compatible loading device. Major contributions from this study involve finding that the effect of acute loading at 40% BW on the qMRI measurements was: 1) opposite in the femoral and tibial cartilage; 2) larger in the cartilage contacting regions than in the non-contacting regions of the femur cartilage; and 3) repeatable between two visits separated by one week. Another major contribution was the introduction of a new hypothesis that the direction of the flux of fluid between the femoral and tibial contacting cartilage may be opposing in response to a 40% BW load.

Chapter 5 was an in depth look at the side-to-side and visit-to-visit repeatability of T1 $\rho$  and T2\* in healthy knees. The major contribution of this work was that it revealed a sidedness bias between left and right scans that has not received attention in the literature. Another contribution to this work was that it showed loaded scans via the MR loading device were just as repeatable as unloaded scans. Lastly, this study was the first to quantify how the repeatability of these measurements change when the ROI size is changed.

Chapter 6 analyzed the arthrokinematic and cartilage compositional outcome metrics in ACLR+M knees 1-2 years post-surgery. The major contribution of this work was the finding that surgery influenced both arthrokinematics (contact locations and overlap during walking) and compositional MR metrics (T2\* with applied load and the effect of load on T1 $\rho$ ). Another contribution was the finding that larger AP differences

in contact locations were correlated with decreases in T2\* loaded measurements which suggest that larger changes in the contact locations of the cartilage is associated with larger changes in cartilage composition.

### **7.1. Implications for Future Research**

A large portion of this work was focused on developing the tools and systems necessary to measure biomechanical outcomes in hopes of better understanding the mechanisms that are driving the accelerated degeneration of the articular cartilage following sports-related injury. Much work can still be done to better understand the capabilities of these tools in detecting abnormalities. As for the arthrokinematic models, further insight into how different filtering techniques, weighted centroid algorithms, and contact velocity estimation approaches affect our measurements will increase the confidence that what we are detecting is truly an effect of injury as opposed to choices in our analysis. As for qMRI, further experimental procedures involving measuring temperature changes or measuring magnetic field inhomogeneity with the addition of our loading device may reveal the cause of our sidedness bias. Additionally, the comparison of results between institutions, such as processing data taken from different research groups using our postprocessing techniques and comparing our answers to that of other institutions, may help understand differences in results and approaches.

Lastly, the combination of data from Chapter 6 (timepoint 1) and future data from that of the same population one year later (timepoint 2) will ultimately provide us with a better understanding of the temporal mechanisms driving the disease progression. To determine if the loading environment is changing and/or if the disease is progressing,

comparisons between 1- and 2-years post-surgery of both the arthrokinematic metrics and cartilage composition measurements should be made. An increase in qMRI metric differences from timepoint 1 to timepoint 2 would suggest the disease is progression and would support the hypothesis that altered loading environments following ACLR+M injury and surgery causes the progression of PTOA. To further support this hypothesis, correlations should be used to test if subjects who had larger arthrokinematic differences at timepoint 1 have larger qMRI metric differences at timepoint 2. If we do not find larger difference in composition between timepoints, it may be the case that the impacts of the abnormal loading quantified at timepoint 1 may occur further out than 2 years post-surgery.

## REFERENCES

- [1] Kaplan, Y., and Witvrouw, E., 2019, “When Is It Safe to Return to Sport After ACL Reconstruction? Reviewing the Criteria,” *Sports Health*, **11**(4), pp. 301–305.
- [2] Brinlee, A. W., Dickenson, S. B., Hunter-Giordano, A., and Snyder-Mackler, L., 2021, “ACL Reconstruction Rehabilitation: Clinical Data, Biologic Healing, and Criterion-Based Milestones to Inform a Return-to-Sport Guideline,” *Sports Health*, **14**(5), pp. 770–779.
- [3] Lohmander, L. S., Östenberg, A., Englund, M., and Roos, H., 2004, “High Prevalence of Knee Osteoarthritis, Pain, and Functional Limitations in Female Soccer Players Twelve Years after Anterior Cruciate Ligament Injury,” *Arthritis & Rheumatism*, **50**(10), pp. 3145–3152.
- [4] Oiestad, B. E., Holm, I., Aune, A. K., Gunderson, R., Myklebust, G., Engebretsen, L., Fosdahl, M. A., and Risberg, M. A., 2010, “Knee Function and Prevalence of Knee Osteoarthritis after Anterior Cruciate Ligament Reconstruction: A Prospective Study with 10 to 15 Years of Follow-Up,” *Am J Sports Med*, **38**(11), pp. 2201–2210.
- [5] Carbone, A., and Rodeo, S., 2017, “Review of Current Understanding of Post-Traumatic Osteoarthritis Resulting from Sports Injuries,” *Journal of Orthopaedic Research*, **35**(3), pp. 397–405.
- [6] Thomas, A. C., Hubbard-Turner, T., Wikstrom, E. A., and Palmieri-Smith, R. M., 2017, “Epidemiology of Posttraumatic Osteoarthritis,” *J Athl Train*, **52**(6), pp. 491–496.
- [7] Brown, T. D., Johnston, R. C., Saltzman, C. L., Marsh, J. L., and Buckwalter, J. A., 2006, “Posttraumatic Osteoarthritis: A First Estimate of Incidence, Prevalence, and Burden of Disease,” *J Orthop Trauma*, **20**(10), pp. 739–744.
- [8] Bodkin, S. G., Werner, B. C., Slater, L. V., and Hart, J. M., 2019, “Post-Traumatic Osteoarthritis Diagnosed within 5 Years Following ACL Reconstruction,” *Knee Surg Sports Traumatol Arthrosc*.
- [9] Wang, L.-J., Zeng, N., Yan, Z.-P., Li, J.-T., and Ni, G.-X., 2020, “Post-Traumatic Osteoarthritis Following ACL Injury,” *Arthritis Res Ther*, **22**(1), p. 57.
- [10] Khella, C. M., Asgarian, R., Horvath, J. M., Rolauffs, B., and Hart, M. L., 2021, “An Evidence-Based Systematic Review of Human Knee Post-Traumatic Osteoarthritis (PTOA): Timeline of Clinical Presentation and Disease Markers, Comparison of Knee Joint PTOA Models and Early Disease Implications,” *Int J Mol Sci*, **22**(4), p. 1996.
- [11] Whittaker, J. L., Truong, L. K., Dhiman, K., and Beck, C., 2021, “Osteoarthritis Year in Review 2020: Rehabilitation and Outcomes,” *Osteoarthritis and Cartilage*, **29**(2), pp. 190–207.
- [12] Hunter, D. J., Schofield, D., and Callander, E., 2014, “The Individual and Socioeconomic Impact of Osteoarthritis,” *Nat Rev Rheumatol*, **10**(7), pp. 437–441.
- [13] Saleh, H., Yu, S., Vigdorichik, J., and Schwarzkopf, R., 2016, “Total Knee Arthroplasty for Treatment of Post-Traumatic Arthritis: Systematic Review,” *World J Orthop*, **7**(9), pp. 584–591.

- [14] Canovas, F., and Dagneaux, L., 2018, “Quality of Life after Total Knee Arthroplasty,” *Orthop Traumatol Surg Res*, **104**(1S), pp. S41–S46.
- [15] Farr II, J., Miller, L. E., and Block, J. E., 2013, “Quality of Life in Patients with Knee Osteoarthritis: A Commentary on Nonsurgical and Surgical Treatments,” *Open Orthop J*, **7**, pp. 619–623.
- [16] Neogi, T., 2013, “The Epidemiology and Impact of Pain in Osteoarthritis,” *Osteoarthritis Cartilage*, **21**(9), pp. 1145–1153.
- [17] Bitton, R., 2009, “The Economic Burden of Osteoarthritis,” *Am J Manag Care*, **15**(8 Suppl), pp. S230–235.
- [18] Kramer, W. C., Hendricks, K. J., and Wang, J., 2011, “Pathogenetic Mechanisms of Posttraumatic Osteoarthritis: Opportunities for Early Intervention,” *Int J Clin Exp Med*, **4**(4), pp. 285–298.
- [19] Anderson, D. D., Chubinskaya, S., Guilak, F., Martin, J. A., Oegema, T. R., Olson, S. A., and Buckwalter, J. A., 2011, “POST-TRAUMATIC OSTEOARTHRITIS: IMPROVED UNDERSTANDING AND OPPORTUNITIES FOR EARLY INTERVENTION,” *J Orthop Res*, **29**(6), pp. 802–809.
- [20] Mall, N. A., Chalmers, P. N., Moric, M., Tanaka, M. J., Cole, B. J., Bach, B. R., and Paletta, G. A., 2014, “Incidence and Trends of Anterior Cruciate Ligament Reconstruction in the United States,” *Am J Sports Med*, **42**(10), pp. 2363–2370.
- [21] Claes, S., Hermie, L., Verdonk, R., Bellemans, J., and Verdonk, P., 2013, “Is Osteoarthritis an Inevitable Consequence of Anterior Cruciate Ligament Reconstruction? A Meta-Analysis,” *Knee Surg Sports Traumatol Arthrosc*, **21**(9), pp. 1967–1976.
- [22] Slater, L. V., Hart, J. M., Kelly, A. R., and Kuenze, C. M., 2017, “Progressive Changes in Walking Kinematics and Kinetics After Anterior Cruciate Ligament Injury and Reconstruction: A Review and Meta-Analysis,” *J Athl Train*, **52**(9), pp. 847–860.
- [23] Cereatti, A., Bonci, T., Akbarshahi, M., Aminian, K., Barré, A., Begon, M., Benoit, D. L., Charbonnier, C., Dal Maso, F., Fantozzi, S., Lin, C.-C., Lu, T.-W., Pandy, M. G., Stagni, R., van den Bogert, A. J., and Camomilla, V., 2017, “Standardization Proposal of Soft Tissue Artefact Description for Data Sharing in Human Motion Measurements,” *Journal of Biomechanics*, **62**, pp. 5–13.
- [24] Fiorentino, N. M., Atkins, P. R., Kutschke, M. J., Goebel, J. M., Foreman, K. B., and Anderson, A. E., 2017, “Soft Tissue Artifact Causes Significant Errors in the Calculation of Joint Angles and Range of Motion at the Hip,” *Gait Posture*, **55**, pp. 184–190.
- [25] Potvin, B., Shourijeh, M., Smale, K., and Benoit, D., 2017, “A Practical Solution to Reduce Soft Tissue Artifact Error at the Knee Using Adaptive Kinematic Constraints,” *Journal of Biomechanics*, **62**, pp. 124–131.
- [26] Benoit, D. L., Ramsey, D. K., Lamontagne, M., Xu, L., Wretenberg, P., and Renström, P., 2006, “Effect of Skin Movement Artifact on Knee Kinematics during Gait and Cutting Motions Measured in Vivo,” *Gait & Posture*, **24**(2), pp. 152–164.
- [27] Sekiya, I., Kohno, Y., Hyodo, A., Katano, H., Komori, K., Koga, H., Tomita, M., Suzuki, K., Masumoto, J., and Ozeki, N., 2021, “Interscan Measurement Error of

- Knee Cartilage Thickness and Projected Cartilage Area Ratio at 9 Regions and 45 Subregions by Fully Automatic Three-Dimensional MRI Analysis,” *Eur J Radiol*, **139**, p. 109700.
- [28] Gurchiek, R. D., Cheney, N., and McGinnis, R. S., 2019, “Estimating Biomechanical Time-Series with Wearable Sensors: A Systematic Review of Machine Learning Techniques,” *Sensors (Basel)*, **19**(23), p. 5227.
- [29] Gurchiek, R. D., Donahue, N., Fiorentino, N. M., and McGinnis, R. S., 2022, “Wearables-Only Analysis of Muscle and Joint Mechanics: An EMG-Driven Approach,” *IEEE Trans Biomed Eng*, **69**(2), pp. 580–589.
- [30] Wade, L., Needham, L., McGuigan, P., and Bilzon, J., 2022, “Applications and Limitations of Current Markerless Motion Capture Methods for Clinical Gait Biomechanics,” *PeerJ*, **10**, p. e12995.
- [31] Kanko, R. M., Laende, E. K., Davis, E. M., Selbie, W. S., and Deluzio, K. J., 2021, “Concurrent Assessment of Gait Kinematics Using Marker-Based and Markerless Motion Capture,” *J Biomech*, **127**, p. 110665.
- [32] Gray, H. A., Guan, S., and Pandy, M. G., 2017, “Accuracy of Mobile Biplane X-Ray Imaging in Measuring 6-Degree-of-Freedom Patellofemoral Kinematics during Overground Gait,” *Journal of Biomechanics*, **57**, pp. 152–156.
- [33] Thorhauer, E., and Tashman, S., 2015, “Validation of a Method for Combining Biplanar Radiography and Magnetic Resonance Imaging to Estimate Knee Cartilage Contact,” *Med Eng Phys*, **37**(10), pp. 937–947.
- [34] Anderst, W., Zael, R., Bishop, J., Demps, E., and Tashman, S., 2009, “Validation of Three-Dimensional Model-Based Tibio-Femoral Tracking during Running,” *Medical Engineering & Physics*, **31**(1), pp. 10–16.
- [35] Li, G., Van de Velde, S. K., and Bingham, J. T., 2008, “Validation of a Non-Invasive Fluoroscopic Imaging Technique for the Measurement of Dynamic Knee Joint Motion,” *Journal of Biomechanics*, **41**(7), pp. 1616–1622.
- [36] Bey, M. J., Zael, R., Brock, S. K., and Tashman, S., 2006, “Validation of a New Model-Based Tracking Technique for Measuring Three-Dimensional, In Vivo Glenohumeral Joint Kinematics,” *J Biomech Eng*, **128**(4), pp. 604–609.
- [37] Pius, A. K., Beynnon, B. D., Fiorentino, N., Gardner-Morse, M., Vacek, P. M., DeSarno, M., Failla, M., Slauterbeck, J. R., Sturnick, D. R., Argentieri, E. C., and Tourville, T. W., 2022, “Articular Cartilage Thickness Changes Differ between Males and Females 4 Years Following Anterior Cruciate Ligament Reconstruction,” *Journal of Orthopaedic Research*, **40**(1), pp. 65–73.
- [38] Lonza, G. C., Gardner-Morse, M. G., Vacek, P. M., and Beynnon, B. D., 2019, “Radiographic-Based Measurement of Tibiofemoral Joint Space Width and Magnetic Resonance Imaging Derived Articular Cartilage Thickness Are Not Related in Subjects at Risk for Post Traumatic Arthritis of the Knee,” *J Orthop Res*, **37**(5), pp. 1052–1058.
- [39] Guermazi, A., Alizai, H., Crema, M. D., Trattinig, S., Regatte, R. R., and Roemer, F. W., 2015, “Compositional MRI Techniques for Evaluation of Cartilage Degeneration in Osteoarthritis,” *Osteoarthritis Cartilage*, **23**(10), pp. 1639–1653.

- [40] MacKay, J. W., Low, S. B. L., Smith, T. O., Toms, A. P., McCaskie, A. W., and Gilbert, F. J., 2018, “Systematic Review and Meta-Analysis of the Reliability and Discriminative Validity of Cartilage Compositional MRI in Knee Osteoarthritis,” *Osteoarthritis Cartilage*, **26**(9), pp. 1140–1152.
- [41] Andriacchi, T. P., Koo, S., and Scanlan, S. F., 2009, “Gait Mechanics Influence Healthy Cartilage Morphology and Osteoarthritis of the Knee,” *Journal of Bone and Joint Surgery*, **91**(Supplement\_1), pp. 95–101.
- [42] Koo, S., and Andriacchi, T. P., 2007, “A Comparison of the Influence of Global Functional Loads vs. Local Contact Anatomy on Articular Cartilage Thickness at the Knee,” *Journal of Biomechanics*, **40**(13), pp. 2961–2966.
- [43] Chaudhari, A. M. W., Briant, P. L., Beville, S. L., Koo, S., and Andriacchi, T. P., 2008, “Knee Kinematics, Cartilage Morphology, and Osteoarthritis after ACL Injury,” *Medicine & Science in Sports & Exercise*, **40**(2), pp. 215–222.
- [44] Anderst, W., Irrgang, J. J., Fu, F. H., Tashman, S., Karlsson, J., and Musahl, V., 2021, “In Search of a Gold Standard for Objective Clinical Outcome: Using Dynamic Biplane Radiography to Measure Knee Kinematics,” *Knee Surg Sports Traumatol Arthrosc.*
- [45] Miranda, D. L., Schwartz, J. B., Loomis, A. C., Brainerd, E. L., Fleming, B. C., and Crisco, J. J., 2011, “Static and Dynamic Error of a Biplanar Videoradiography System Using Marker-Based and Markerless Tracking Techniques,” *J Biomech Eng*, **133**(12), p. 121002.
- [46] Guan, S., Gray, H. A., Keynejad, F., and Pandy, M. G., 2016, “Mobile Biplane X-Ray Imaging System for Measuring 3D Dynamic Joint Motion During Overground Gait,” *IEEE Transactions on Medical Imaging*, **35**(1), pp. 326–336.
- [47] Söderkvist, I., and Wedin, P.-Å., 1993, “Determining the Movements of the Skeleton Using Well-Configured Markers,” *Journal of Biomechanics*, **26**(12), pp. 1473–1477.
- [48] Gray, H. A., Guan, S., and Pandy, M. G., 2017, “Accuracy of Mobile Biplane X-Ray Imaging in Measuring 6-Degree-of-Freedom Patellofemoral Kinematics during Overground Gait,” *Journal of Biomechanics*, **57**, pp. 152–156.
- [49] Cignoni, P., Callieri, M., Corsini, M., Dellepiane, M., Ganovelli, F., and Ranzuglia, G., “MeshLab: An Open-Source Mesh Processing Tool,” p. 8.
- [50] Miranda, D. L., Rainbow, M. J., Leventhal, E. L., Crisco, J. J., and Fleming, B. C., 2010, “Automatic Determination of Anatomical Coordinate Systems for Three-Dimensional Bone Models of the Isolated Human Knee,” *J Biomech*, **43**(8), pp. 1623–1626.
- [51] Knörlein, B. J., Baier, D. B., Gatesy, S. M., Laurence-Chasen, J. D., and Brainerd, E. L., 2016, “Validation of XMALab Software for Marker-Based XROMM,” *Journal of Experimental Biology*, **219**(23), pp. 3701–3711.
- [52] “DSX Overview - Visual3D Wiki Documentation” [Online]. Available: [https://www.c-motion.com/v3dwiki/index.php?title=DSX\\_Overview](https://www.c-motion.com/v3dwiki/index.php?title=DSX_Overview). [Accessed: 03-Jan-2023].
- [53] Brainerd, E. L., Baier, D. B., Gatesy, S. M., Hedrick, T. L., Metzger, K. A., Gilbert, S. L., and Crisco, J. J., 2010, “X-Ray Reconstruction of Moving Morphology (XROMM): Precision, Accuracy and Applications in Comparative Biomechanics

- Research,” *Journal of Experimental Zoology Part A: Ecological Genetics and Physiology*, **313A**(5), pp. 262–279.
- [54] Woltring, H. J., 1986, “A Fortran Package for Generalized, Cross-Validatory Spline Smoothing and Differentiation,” *Advances in Engineering Software* (1978), **8**(2), pp. 104–113.
- [55] Grood, E. S., and Suntay, W. J., 1983, “A Joint Coordinate System for the Clinical Description of Three-Dimensional Motions: Application to the Knee,” *J Biomech Eng*, **105**(2), pp. 136–144.
- [56] Beveridge, J. E., Shrive, N. G., and Frank, C. B., 2014, “Repeatability and Precision of a Weighted Centroid Method for Estimating Dynamic in Vivo Tibiofemoral Surface Interactions in Sheep,” *Computer Methods in Biomechanics and Biomedical Engineering*, **17**(16), pp. 1853–1863.
- [57] Anderst, W. J., and Tashman, S., 2003, “A Method to Estimate in Vivo Dynamic Articular Surface Interaction,” *Journal of Biomechanics*, **36**(9), pp. 1291–1299.
- [58] Foumani, M., Strackee, S. D., van de Giessen, M., Jonges, R., Blankevoort, L., and Streekstra, G. J., 2013, “In-Vivo Dynamic and Static Three-Dimensional Joint Space Distance Maps for Assessment of Cartilage Thickness in the Radiocarpal Joint,” *Clinical Biomechanics*, **28**(2), pp. 151–156.
- [59] Zheng, L., Carey, R., Thorhauer, E., Tashman, S., Harner, C., and Zhang, X., 2018, “In Vivo Tibiofemoral Skeletal Kinematics and Cartilage Contact Arthrokinematics during Decline Walking after Isolated Meniscectomy,” *Medical Engineering & Physics*, **51**, pp. 41–48.
- [60] Nishida, K., Gale, T., Chiba, D., Suntaxi, F., Lesniak, B., Fu, F., Anderst, W., and Musahl, V., 2021, “The Effect of Lateral Extra-Articular Tenodesis on in Vivo Cartilage Contact in Combined Anterior Cruciate Ligament Reconstruction,” *Knee Surg Sports Traumatol Arthrosc*.
- [61] Akpınar, B., Thorhauer, E., Tashman, S., Irrgang, J. J., Fu, F. H., and Anderst, W. J., 2019, “Tibiofemoral Cartilage Contact Differences Between Level Walking and Downhill Running,” *Orthop J Sports Med*, **7**(4).
- [62] Thomeer, L. T., Guan, S., Gray, H. A., and Pandy, M. G., 2022, “Articular Contact Motion at the Knee during Daily Activities,” *J Orthop Res*, **40**(8), pp. 1756–1769.
- [63] DeFrate, L. E., Sun, H., Gill, T. J., Rubash, H. E., and Li, G., 2004, “In Vivo Tibiofemoral Contact Analysis Using 3D MRI-Based Knee Models,” *Journal of Biomechanics*, **37**(10), pp. 1499–1504.
- [64] Kim, J., Mamoto, K., Lartey, R., Xu, K., Nakamura, K., Shin, W., Winalski, C. S., Obuchowski, N., Tanaka, M., Bahroos, E., Link, T. M., Hardy, P. A., Peng, Q., Reddy, R., Bemden, A. B., Liu, K., Peters, R. D., Wu, C., and Li, X., 2020, “Multi-Vendor Multi-Site T1 $\rho$  and T2 Quantification of Knee Cartilage,” *Osteoarthritis and Cartilage*, **28**(12), pp. 1539–1550.
- [65] Wei, Z., Ma, Y.-J., Jang, H., Yang, W., and Du, J., 2020, “To Measure T1 of Short T2 Species Using an Inversion Recovery Prepared Three-Dimensional Ultrashort Echo Time (3D IR-UTE) Method: A Phantom Study,” *J Magn Reson*, **314**, p. 106725.
- [66] Li, X., Han, E. T., Busse, R. F., and Majumdar, S., 2008, “In Vivo T1 $\rho$  Mapping in Cartilage Using 3D Magnetization-Prepared Angle-Modulated Partitioned k-Space

- Spoiled Gradient Echo Snapshots (3D MAPSS),” *Magnetic Resonance in Medicine*, **59**(2), pp. 298–307.
- [67] Otsu, N., 1979, “A Threshold Selection Method from Gray-Level Histograms,” *IEEE Transactions on Systems, Man, and Cybernetics*, **9**(1), pp. 62–66.
- [68] “GitHub - Mggardne/MRI\_Phantom: Matlab Code for Segmenting and Calculating T1rho or T2\* from Philips MRI Images of Phantom” [Online]. Available: [https://github.com/mggardne/MRI\\_Phantom](https://github.com/mggardne/MRI_Phantom). [Accessed: 12-Oct-2022].
- [69] Levenberg, K., 1944, “A Method for the Solution of Certain Non-Linear Problems in Least Squares,” *Quart. Appl. Math.*, **2**(2), pp. 164–168.
- [70] Marquardt, D. W., 1963, “An Algorithm for Least-Squares Estimation of Nonlinear Parameters,” *Journal of the Society for Industrial and Applied Mathematics*, **11**(2), pp. 431–441.
- [71] Wang, L., and Regatte, R. R., 2014, “Quantitative Mapping of Human Cartilage at 3.0T: Parallel Changes in T2, T1ρ, and DGEMRIC,” *Academic Radiology*, **21**(4), pp. 463–471.
- [72] Williams, A. A., Titchenal, M. R., Andriacchi, T. P., and Chu, C. R., 2018, “MRI UTE-T2\* Profile Characteristics Correlate to Walking Mechanics and Patient Reported Outcomes 2 Years after ACL Reconstruction,” *Osteoarthritis and Cartilage*, **26**(4), pp. 569–579.
- [73] Shellock, F. G., Schaefer, D. J., and Crues, J. V., 1989, “Alterations in Body and Skin Temperatures Caused by Magnetic Resonance Imaging: Is the Recommended Exposure for Radiofrequency Radiation Too Conservative?,” *Br J Radiol*, **62**(742), pp. 904–909.
- [74] Rieke, V., and Pauly, K. B., 2008, “MR Thermometry,” *J Magn Reson Imaging*, **27**(2), pp. 376–390.
- [75] Banjar, M., Horiuchi, S., Gedeon, D. N., and Yoshioka, H., 2022, “Review of Quantitative Knee Articular Cartilage MR Imaging,” *Magn Reson Med Sci*, **21**(1), pp. 29–40.
- [76] Obuchowski, N. A., Reeves, A. P., Huang, E. P., Wang, X.-F., Buckler, A. J., Kim, H. J. G., Barnhart, H. X., Jackson, E. F., Giger, M. L., Pennello, G., Toledano, A. Y., Kalpathy-Cramer, J., Apanasovich, T. V., Kinahan, P. E., Myers, K. J., Goldgof, D. B., Barboriak, D. P., Gillies, R. J., Schwartz, L. H., Sullivan, D. C., and Algorithm Comparison Working Group, 2015, “Quantitative Imaging Biomarkers: A Review of Statistical Methods for Computer Algorithm Comparisons,” *Stat Methods Med Res*, **24**(1), pp. 68–106.
- [77] Amano, K., Padoia, V., Su, F., Souza, R. B., Li, X., and Ma, C. B., 2016, “Persistent Biomechanical Alterations After ACL Reconstruction Are Associated With Early Cartilage Matrix Changes Detected by Quantitative MR,” *Orthop J Sports Med*, **4**(4), p. 2325967116644421.
- [78] Williams, A. A., Titchenal, M. R., Do, B. H., Guha, A., and Chu, C. R., 2019, “MRI UTE-T2\* Shows High Incidence of Cartilage Subsurface Matrix Changes 2 Years after ACL Reconstruction,” *J Orthop Res*, **37**(2), pp. 370–377.
- [79] Theologis, A. A., Haughom, B., Liang, F., Zhang, Y., Majumdar, S., Link, T. M., Ma, C. B., and Li, X., 2014, “Comparison of T1rho Relaxation Times between ACL-

- Reconstructed Knees and Contralateral Uninjured Knees,” *Knee Surg Sports Traumatol Arthrosc*, **22**(2), pp. 298–307.
- [80] Padoia, V., Su, F., Amano, K., Li, Q., McCulloch, C. E., Souza, R. B., Link, T. M., Ma, B. C., and Li, X., 2017, “Analysis of the Articular Cartilage T1 $\rho$  and T2 Relaxation Times Changes After ACL Reconstruction in Injured and Contralateral Knees and Relationships With Bone Shape,” *J Orthop Res*, **35**(3), pp. 707–717.
- [81] Wheaton, A. J., Dodge, G. R., Elliott, D. M., Nicoll, S. B., and Reddy, R., 2005, “Quantification of Cartilage Biomechanical and Biochemical Properties via T1 $\rho$  Magnetic Resonance Imaging,” *Magnetic Resonance in Medicine*, **54**(5), pp. 1087–1093.
- [82] Williams, A., Qian, Y., Bear, D., and Chu, C. R., 2010, “Assessing Degeneration of Human Articular Cartilage with Ultra-Short Echo Time (UTE) T2\* Mapping,” *Osteoarthritis Cartilage*, **18**(4), pp. 539–546.
- [83] Matzat, S. J., van Tiel, J., Gold, G. E., and Oei, E. H. G., 2013, “Quantitative MRI Techniques of Cartilage Composition,” *Quant Imaging Med Surg*, **3**(3), pp. 162–174.
- [84] Jerban, S., Chang, E. Y., and Du, J., 2020, “Magnetic Resonance Imaging (MRI) Studies of Knee Joint under Mechanical Loading: Review,” *Magn Reson Imaging*, **65**, pp. 27–36.
- [85] Souza, R. B., Stehling, C., Wyman, B. T., Graverand, M.-P. H. L., Li, X., Link, T. M., and Majumdar, S., 2010, “The Effects of Acute Loading on T1 $\rho$  and T2 Relaxation Times of Tibiofemoral Articular Cartilage,” *Osteoarthritis and Cartilage*, **18**(12), pp. 1557–1563.
- [86] Subburaj, K., Souza, R. B., Stehling, C., Wyman, B. T., Le Graverand-Gastineau, M.-P., Link, T. M., Li, X., and Majumdar, S., 2012, “Association of MR Relaxation and Cartilage Deformation in Knee Osteoarthritis,” *J Orthop Res*, **30**(6), pp. 919–926.
- [87] Rosset, A., Spadola, L., and Ratib, O., 2004, “OsiriX: An Open-Source Software for Navigating in Multidimensional DICOM Images,” *J Digit Imaging*, **17**(3), pp. 205–216.
- [88] “GitHub - Mggardne/MRI\_T1rho\_T2star\_reliability: Matlab Code for Calculating T1 $\rho$  or T2\* from Philips MRI Images of Phantom” [Online]. Available: [https://github.com/mggardne/MRI\\_T1rho\\_T2star\\_reliability](https://github.com/mggardne/MRI_T1rho_T2star_reliability). [Accessed: 12-Dec-2022].
- [89] Klein, S., Staring, M., Murphy, K., Viergever, M. A., and Pluim, J. P. W., 2010, “Elastix: A Toolbox for Intensity-Based Medical Image Registration,” *IEEE Trans Med Imaging*, **29**(1), pp. 196–205.
- [90] Hamada, H., Nishii, T., Tamura, S., Tanaka, H., Wakayama, T., and Sugano, N., 2015, “Comparison of Load Responsiveness of Cartilage T1 $\rho$  and T2 in Porcine Knee Joints: An Experimental Loading MRI Study,” *Osteoarthritis and Cartilage*, **23**(10), pp. 1776–1779.
- [91] McLure, S. W. D., Fisher, J., Conaghan, P. G., and Williams, S., 2012, “Regional Cartilage Properties of Three Quadruped Tibiofemoral Joints Used in Musculoskeletal Research Studies,” *Proc Inst Mech Eng H*, **226**(8), pp. 652–656.
- [92] Van Rossom, S., Smith, C. R., Zevenbergen, L., Thelen, D. G., Vanwanseele, B., Van Assche, D., and Jonkers, I., 2017, “Knee Cartilage Thickness, T1 $\rho$  and T2 Relaxation

- Time Are Related to Articular Cartilage Loading in Healthy Adults,” PLoS One, **12**(1), p. e0170002.
- [93] Heckelman, L. N., Smith, W. A. R., Riofrio, A. D., Vinson, E. N., Collins, A. T., Gwynn, O. R., Utturkar, G. M., Goode, A. P., Spritzer, C. E., and DeFrate, L. E., 2020, “Quantifying the Biochemical State of Knee Cartilage in Response to Running Using T1rho Magnetic Resonance Imaging,” *Sci Rep*, **10**(1), p. 1870.
- [94] Subburaj, K., Kumar, D., Souza, R. B., Alizai, H., Li, X., Link, T. M., and Majumdar, S., 2012, “The Acute Effect of Running on Knee Articular Cartilage and Meniscus Magnetic Resonance Relaxation Times in Young Healthy Adults,” *Am J Sports Med*, **40**(9), pp. 2134–2141.
- [95] Li, H., Li, J., Yu, S., Wu, C., and Zhang, W., 2021, “The Mechanical Properties of Tibiofemoral and Patellofemoral Articular Cartilage in Compression Depend on Anatomical Regions,” *Sci Rep*, **11**(1), p. 6128.
- [96] Patel, R., Eltgroth, M., Souza, R. B., Zhang, C. A., Majumdar, S., Link, T. M., and Motamedi, D., 2016, “Loaded versus Unloaded Magnetic Resonance Imaging (MRI) of the Knee: Effect on Meniscus Extrusion in Healthy Volunteers and Patients with Osteoarthritis,” *Eur J Radiol Open*, **3**, pp. 100–107.
- [97] Shiomi, T., Nishii, T., Tamura, S., Tanaka, H., Murase, K., Yoshikawa, H., and Sugano, N., 2012, “Influence of Medial Meniscectomy on Stress Distribution of the Femoral Cartilage in Porcine Knees: A 3D Reconstructed T2 Mapping Study,” *Osteoarthritis and Cartilage*, **20**(11), pp. 1383–1390.
- [98] Nishii, T., Kuroda, K., Matsuoka, Y., Sahara, T., and Yoshikawa, H., 2008, “Change in Knee Cartilage T2 in Response to Mechanical Loading,” *Journal of Magnetic Resonance Imaging*, **28**(1), pp. 175–180.
- [99] Mow, V. C., and Huijskes, R., 2005, *Basic Orthopaedic Biomechanics & Mechano-Biology*, Lippincott Williams & Wilkins.
- [100] Bingham, J. T., Papannagari, R., Van de Velde, S. K., Gross, C., Gill, T. J., Felson, D. T., Rubash, H. E., and Li, G., 2008, “In Vivo Cartilage Contact Deformation in the Healthy Human Tibiofemoral Joint,” *Rheumatology (Oxford)*, **47**(11), pp. 1622–1627.
- [101] Beynnon, B. D., Fleming, B. C., Labovitch, R., and Parsons, B., 2002, “Chronic Anterior Cruciate Ligament Deficiency Is Associated with Increased Anterior Translation of the Tibia during the Transition from Non-Weightbearing to Weightbearing,” *J Orthop Res*, **20**(2), pp. 332–337.
- [102] Sepúlveda, F., Sánchez, L., Amy, E., and Micheo, W., 2017, “Anterior Cruciate Ligament Injury: Return to Play, Function and Long-Term Considerations,” *Curr Sports Med Rep*, **16**(3), pp. 172–178.
- [103] Webster, K. E., and Hewett, T. E., 2022, “Anterior Cruciate Ligament Injury and Knee Osteoarthritis: An Umbrella Systematic Review and Meta-Analysis,” *Clin J Sport Med*, **32**(2), pp. 145–152.
- [104] Barenus, B., Ponzer, S., Shalabi, A., Bujak, R., Norlén, L., and Eriksson, K., 2014, “Increased Risk of Osteoarthritis after Anterior Cruciate Ligament Reconstruction: A 14-Year Follow-up Study of a Randomized Controlled Trial,” *Am J Sports Med*, **42**(5), pp. 1049–1057.

- [105] Ruano, J. S., Sitler, M. R., and Driban, J. B., 2017, “Prevalence of Radiographic Knee Osteoarthritis After Anterior Cruciate Ligament Reconstruction, With or Without Meniscectomy: An Evidence-Based Practice Article,” *J Athl Train*, **52**(6), pp. 606–609.
- [106] Lohmander, L. S., Englund, P. M., Dahl, L. L., and Roos, E. M., 2007, “The Long-Term Consequence of Anterior Cruciate Ligament and Meniscus Injuries: Osteoarthritis,” *Am J Sports Med*, **35**(10), pp. 1756–1769.
- [107] Akpinar, B., Thorhauer, E., Irrgang, J. J., Tashman, S., Fu, F. H., and Anderst, W. J., 2018, “Alteration of Knee Kinematics After Anatomic Anterior Cruciate Ligament Reconstruction Is Dependent on Associated Meniscal Injury,” *Am J Sports Med*, **46**(5), pp. 1158–1165.
- [108] Nagai, K., Gale, T., Irrgang, J. J., Tashman, S., Fu, F. H., and Anderst, W., 2018, “Anterior Cruciate Ligament Reconstruction Affects Tibiofemoral Joint Congruency During Dynamic Functional Movement,” *Am J Sports Med*, **46**(7), pp. 1566–1574.

## APPENDIX

**Table 8a: MR scanning parameters for the T1 $\rho$  acquisitions in vivo knee scans.**

3D T1 $\rho$ imaging	In vivo study
Field of View (FH x AP x RL mm <sup>3</sup> )	250x140x96
Acquired matrix size	500x280x32
Image orientation	Sagittal
Rec matrix size	512x512x64
Time of recovery (ms)	2150
Spin-lock times (ms)	0,10,40,80
Echo time (ms)	5.1
Repetition time (ms)	10.0
Flip angle (°)	70
Acquisition time	9min 11 sec
Bandwidth per pixel (Hz/pix)	287.4
TFE factor	92
Spin-lock Frequency (Hz)	500
Compress Sensing factor	3.2
TFE profile order	Low-high
TFE turbo direction	radial
Fat suppression	ProSet-1331
B <sub>0</sub> Shimming	PB-volume

**Table 9a: MR scanning parameters for the unloaded and loaded T2\* in vivo knee acquisitions.**

3D T2* imaging	In vivo
Field of View (mm <sup>3</sup> )	140x140x96
Acquired matrix size	232x232x24
Image orientation	Sagittal
Rec matrix size	320x320x48
Number of Echoes	6
Echo times	0.42, 1.0, 5.0, 15.0, 30.0
Repetition time (ms)	50
Flip angle (°)	8
Spiral acquisition window (ms)	2.9
Number of spiral interleaves	126
B <sub>0</sub> Shimming	PB-volume
Fat suppression	SPIR
Acquisition duration	12min and 37.5sec